

Evidence for a \mathbb{Z}_2 Dirac spin liquid in the generalized Shastry-Sutherland model

Atanu Maity,^{1,2} Francesco Ferrari,^{2,3} Jong Yeon Lee,⁴ Janik Potten,¹
Tobias Müller,¹ Ronny Thomale,^{1,2} Rhine Samajdar,^{5,6} and Yasir Iqbal^{2,*}

¹*Institut für Theoretische Physik und Astrophysik and Würzburg-Dresden Cluster of Excellence ct.qmat,
Julius-Maximilians-Universität Würzburg, Am Hubland, Campus Süd, Würzburg 97074, Germany*

²*Department of Physics and Quantum Centre of Excellence for Diamond and Emergent Materials (QuCenDiEM),
Indian Institute of Technology Madras, Chennai 600036, India*

³*Institut für Theoretische Physik, Goethe Universität Frankfurt,
Max-von-Laue-Straße 1, 60438 Frankfurt am Main, Germany*

⁴*Department of Physics and Anthony J. Leggett Institute for Condensed Matter Theory,
University of Illinois at Urbana-Champaign, Urbana, IL 61801, USA*

⁵*Department of Physics, Princeton University, Princeton, NJ 08544, USA*

⁶*Princeton Center for Theoretical Science, Princeton University, Princeton, NJ 08544, USA*

We present a multimethod investigation into the nature of the recently reported quantum spin liquid (QSL) phase in the spin-1/2 Heisenberg antiferromagnet on the Shastry-Sutherland lattice. A comprehensive projective symmetry group classification of fermionic mean-field *Ansätze* on this lattice yields 46 U(1) and 80 \mathbb{Z}_2 states. Motivated by density-matrix renormalization group (DMRG) calculations suggesting that the Shastry-Sutherland model and the square-lattice J_1 - J_2 Heisenberg antiferromagnet putatively share the same QSL phase, we establish a mapping of our *Ansätze* to those of the square lattice. This enables us to identify the equivalent of the square-lattice QSL (Z2Azz13) in the Shastry-Sutherland system. Employing state-of-the-art variational Monte Carlo calculations with Gutzwiller-projected wavefunctions improved upon by Lanczos steps, we demonstrate the excellent agreement of energies and correlators between a gapless (Dirac) \mathbb{Z}_2 spin liquid—characterized by only few parameters—and approaches based on neural quantum states and DMRG. Furthermore, the real-space spin-spin correlations are shown to decay with the same power law as in the J_1 - J_2 square lattice model, which also hosts a \mathbb{Z}_2 Dirac spin liquid. Finally, we apply the recently developed Keldysh formulation of the pseudo-fermion functional renormalization group to compute the dynamical spin structure factor; these correlations exhibit the features expected due to Dirac cones in the excitation spectrum, thus providing strong independent evidence for a Dirac QSL ground state. Our finding of a d -wave pairing \mathbb{Z}_2 Dirac QSL is consistent with the recently observed signatures of QSL behavior in $\text{Pr}_2\text{Ga}_2\text{BeO}_7$ and outlines predictions for future experiments.

I. INTRODUCTION

The celebrated spin-1/2 Heisenberg antiferromagnet on the Shastry-Sutherland lattice presents a rare example of a two-dimensional spin model which admits an *exact* solution for its ground state [1]. This Archimedean lattice, which is also called the snub square or (3², 4, 3, 4) lattice, features two symmetry-inequivalent bonds, and the Shastry-Sutherland model (SSM) is defined on this lattice as

$$\hat{H} = J_s \sum_{\langle i,j \rangle_{\text{square}}} \hat{\mathbf{S}}_i \cdot \hat{\mathbf{S}}_j + J_d \sum_{\langle i,j \rangle_{\text{dimer}}} \hat{\mathbf{S}}_i \cdot \hat{\mathbf{S}}_j. \quad (1)$$

Here, \mathbf{S}_i denotes the SU(2) spin operator acting on the spin $S=1/2$ representation at site i . The nearest-neighbor antiferromagnetic exchange is given by J_s , with the first sum in Eq. (1) running over all the bonds of the square lattice. The next-nearest-neighbor interaction is represented by J_d and the second sum runs over the additional diagonal bonds introduced on alternating

plaquettes of the square lattice, creating a pattern of orthogonal dimers [see Fig. 1(b)]. In the limit $J_s/J_d = 0$, the Hamiltonian reduces to one consisting of decoupled dimers and the ground state is given by a tensor product of singlets with an energy of $-3/8J_d$ per site. This state is always an exact eigenstate of Eq. (1) and remains the ground state till a finite critical J_s/J_d . The opposite limit, $J_s/J_d \rightarrow \infty$, yields the Heisenberg model on the square lattice, which has a two-sublattice Néel-ordered ground state.

Over the past few decades, the SSM has been the focus of extensive theoretical efforts to map out the phase diagram of Eq. (1), with interest intensifying in particular after the discovery of $\text{SrCu}_2(\text{BO}_3)_2$ [2, 3], which is well approximated by this model¹. Other intriguing compounds in the family of Shastry-Sutherland lattice materials have also attracted much attention lately, due to their promise for hosting exotic nonmagnetic ground states, possibly QSLs, as well as exciting possibilities to realize altermagnetism [5]. These include rare-

* yiqbal@physics.iitm.ac.in

¹ The role of interlayer couplings in accurately describing its behavior has lately been appreciated [4].

earth magnets such as $\text{BaCe}_2\text{ZnS}_5$ [6], $\text{Pr}_2\text{Ga}_2\text{BeO}_7$ [7], $\text{Pr}_2\text{Be}_2\text{GeO}_7$ [8], $\text{Yb}_2\text{Be}_2\text{GeO}_7$ [9], $\text{Er}_2\text{Be}_2\text{SiO}_7$ [10], and $\text{Er}_2\text{Be}_2\text{GeO}_7$ [11, 12].

With regard to the ground-state phase diagram of Eq. (1), while most early works advocated for a direct transition between the dimer and Néel phases [13–15], one of the first studies based on Schwinger boson mean-field theory [16], and subsequent variational calculations [17], found an intermediate state with helimagnetic order, which is known to be the classical ($S \rightarrow \infty$) ground state [1]. Later investigations based on series expansion, stochastic state selection [18], coupled-cluster [19], and perturbative [20, 21] methods introduced the possibility of a gapped nonmagnetic intermediate phase, with either plaquette [22, 23] or columnar [24] valence bond crystal (VBC) order. The presence of plaquette order was subsequently confirmed by a large- N expansion based on a generalization to $Sp(2N)$ symmetry [25], exact diagonalization and a combination of dimer- and quadrumer-boson methods [26], triplon mean-field analysis [27], two-step density-matrix renormalization group (DMRG) [28], and $D = 2$ projected entangled pair states [29]. More recently, numerical quantum many-body approaches using tensor networks [30], DMRG [31], and the pseudo-fermion functional renormalization group [32] have established the presence of a plaquette-ordered ground state. Furthermore, some suggestions hinting at exotic topologically ordered phases have also been made [33, 34].

Nonetheless, a consensus has now emerged that the intermediate phase between the dimer and Néel orders is indeed a plaquette VBC. This VBC breaks reflection symmetry across the lines containing the J_d bonds, implying a twofold degenerate ground state, and features resonating singlets on empty (with no J_d bonds) plaquettes. In $\text{SrCu}_2(\text{BO}_3)_2$, a plaquette VBC, likely ascribed to broken fourfold rotation symmetry about the centers of the empty squares, has been realized under the application of hydrostatic pressure [35, 36]. Thermodynamic measurements under high pressure have also provided evidence for the exciting possibility of a deconfined quantum critical point between Néel order and the plaquette VBC [37].

Theoretical evidence for a continuous transition between the plaquette VBC and Néel-ordered states, and a resultant deconfined quantum critical point (DQCP) exhibiting emergent $O(4)$ symmetry, has been provided by a combination of infinite density-matrix renormalization group (iDMRG) calculations and field-theoretical analysis [31], as well as recent tensor-network studies [38]. Other works have argued for a weak first-order transition between these phases [39–41] and suggested that the DQCP might instead be proximate in parameter space [39, 42]. In contrast to both these scenarios, recent numerical investigations using DMRG [43], exact diagonalization [34, 44, 45], pseudo-fermion functional renormalization group [32], and state-of-the-art neural-network quantum states [46, 47] have all reported the

presence of a QSL phase sandwiched between the plaquette VBC and Néel-ordered states. This QSL phase occupies a narrow parameter range, $0.77 \lesssim J_s/J_d \lesssim 0.82$ [43, 46]. This raises the question of whether one can explore an extended parameter space to widen the window of QSL behavior, and identify its precise microscopic character, i.e., if it is gapped or gapless, as well as the nature of its low-energy gauge group.

In this work, employing DMRG simulations, we show that such a broader island of spin liquidity can be potentially accessed by turning on the antiferromagnetic exchange couplings, henceforth labeled J'_d , on all the “other” diagonal bonds (within the square plaquettes) that were originally excluded in the Shastry-Sutherland geometry. Upon increasing the strength of these additional couplings, we do not find a signature of a phase transition up to the point when $J'_d = J_d$, i.e., in the limit of the J_1 - J_2 model on the square lattice. This hints at the interesting possibility that, if they exist, the QSLs of the two models might be adiabatically connected and in the same phase. Our analysis will show how this observation provides crucial insight into uncovering the microscopic nature of the spin liquid. We emphasize that our results remain agnostic to—and do not rely on—the existence of an extended QSL phase in the pure SSM. Rather, what we demonstrate and focus on is the presence of a QSL phase in the broader parameter space, with J'_d couplings, which we identify to be the same as that observed in the square-lattice model. However, determining whether this island of spin liquidity extends all the way to the $J'_d = 0$ limit of the SSM or terminates beforehand lies beyond the scope of this study.

A. Connection to the square-lattice J_1 - J_2 model

Previous studies using variational Monte Carlo (VMC) [48, 49], many-variable VMC [50], neural-network wavefunctions [51], DMRG [52], and tensor networks [53, 54] have offered evidence for the presence of a gapless spin liquid sandwiched between the Néel and VBC phases in the $S = 1/2$ square-lattice Heisenberg model with nearest-neighbor (J_1) and next-nearest-neighbor (J_2) couplings. On the other hand, as noted above, numerical simulations on the J_s - J_d SSM point to a variety of possibilities, including weakly first-order or continuous phase transitions or a gapless QSL phase. Given the geometric similarity between these two models, we introduce the following Hamiltonian which straightforwardly interpolates between them [39]:

$$\hat{H} = J_s \sum_{\langle i,j \rangle} \hat{\mathbf{S}}_i \cdot \hat{\mathbf{S}}_j + J_d \sum_{\langle\langle i,j \rangle\rangle_{\text{dimer}}} \hat{\mathbf{S}}_i \cdot \hat{\mathbf{S}}_j + J'_d \sum_{\langle\langle i,j \rangle\rangle_{\text{other}}} \hat{\mathbf{S}}_i \cdot \hat{\mathbf{S}}_j, \quad (2)$$

where the $J'_d = 0$ limit corresponds to the SSM and the $J'_d = J_d$ limit corresponds to the J_1 - J_2 model on the square lattice.

In Fig. 1, we illustrate the schematic phase diagram for this Hamiltonian, where the approximate phase boundaries are obtained from iDMRG simulations on an infinite cylinder with a circumference of length $L = 10$ and a bond dimension $\chi = 2000$. In this diagram, the hatched white region indicates a phase in which the simulation converges very slowly (or not at all, to within the conventionally accepted truncation error of 10^{-5}), with Néel and VBC order parameters that are both small and of similar magnitude. Furthermore, along the transverse direction indicated by the arrow in Fig. 1, we find no signatures of any phase transitions. This suggests that if a gapless spin liquid phase exists in the SSM as proposed in Refs. [43, 46], it should be adiabatically connected to the gapless spin liquid phase of the square-lattice J_1 - J_2 model. For the chosen bond dimension, the phase transition between the VBC and Néel phases in the SSM appears to be weakly first-order.

B. Summary of theoretical approach and results

To further explore this hypothesis and shed light on the nature of the QSL in the SSM, we employ the framework of projective symmetry groups (PSGs) [55, 56], described in Sec. IIB (and extensively utilized on many two- and three-dimensional lattices [57–85]), to perform a systematic classification of fermionic mean-field states with $SU(2)$, $U(1)$, and \mathbb{Z}_2 low-energy gauge groups. Since, previous studies [43, 46] have provided evidence for a gapless spin liquid, we choose to employ the fermionic representation of spin operators, as opposed to bosonic, since the former enables a description of gapless QSLs while the latter is restricted to describing only gapped QSLs [82]. Considering QSLs which respect the full space-group symmetry as well as lattice-nematic QSLs compatible with the lower symmetry of the adjacent plaquette VBC, we present the microscopic *Ansätze* describing these states in Sec. III. Then, we develop a mapping between the \mathbb{Z}_2 *Ansätze* on the Shastry-Sutherland and square lattices by establishing a connection between the PSGs of the respective symmetry groups. This approach allows us to systematically narrow down the candidate wavefunctions for the potential QSL in the generalized Shastry-Sutherland model by identifying the parton *Ansätze* that can be adiabatically connected to those of the QSL phase in the J_1 - J_2 model.

In Sec. III C, we analyze the *Ansatz* on the Shastry-Sutherland lattice that maps to the Z2Azz13 state on the square lattice—a gapless (Dirac) \mathbb{Z}_2 QSL, which is believed to provide an excellent variational description of the QSL in the J_1 - J_2 square-lattice Heisenberg model [48, 51]. To characterize this *Ansatz*, we analyze its spinon band structure and compute the mean-field dynamical and equal-time spin structure factors at $J_s/J_d = 0.80$, which lies within the putative QSL phase [32, 43, 44, 46]. We identify the state to be a

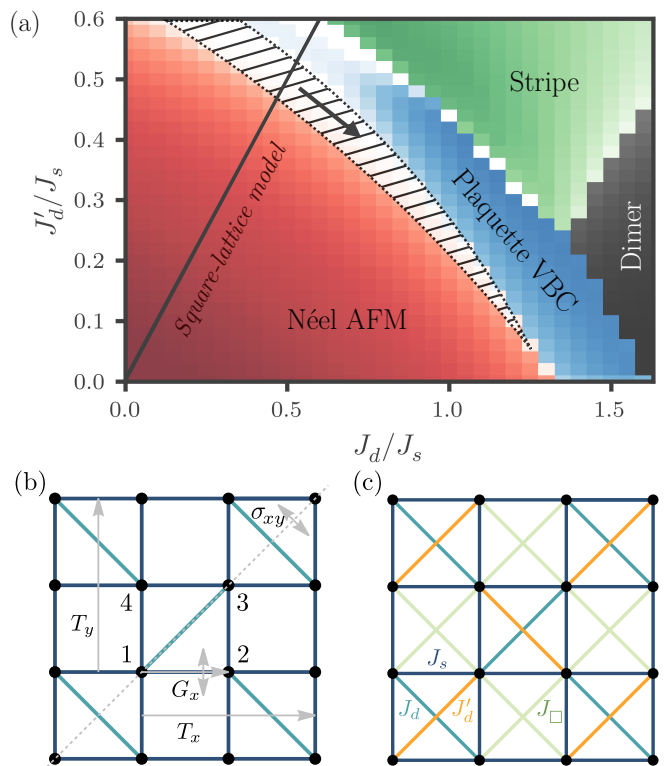


FIG. 1. (a) Schematic ground-state quantum phase diagram of the Hamiltonian (2) interpolating between the square-lattice J_1 - J_2 Heisenberg and Shastry-Sutherland models. The solid line in the figure indicates the parameters of the square-lattice model, while the horizontal axis corresponds to the pure Shastry-Sutherland model. The shading of the color conveys the strength of the appropriate order parameter. The hatched region in the diagram is where iDMRG does not converge well, and which might host a gapless spin liquid phase. (b) Structure of the Shastry-Sutherland lattice, highlighting its space-group symmetries. (c) Mapping of the Shastry-Sutherland lattice to the square lattice. The two additional types of symmetry-inequivalent bonds are denoted by orange and light green lines, respectively. In the square-lattice limit, i.e., $J_d = J'_d = J_\square$, all the diagonal bonds are related by symmetry.

gapless (Dirac) \mathbb{Z}_2 QSL with d -wave pairing and featuring Dirac cones at incommensurate $(\pi/2 \pm \varepsilon, \pi/2 \pm \varepsilon)$ positions, similar to the Z2Azz13 state [56]². Finally, in Sec. IV, we carry out a state-of-the-art variational Monte Carlo study of the corresponding Gutzwiller-projected wavefunctions supplemented with Lanczos steps, and demonstrate the excellent agreement of the energies and equal-time correlators of our \mathbb{Z}_2 Dirac QSL with those obtained from vision transformer (ViT) neural networks,

² In the Z2Azz13 state, the splitting of the Dirac cone into four cones at $(\pi/2 \pm \varepsilon, \pi/2 \pm \varepsilon)$ occurs due to the d_{xy} pairing on the diagonal bonds connecting site $(0, 0)$ to $(\pm 1, \pm 1)$; however, if we instead introduce the pairing on the $(\pm 2, \pm 2)$ bonds, the Dirac cones remain intact at $(\pi/2, \pi/2)$.

DMRG, and exact diagonalization on small clusters. We show that the (equal-time) real-space spin-spin correlations decay with the same exponent $z + \eta \sim 1.5$ as known for the square-lattice QSL. Finally, employing a novel Keldysh formulation of the pseudo-fermion functional renormalization group, we present, hitherto unreported, dynamical spin structure factors of the QSL, which reveal a remarkable consistency with the expectation of a Dirac spin liquid. Taken together, all these pieces provide striking evidence for a \mathbb{Z}_2 Dirac QSL phase in the generalized Shastry-Sutherland model. We emphasize that the projective realizations of the Shastry-Sutherland lattice symmetries are already built into the *Ansätze* and dictate its sign and amplitude structure. Hence, such an approach requires a much smaller number of variational parameters as compared to methods based on neural-network wavefunctions, DMRG, and many-variable VMC that rely on unconstrained optimizations.

In light of recent observations of gapless QSL behavior in $\text{Pr}_2\text{Ga}_2\text{BeO}_7$ [7], which can approximately be modeled by $S = 1/2$ XXZ interactions on the Shastry-Sutherland lattice, our results find additional significance. In particular, our finding of a d -wave pairing \mathbb{Z}_2 Dirac QSL is compatible with the thermodynamic signatures of a T^2 dependence of the specific heat and a finite κ_0/T arising due to a disorder-induced finite density of states [7]. Thus, under the assumption of the continuity of the \mathbb{Z}_2 Dirac QSL upon introducing XXZ anisotropy to the Heisenberg model, our work also potentially clarifies the microscopic identity of the QSL in $\text{Pr}_2\text{Ga}_2\text{BeO}_7$.

II. METHODOLOGY

A. Parton construction

A powerful framework to construct mean-field theories of QSLs is provided by the ‘‘parton’’ representation of spin operators. The first step in this scheme is to express the spin operators \hat{S}^γ ($\gamma = x, y, z$) in terms of spin-1/2, charge-neutral quasiparticles called *spinons*, which can be chosen to have either bosonic or fermionic statistics. As we are interested in describing gapped as well as gapless QSLs and the competition between them, we henceforth consider the spinons to be fermionic. In this language, the spin operator can be rewritten as a bilinear with two flavors of complex fermions [86, 87]:

$$\hat{S}_i^\gamma = \frac{1}{2} \sum_{\alpha\beta} \hat{f}_{i\alpha}^\dagger \tau_{\alpha\beta}^\gamma \hat{f}_{i\beta}. \quad (3)$$

Here, the $\hat{f}_{i\alpha}$ ($\hat{f}_{i\alpha}^\dagger$) are spinon operators which annihilate (create) a spin-1/2 fermion with flavor $\alpha \in \{\uparrow, \downarrow\}$ at site i and τ^γ ($\gamma = x, y, z$) are the three Pauli matrices. In order to make the symmetries of the fermionic representation

manifest, it proves instructive to re-express Eq. (3) as

$$\hat{S}_i^\gamma = \frac{1}{2} \text{Tr} \left[\hat{\psi}_i^\dagger \tau^\gamma \hat{\psi}_i \right] \quad (4)$$

in terms of the spinor doublet $\hat{\psi}_i \equiv (\hat{\mathbf{f}}_i, \hat{\hat{\mathbf{f}}}_i)$, where $\hat{\mathbf{f}}_i = (\hat{f}_{i,\uparrow}, \hat{f}_{i,\downarrow})^\text{T}$ and $\hat{\hat{\mathbf{f}}}_i = (\hat{f}_{i,\downarrow}^\dagger, -\hat{f}_{i,\uparrow}^\dagger)^\text{T}$. Under a right multiplication $\hat{\psi}_i \rightarrow \hat{\psi}_i W_i$ with $W_i \in \text{SU}(2)$, the spin operators in Eq. (4) and the fermionic anticommutation relations of the spinons remain unaffected, i.e., such a transformation does not affect the physical observables. Thus, the fermionization of the spin operators is accompanied by a local gauge freedom associated with an internal symmetry group (ISG) [88, 89], which, in this case, is $\text{SU}(2)$. In distinction to right multiplications, a left $\text{SU}(2)$ multiplication, i.e., $\hat{\psi}_i \rightarrow G \hat{\psi}_i$ effects a rotation in spin space. Moreover, it is important to note that the fermionic Hilbert space is four-dimensional while the spin space is \mathbb{C}^2 . This necessitates the introduction of an additional constraint requiring that there be exactly one fermion per site:

$$\hat{\psi}_i \tau^\gamma \hat{\psi}_i^\dagger = 0, \quad \gamma \in \{x, y, z\}, \quad (5)$$

which ensures that the Hilbert space dimensions of the spin and spinon representations are in agreement.

Inserting Eq. (3) into a generic Heisenberg model such as, say, Eq. (1), yields a four-fermion interaction term in the Hamiltonian, following which, we can perform a mean-field decoupling to obtain an effective quadratic Hamiltonian. Given that we intend to formulate a low-energy Hamiltonian for a spin-rotation-invariant quantum paramagnet, we restrict this decoupling to only the singlet channel. Since a spin rotation is implemented in the fermionic Hilbert space by a left $\text{SU}(2)$ multiplication, the quadratic field $\hat{\psi}_i^\dagger \hat{\psi}_j$ is manifestly spin-rotation invariant. Accordingly, the mean field in the singlet channel can be identified as $u_{ij} = \langle \hat{\psi}_i^\dagger \hat{\psi}_j \rangle$, which, in turn, consists of two subchannels χ_{ij} and Δ_{ij} :

$$u_{ij} = \begin{bmatrix} \chi_{ij} & \Delta_{ij}^\dagger \\ \Delta_{ij} & -\chi_{ij}^\dagger \end{bmatrix}. \quad (6)$$

Here, χ_{ij} and Δ_{ij} are the hopping and pairing singlet mean fields, respectively, which reside on the bond connecting sites i and j . The resulting quadratic spinon Hamiltonian for a quantum paramagnet generically takes the form

$$\begin{aligned} \hat{H}_{\text{MF}} = & \sum_{\langle ij \rangle} \frac{3}{8} J_{ij} \left[\frac{1}{2} \text{Tr}(u_{ij}^\dagger u_{ij}) - \text{Tr}(\hat{\psi}_i u_{ij} \hat{\psi}_j^\dagger + \text{H.c.}) \right] \\ & + \sum_i \sum_\gamma a_{\gamma,i} \text{Tr} \left[\hat{\psi}_i \tau^\gamma \hat{\psi}_i^\dagger \right]. \end{aligned} \quad (7)$$

The term in the second line above incorporates the constraint forbidding empty and doubly occupied sites at the mean-field level, i.e., $\langle \hat{\psi}_i \tau^\gamma \hat{\psi}_i^\dagger \rangle = 0$, using three Lagrange

multipliers a_γ , with $\gamma = x, y, z$, at each site. As the spinon Hamiltonian is completely specified by $(u_{ij}, a_{\gamma,i})$, these fields together constitute an *Ansatz* for a given QSL phase. The mean-field Hamiltonian (7) is now invariant under the following gauge transformations:

$$\hat{\psi}_i \rightarrow \hat{\psi}_i W_i, \quad u_{ij} \rightarrow W_i^\dagger u_{ij} W_j, \quad a_{\gamma,i} \tau^\gamma \rightarrow a_{\gamma,i} W_i^\dagger \tau^\gamma W_i, \quad (8)$$

for $W_i \in \text{SU}(2)$. Therefore, the ISG turns out to also be the gauge-symmetry group in the mean-field construction. Next, we describe how this property leads to nontrivial symmetry operations in the fermionic Hilbert space.

B. Projective symmetry group framework

Fully symmetric QSLs are quantum paramagnets that do not spontaneously break lattice space-group and time-reversal symmetries, and consequently, cannot be characterized by local physical order parameters. In principle, QSLs may break one or more lattice symmetries and time reversal, but they still cannot be uniquely characterized by local order parameters since there can exist a plethora of QSLs breaking the very same symmetries—as occurs for chiral QSLs [68] and spin-/lattice-nematic QSLs [67, 90, 91]. To establish the invariance of an *Ansatz* under different symmetry operations, one therefore has to specify how a lattice or time-reversal symmetry operation acts in the fermionic Hilbert space.

In general, an *Ansatz* given by u_{ij} is modified to $u'_{ij} = u_{\mathcal{O}(i), \mathcal{O}(j)}$ under a symmetry operation denoted by \mathcal{O} , so, at first sight, it appears that the symmetry of the *Ansatz* under \mathcal{O} is broken. However, the $\text{SU}(2)$ gauge symmetry in the fermionic representation implies that two *Ansätze* related by a $\text{SU}(2)$ gauge transformation label the same physical spin state. Thus, if we choose an appropriate local $\text{SU}(2)$ matrix W_i that connects u_{ij} and u'_{ij} , the symmetry of the *Ansatz* can be restored. As a result, lattice and time-reversal symmetries are realized projectively (i.e., up to $\text{SU}(2)$ gauge transformations) in the fermionic Hilbert space. This lays the foundation for the idea of the projective symmetry group (PSG) framework [55], whereby an *Ansatz* is invariant under a symmetry operation \mathcal{O} iff the following condition is satisfied:

$$W_{\mathcal{O}(i)}^\dagger u_{\mathcal{O}(i)\mathcal{O}(j)} W_{\mathcal{O}(j)} = u_{ij}. \quad (9)$$

This combined operation of the physical symmetry element and the element of the ISG defines the PSG of an *Ansatz*. Physically, if two *Ansätze* have gauge-inequivalent PSGs, they correspond to two distinct QSL states. Accordingly, PSGs serve to characterize the internal quantum order of an *Ansatz* [56], i.e., different *Ansätze* can be distinguished and characterized by PSGs in a fashion akin to how classical solid-state phases are characterized by crystallographic space-group symmetries. Hence, a systematic classification of projective representations

of given lattice space groups can serve as a powerful mathematical tool, enabling the construction of distinct QSL *Ansätze* with a desired low-energy gauge group.

To characterize the *Ansätze* in more detail, note that u_{ij} in Eq. (6) can be re-expressed in terms of four real parameters as

$$u_{ij} = i\chi_{ij}^0 \tau^0 + \chi_{ij}^3 \tau^z + \Delta_{ij}^1 \tau^x + \Delta_{ij}^2 \tau^y, \quad (10)$$

where τ^0 is the 2×2 identity matrix. Due to this structure, there always exists a group \mathbb{G} (where \mathbb{G} is either $\text{SU}(2)$ or its subgroups $\text{U}(1)$ and \mathbb{Z}_2) such that under gauge transformations by $\mathcal{G}_i \in \mathbb{G}$, the *Ansatz* remains invariant. The group \mathbb{G} is called the invariant gauge group (IGG) of the *Ansatz*. Another interpretation of the IGG can be seen by comparing Eq. (9) and Eq. (11) below, which implies that the IGG is a special subgroup of the PSG corresponding to an identity symmetry operation ($\mathcal{O} = \mathbf{1}$).

When $u_{ij} = i\chi_{ij}^0 \tau^0$, and $\chi_{ij}^3 = \Delta_{ij}^1 = \Delta_{ij}^2 = 0$, i.e., the *Ansatz* consists of only imaginary hoppings, the IGG is the global $\text{SU}(2)$ gauge group $\{\exp(i\phi \hat{\mathbf{n}} \cdot \hat{\tau})\}$. If we include real hopping terms as well, i.e., $\Delta_{ij}^1 = \Delta_{ij}^2 = 0$, the IGG is the global $\text{U}(1)$ gauge group $\{\exp(i\phi \tau^z)\}$ while the inclusion of pairing terms breaks the IGG down to global \mathbb{Z}_2 , $\{\pm 1\}$. The three different IGGs discussed in this example only involve *global* gauge elements; these correspond to the so-called canonical structures of the *Ansätze*. In canonical form, $\text{SU}(2)$ *Ansätze* contain only imaginary hopping terms, $\text{U}(1)$ *Ansätze* include only real and imaginary hopping amplitudes, and \mathbb{Z}_2 *Ansätze* can take any generic form. However, owing to the $\text{SU}(2)$ gauge redundancy, the elements of the IGG need not always constitute a global gauge group, and the invariance of an *Ansatz* may require the following generic local operation:

$$\mathcal{G}_i^\dagger u_{ij} \mathcal{G}_j = u_{ij}, \quad \mathcal{G} \in \text{IGG}. \quad (11)$$

Thus, in general, the IGG is a *local* gauge group.

C. Symmetries of the Shastry-Sutherland model

The symmetries of the Shastry-Sutherland lattice [see Fig. 1(b)] correspond to the $p4g$ wallpaper group. Let the positions of the lattice sites in the Cartesian coordinate system be denoted by

$$\mathbf{r} \equiv (x, y) \equiv (x\hat{\mathbf{x}} + y\hat{\mathbf{y}})a, \quad (12)$$

where a is the lattice parameter. The symmetry generators and their actions on a lattice site are then as

$w_{\mathcal{T}}$	w_{G_x}	$w_{\sigma_{xy}}$	ξ_y	$\xi_{G_{xy}}$	$\bar{\phi}_{G_x,u}$	$\bar{\phi}_{\sigma_{xy},u}$	# of PSG classes
1	0	0	0	$p_{G_{xy}}\pi$	$\{0, p_{G_x T_x}\pi, 0, p_{G_x T_x}\pi + p_{G_{xy}}\pi\}$	$\{0, 0, p_{\sigma_{xy}}\pi, 0\}$	8
1	0	1	0	$p_{G_{xy}}\pi$	$\{0, p_{G_x T_x}\pi, p_{G_x T_x}\pi - p_{G_{xy}}\pi, 0\}$	$\{0, 0, p_{\sigma_{xy}}\pi, 0\}$	8
1	1	0	0	$p_{G_{xy}}\pi$	$\{0, p_{G_x T_x}\pi, 0, p_{G_x T_x}\pi - p_{G_{xy}}\pi\}$	$\{0, 0, p_{\sigma_{xy}}\pi, 0\}$	8
1	1	1	0	$p_{G_{xy}}\pi$	$\{0, p_{G_x T_x}\pi, 0, p_{G_x T_x}\pi - p_{G_{xy}}\pi\}$	$\{0, 0, p_{\sigma_{xy}}\pi, 0\}$	8
0	0	0	0	0	$\{0, 0, 0, 0\}$	$\{0, 0, p_{\sigma_{xy}}\pi, 0\}$	2
0	0	1	0	0	$\{0, 0, 0, 0\}$	$\{0, 0, p_{\sigma_{xy}}\pi, 0\}$	2
0	1	0	0	$p_{G_{xy}}\pi$	$\{0, p_{G_x T_x}\pi, 0, p_{G_x T_x}\pi - p_{G_{xy}}\pi\}$	$\{0, 0, p_{\sigma_{xy}}\pi, 0\}$	8
0	1	1	$-2\xi_{G_{xy}}$	$\xi_{G_{xy}}$	$\{0, p_{G_x T_x}\pi, 0, p_{G_x T_x}\pi - \xi_{G_{xy}}\}$	0	2

TABLE I. The 46 U(1) PSG classes, characterized by different gauge-inequivalent choices of $w_{\mathcal{O}}$, $\bar{\phi}_{\mathcal{O},u}$, and the U(1) phases ξ_{\dots} . Each vector $\{\dots\}$ lists the four values of $\bar{\phi}_{\mathcal{O},u}$ for $u = 1, \dots, 4$. The parameters p_{\dots} are binary variables, which can be either 0 or 1.

follows [31]:

$$\begin{aligned}
T_x(x, y) &\rightarrow (x + 2, y), \\
T_y(x, y) &\rightarrow (x, y + 2), \\
G_x(x, y) &\rightarrow (x + 1, -y), \\
G_y(x, y) &\rightarrow (-x, y + 1), \\
\sigma_{xy}(x, y) &\rightarrow (y, x), \\
\sigma_{x\bar{y}}(x, y) &\rightarrow (-y + 1, -x + 1), \\
C_4(x, y) &\rightarrow (-y + 2, x - 1).
\end{aligned} \tag{13}$$

Here, T_x and T_y stand for translations by $2a\hat{x}$ and $2a\hat{y}$, respectively, on the underlying Bravais (square) lattice. The operations G_x (G_y) are glide reflections, combining a translation $a\hat{x}$ ($a\hat{y}$) with a reflection across the x - (y -) axis. The symmetries σ_{xy} and $\sigma_{x\bar{y}}$ denote reflections across the two diagonal axes, while C_4 represents fourfold rotations about the centers of the empty squares. Note that T_x , T_y , G_x , $\sigma_{x\bar{y}}$, and C_4 can be expressed in terms of G_x and σ_{xy} as

$$\begin{aligned}
G_y &= \sigma_{xy} G_x \sigma_{xy}, \\
T_x &= G_x^2, \quad T_y = G_y^2, \\
\sigma_{x\bar{y}} &= \sigma_{xy} G_x G_y^{-1}, \\
C_4 &= G_x \sigma_{xy} G_x G_y^{-1} = G_x \sigma_{x\bar{y}}.
\end{aligned} \tag{14}$$

Thus, G_x and σ_{xy} form a minimal set of symmetry generators for the $p4g$ wallpaper group. However, for simplicity, we include the translations T_x and T_y explicitly in the discussion hereafter.

Using the notation (m, n, u) , the position of a lattice site is expressed as:

$$\mathbf{r} \equiv (r, u) \equiv (m, n, u) \equiv 2(m\hat{x} + n\hat{y})a + \epsilon_u, \tag{15}$$

where $u = 1, 2, 3, 4$ labels the four distinct sites within the geometric unit cell, and

$$\epsilon_1 = 0, \quad \epsilon_2 = a\hat{x}, \quad \epsilon_3 = a(\hat{x} + \hat{y}), \quad \epsilon_4 = a\hat{y}. \tag{16}$$

The symmetry operations, in this notation, are defined as:

$$\begin{aligned}
T_x &: (m, n, u) \rightarrow (m + 1, n, u), \\
T_y &: (m, n, u) \rightarrow (m, n + 1, u), \\
G_x &: (m, n, u) \rightarrow (m + \delta_{u,2/3}, -n - \delta_{u,3/4}, G_x(u)), \\
\sigma_{xy} &: (m, n, u) \rightarrow (n, m, \sigma_{xy}(u)),
\end{aligned} \tag{17}$$

where $\delta_{u,a/b} \equiv \delta_{u,a} + \delta_{u,b}$, $G_x(\{1, 2, 3, 4\}) = (\{2, 1, 4, 3\})$, and $\sigma_{xy}(\{1, 2, 3, 4\}) = (\{1, 4, 3, 2\})$.

In addition to the space-group symmetries, we need to consider time reversal \mathcal{T} given that we are dealing with fully symmetric QSL *Ansätze*. Being an internal symmetry, \mathcal{T} leaves (m, n, u) unchanged and commutes with all space-group operations. Taking \mathcal{T} into account, the symmetry group of the Shastry-Sutherland lattice is then fully specified by the following identity relations:

$$\begin{aligned}
T_x^{-1} T_y^{-1} T_x T_y &= \mathbf{1}, \\
G_x^{-1} T_x^{-1} G_x T_x &= \mathbf{1}, \\
G_x^{-1} T_y^{-1} G_x T_y &= \mathbf{1}, \\
T_x^{-1} G_x^2 &= \mathbf{1}, \\
T_y^{-1} \sigma_{xy}^{-1} T_x \sigma_{xy} &= \mathbf{1}, \\
T_x^{-1} \sigma_{xy}^{-1} T_y \sigma_{xy} &= \mathbf{1}, \\
(\sigma_{xy} G_x)^4 &= \mathbf{1}, \\
\sigma_{xy}^2 &= \mathbf{1}, \\
\mathcal{T}^2 &= \mathbf{1}, \\
\mathcal{T} \mathcal{O} \mathcal{T}^{-1} \mathcal{O}^{-1} &= \mathbf{1}, \quad \mathcal{O} \in \{T_x, T_y, G_x, \sigma_{xy}\}.
\end{aligned} \tag{18}$$

Finally, time-reversal symmetry acts nontrivially on the mean fields, as $\mathcal{T}(u_{ij}, a_\gamma) = -(u_{ij}, a_\gamma)$ [55, 68]. This imposes the condition

$$W_{\mathcal{T}}^\dagger(i) u_{ij} W_{\mathcal{T}}(j) = -u_{ij}, \tag{19}$$

where $W_{\mathcal{T}} \in \text{SU}(2)$ is a site-dependent gauge transformation.

Since the physical symmetries act projectively in the fermionic Hilbert space, the group relations of Eq. (18), which are generically of the type

$$\mathcal{O}_1 \circ \mathcal{O}_2 \circ \dots = 1, \quad (20)$$

naturally translate to gauge-enriched group compositions of the type

$$\tilde{\mathcal{O}}_1 \circ \tilde{\mathcal{O}}_2 \circ \dots = (W_{\mathcal{O}_1} \circ \mathcal{O}_1) \circ (W_{\mathcal{O}_2} \circ \mathcal{O}_2) \circ \dots = \mathcal{G}, \quad (21)$$

where $\mathcal{G} \in \text{IGG}$ is a pure gauge transformation which reduces to the identity operation for spins. The complete set of PSG solutions can be obtained using the relations in Eq. (18).

Let us first consider the case where the IGG is $U(1)$. The generic form of a $U(1)$ PSG solution for any symmetry operator \mathcal{O} , in the canonical gauge, is given by $W_{\mathcal{O}}(m, n, u) = F_3(\phi_{\mathcal{O}}(m, n, u))(i\tau^x)^{w_{\mathcal{O}}}$, where $F_3(\lambda) \equiv \exp(i\lambda\tau^z)$, and $w_{\mathcal{O}}$ takes the values 0 and 1. However, due to the consistency conditions on G_x arising from the relations (18), there exist no solutions with $w_{\mathcal{O}} = 1$ for $\mathcal{O} \in \{T_x, T_y\}$. The solutions for $\phi_{\mathcal{O}}(m, n, u)$ can be written as

$$\phi_{T_x}(m, n, u) = y\xi_y, \quad \phi_{T_y}(m, n, u) = 0, \quad (22)$$

$$\phi_{G_x}(m, n, u) = (-1)^{w_{G_x}}(n\xi_{G_{xy}} + m\xi_y\delta_{u,3/4}) + \bar{\phi}_{G_x,u}, \quad (23)$$

$$\phi_{\sigma_{xy}}(m, n, u) = mn\xi_y + \bar{\phi}_{\sigma_{xy},u}, \quad (24)$$

$$\phi_{\mathcal{T}}(m, n, u) = u\pi\delta_{w_{\mathcal{T}},0}, \quad (25)$$

with $\bar{\phi}_{\mathcal{O},u} \equiv \phi_{\mathcal{O}}(0, 0, u)$; for details, refer to Appendix B. The different gauge-inequivalent choices of the phases $0 \leq \xi_y, \xi_{G_{xy}}, \bar{\phi}_{G_x,u}, \bar{\phi}_{\sigma,u} < 2\pi$ are listed in Table I. We find a total of 46 $U(1)$ solutions that can be realized on the Shastry-Sutherland lattice.

When the IGG is \mathbb{Z}_2 , an identity can be defined up to a global sign in the canonical gauge. The solutions for the \mathbb{Z}_2 PSGs (for details, see Appendix C) can be expressed as

$$W_{T_x}(m, n, u) = W_{T_y}(m, n, u) = \tau^0, \quad (26)$$

$$W_{G_x}(m, n, u) = \eta_{G_{xy}}^n \mathcal{W}_{G_x,u}, \quad (27)$$

$$W_{\sigma_{xy}}(m, n, u) = \mathcal{W}_{\sigma_{xy},u}, \quad (28)$$

$$W_{\mathcal{T}}(m, n, u) = \mathcal{W}_{\mathcal{T},u}, \quad (29)$$

where $\eta_{G_{xy}} = \pm$ and the matrices $\mathcal{W}_{\mathcal{O},u} = W_{\mathcal{O}}(0, 0, u)$ matrices can be read off from Table II. While there are $2^4 \times 5 = 80$ \mathbb{Z}_2 PSGs in total, for the $\eta_{G_x\mathcal{T}} = 1$ class—in the first and fifth rows of Table II—the first-neighbor mean-field amplitudes vanish, so we need to consider only 64 \mathbb{Z}_2 PSGs.

No.	$\mathcal{W}_{\sigma_{xy},u}$	$\mathcal{W}_{\mathcal{T},u}$
1	$\{\tau^0, \tau^0, \eta_{\sigma}\tau^0, \tau^0\}$	$\{\tau^0, \eta_{G_x\mathcal{T}}\tau^0, \tau^0, \eta_{G_x\mathcal{T}}\tau^0\}$
2	$\{\tau^0, \tau^0, \eta_{\sigma}\tau^0, \tau^0\}$	$\{i\tau^y, \eta_{G_x\mathcal{T}}i\tau^y, i\tau^y, \eta_{G_x\mathcal{T}}i\tau^y\}$
3	$\{i\tau^z, i\tau^z, \eta_{\sigma}i\tau^z, i\tau^z\}$	$\{i\tau^y, \eta_{G_x\mathcal{T}}i\tau^y, i\tau^y, \eta_{G_x\mathcal{T}}i\tau^y\}$
4	$\{i\tau^z, i\tau^z, \eta_{\sigma}i\tau^z, i\tau^z\}$	$\{i\tau^z, \eta_{G_x\mathcal{T}}i\tau^z, i\tau^z, \eta_{G_x\mathcal{T}}i\tau^z\}$
5	$\{i\tau^z, i\tau^z, \eta_{\sigma}i\tau^z, i\tau^z\}$	$\{\tau^0, \eta_{G_x\mathcal{T}}\tau^0, \tau^0, \eta_{G_x\mathcal{T}}\tau^0\}$

TABLE II. Different gauge-inequivalent choices of the matrices $\mathcal{W}_{\sigma_{xy}}$ and $\mathcal{W}_{\mathcal{T}}$ appearing in Eqs. (28) and (29). In addition, Eq. (27) features a third such matrix, which is given by $\mathcal{W}_{G_x,u} = \{\tau^0, \eta_{G_x\mathcal{T}}\tau^0, \tau^0, \eta_{G_x\mathcal{T}}\eta_{G_{xy}}\tau^0\}$ for each row.

III. MEAN-FIELD ANSÄTZE

Having worked out the complete set of PSGs for the Shastry-Sutherland lattice, we are now in a position to derive the different realizable symmetric mean-field *Ansätze* from these PSG solutions. Restricting the mean-field amplitudes to square-lattice bonds (nearest neighbor, NN) and diagonal bonds (next-nearest neighbor, NNN) *only*, we find a total of twelve $U(1)$ and eighteen \mathbb{Z}_2 distinct *Ansätze*. In addition to their PSGs, all the *Ansätze* can be further characterized by defining $SU(2)$ flux operators [55, 68], which are associated with different loops originating from a fixed base point i :

$$P_{\mathcal{C}_i} = u_{ij}u_{jk} \dots u_{li}, \quad (30)$$

where j, k, l, \dots denote the sites included in the contour \mathcal{C}_i . Under a local $SU(2)$ gauge transformation $W(i)$, the flux operator transforms as $P_{\mathcal{C}_i} \rightarrow W^\dagger(i)P_{\mathcal{C}_i}W(i)$, which affects all loop operators with the same base point only up to a global rotation in Pauli space. This property provides a powerful tool for diagnosing different QSL *Ansätze*. In general, for a q -sided loop, $P_{\mathcal{C}_i}$ takes the form:

$$P_{\mathcal{C}_i}(\varphi_{\mathcal{C}_i,i}) \propto g_i e^{i\varphi_{\mathcal{C}_i}\tau^z} (\tau^z)^q g_i^\dagger, \quad g_i \in SU(2), \quad (31)$$

where the phase $\varphi_{\mathcal{C}_i}$ can be interpreted as a magnetic flux threading the loop \mathcal{C}_i .

Furthermore, note that the IGG of an *Ansatz* may not be obvious if the *Ansatz* is not in the canonical gauge. In that case, the disguised IGG for an *Ansatz* written in a generic gauge can be identified from the condition [68]:

$$[\mathcal{G}, P_{\mathcal{C}_i}] = 0,$$

for $\mathcal{G} \in \text{IGG}$ and all nontrivial flux loops $\{P_{\mathcal{C}_i}\}$. In the context of the Shastry-Sutherland lattice, starting from a base site at the origin, we identify four square loops and three triangular loops as illustrated in Fig. 2(a). The associated gauge fluxes are denoted by $\varphi_{s_1}, \varphi_{s_2}, \varphi_{s_3}, \varphi_{s_4}, \varphi_{t_1}, \varphi_{t_2}$, and φ_{t_3} , respectively.

In the following, we now discuss the QSL mean-field *Ansätze* for different IGGs. All these *Ansätze* are defined by simply considering the reference bonds shown in Fig. 2(b).

A. U(1) *Ansätze* on the Shastry-Sutherland lattice

To begin, we consider the different *Ansätze* realizable with IGG U(1). In this family, we demarcate the U(1) PSG solutions into eight different classes, denoted as U1, U2, ..., U8, corresponding to the eight rows in Table I. The states are labeled by their respective classes and the parameters of the PSG as ‘‘Class $\xi_{G_{xy}} \bar{\phi}_{\sigma_{xy}}$ ’’, where $\bar{\phi}_{\sigma_{xy}} = p_{\sigma_{xy}} \pi$. The flux patterns of all the U(1) *Ansätze* are depicted in Fig. 3.

The class U1 yields four distinct *Ansätze* labeled as U100, U1 π 0, U10 π , and U1 $\pi\pi$. Notably, for U10 π , the mean-field amplitudes on the diagonal bonds vanish due to symmetry, and a uniform π -flux threads all the plaquettes, corresponding to a QSL with an SU(2) IGG realized on the square lattice [55].

Next, the four *Ansätze*, labeled as U300, U3 π 0, U30 π , and U3 $\pi\pi$, belong to the class U3. The symmetry-allowed mean fields for U30 π and U3 $\pi\pi$ are identical to those of U10 π and U1 $\pi\pi$, respectively. However, the U3 class has a staggered chemical potential, whereas the chemical potential is uniform for the U1 class. Both the U1 and U3 classes of *Ansätze* consist of real hopping terms only.

Additionally, we identify a few more classes of U(1) *Ansätze*, labeled as U500, U50 π , U600, U60 π , and U8 $\xi\rho$. In these cases, the mean-field amplitudes vanish on the diagonal bonds, as does the onsite potential, while the square bonds include both real and imaginary hopping terms. Note that for the U5 class *Ansätze*, a nontrivial flux, i.e., $\neq 0, \pi$ threads the empty squares of the Shastry-Sutherland lattice, while for the U6 class a nontrivial flux threads those squares of the Shastry-Sutherland lattice which would have otherwise featured a diagonal bond. Up to NN bonds, these two classes of *Ansätze* are equivalent.

The U8 ξ 0 class (with $\xi \equiv \xi_{G_{xy}}$), in particular, incorporates a series of mean-field *Ansätze*. The explicit structure of the mean-field amplitudes in this case is given by:

$$\begin{aligned} u_s &= i\chi_s^0 \tau^0 + \chi_s^3 \tau^z = u_{12} = -u_{14}^\dagger = -u_{23} \\ &= u_{43}^\dagger = -u_{21}^\dagger = u_{41} = F_3(\xi) u_{32}^\dagger = -F_3(\xi) u_{34}. \end{aligned} \quad (32)$$

The bonds u_{41} and u_{32} are modified under a translation T_x , while all other bonds remain invariant:

$$\begin{aligned} u_{41}(x, y) &= u_{(m,n,4),(m,n+1,1)} = F_3(2n\xi) u_{41}, \\ u_{32}(x, y) &= u_{(m,n,3),(m,n+1,2)} = F_3(2n\xi) u_{32}. \end{aligned} \quad (33)$$

To realize such an *Ansatz* on a finite lattice, one must impose the constraint

$$\xi = \xi_{G_{xy}} = \frac{\mathcal{P}}{\mathcal{Q}} \pi, \quad \text{with } \mathcal{P}, \mathcal{Q} \in \mathbb{Z}. \quad (34)$$

Thus, for each choice $\mathcal{P}/\mathcal{Q} \in (0, 1)$, Eq. (34) provides a realization of at least one fully symmetric mean-field

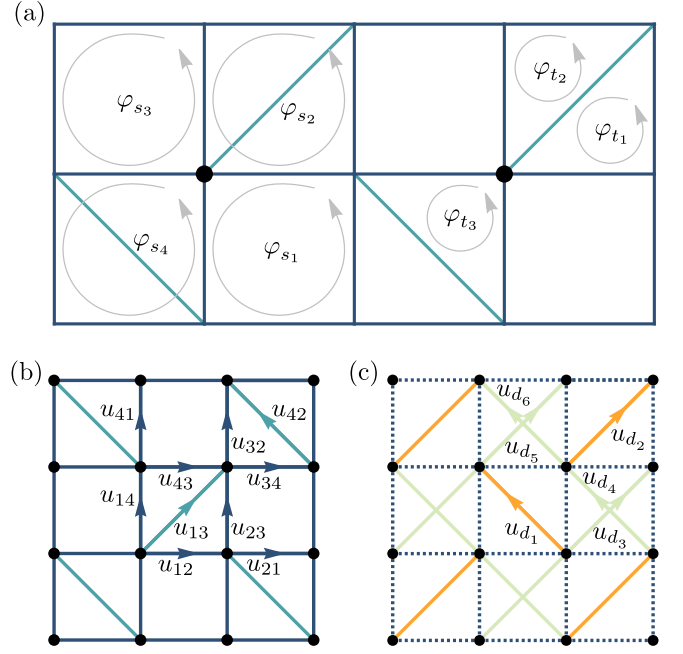


FIG. 2. (a) Illustration of the different SU(2) fluxes which characterize the U(1) *Ansätze*, defined with respect to a ‘‘base site’’ denoted by a black circle. The two such circles shown here are, in fact, equivalent. (b) Definition of mean-field amplitudes on the links of the Shastry-Sutherland lattice within a unit cell, and (c) the labeling convention for the additional diagonal bonds.

QSL within this PSG class, and in total, there exist an infinite number of such QSLs [55].

Lastly, we note that U(1) *Ansätze* in classes U2, U4, and U7 cannot be realized with up to only NNN bonds.

B. \mathbb{Z}_2 *Ansätze* on the Shastry-Sutherland lattice

Although there exist a total of 64 projective extensions of the symmetry group with IGG \mathbb{Z}_2 , only 18 of these can be realized when restricting the *Ansätze* to NNN mean-field amplitudes. The symmetric \mathbb{Z}_2 *Ansätze* have the following structure:

$$u_s = i\chi_s^0 \tau^0 + \Delta_s^1 \tau^x + \Delta_s^2 \tau^y + \chi_s^3 \tau^z, \quad (35)$$

$$u_{12} = \eta_\sigma u_{43}^\dagger = \eta_{G_x T_x} u_{21} = \eta_{G_x T_x} \eta_\sigma \eta_{G_{xy}} u_{34}^\dagger = u_s, \quad (36)$$

$$u_{14} = u_{23}^\dagger = \eta_{G_x T_x} u_{41} = \eta_{G_x T_x} \eta_{G_{xy}} u_{32}^\dagger = (\tau^z)^p u_s (\tau^z)^p, \quad (37)$$

$$u_{13} = u_{42} = u_d = i\chi_d^0 \tau^0 + \Delta_d^1 \tau^x + \Delta_d^2 \tau^y + \chi_d^3 \tau^z, \quad (38)$$

$$a_\gamma(i) \tau^\gamma = a_1 \tau^x + a_2 \tau^y + a_3 \tau^z; \quad (39)$$

here, $p \equiv 0(1)$ for $\mathcal{W}_{\sigma_{xy}, u} \propto \tau^{0(3)}$. In the equations above, the sign parameter $\eta_{G_x T_x}$ is irrelevant because up to NNNs, *Ansätze* with positive and negative $\eta_{G_x T_x}$ are related by a gauge transformation.

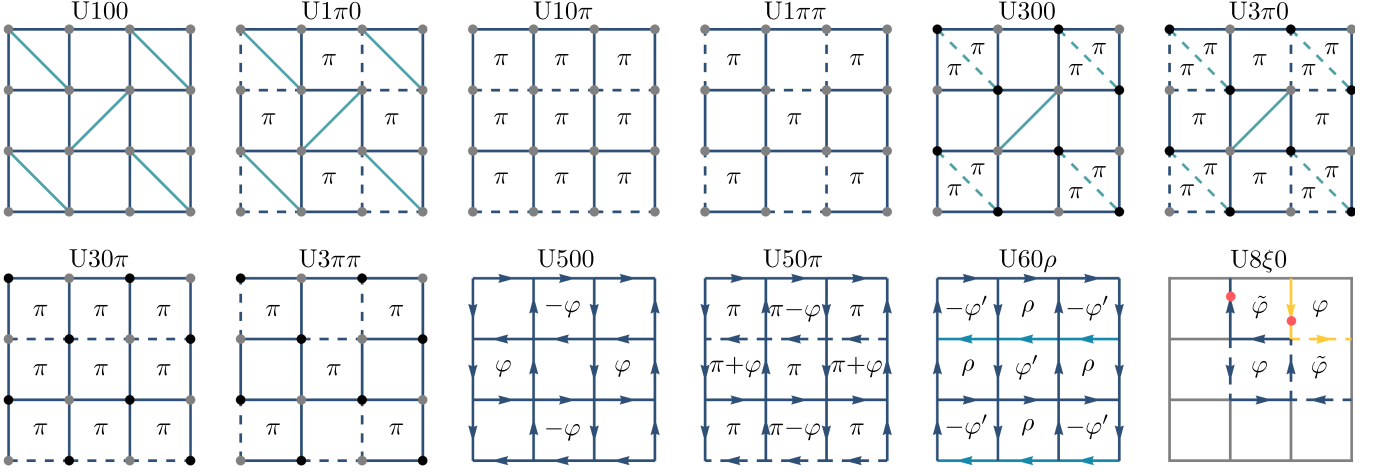


FIG. 3. Sign structure and flux patterns for all U(1) *Ansätze*. Gray (black) dots on the lattice sites denote positive (negative) signs of the onsite chemical potential. The solid (dashed) lines represent an overall positive (negative) signs of the hoppings. Among these *Ansätze*, the ones in the U1 and U3 classes consist of only real hoppings; the U5, U6, and U8 classes feature complex hoppings, so we label the directions of the link fields u_{ij} by arrows. The link fields on dark-blue bonds are defined as $u_s = i\chi_s^0\tau^0 + \chi_s^3\tau^z$. On the light-blue (in U60 ρ) and orange (in U8 ξ 0) bonds, the link fields are given by $F_3(\rho = p_{\sigma_{xy}}\pi)u_s$ and $F_3(\xi = \xi_{G_{xy}})u_s$, respectively, where $F_3(\lambda) \equiv \exp(i\lambda\tau^z)$. For plaquettes with nonzero fluxes, we note the corresponding flux values $\varphi = \text{Arg}[u_s^4]$, $\varphi' = \phi + \text{Arg}[\rho] = \varphi + \text{Arg}[p_{\sigma_{xy}}\pi]$, and $\tilde{\varphi} = -\varphi + \xi = -\varphi + \xi_{G_{xy}}$, where $\xi_{G_{xy}} = \mathcal{P}\pi/\mathcal{Q}$, for $\mathcal{P}, \mathcal{Q} \in \mathbb{Z}$. In the U8 ξ 0 *Ansatz*, the two vertical bonds marked by a red dot are modified by a 2×2 U(1) matrix—specified in Eq. (33)—under translations along \hat{x} , while all other bonds are translation invariant.

Label	u_s	u_d	Onsite	Parent U(1)
Z2000	$\tau^{z,x}$	$\tau^{z,x}$	τ^z	U100, U300
Z2100	$\tau^{z,x}$	$\tau^{z,x}$	τ^z	U1 π 0, U3 π 0
Z2001	$\tau^{0,y}$	$\tau^{z,x}$	τ^z	U100, U300, U500
Z2101	$\tau^{0,y}$	$\tau^{z,x}$	τ^z	U1 π 0, U3 π 0
Z2011	$\tau^{0,y}$	0	τ^z	U10 π , U30 π , U50 π
Z2111	$\tau^{0,y}$	0	τ^z	U1 π π , U3 π π
Z3000	$\tau^{x,z}$	τ^z	τ^z	U100, U300, U800
Z3100	$\tau^{x,z}$	τ^z	τ^z	U1 π 0, U3 π 0, U8 π 0
Z3010	$\tau^{x,z}$	0	τ^z	U10 π , U30 π , U800
Z3110	$\tau^{x,z}$	0	τ^z	U1 π π , U3 π π , U8 π 0
Z3001	$\tau^{0,y}$	τ^z	τ^z	U100, U300, U600
Z3101	$\tau^{0,y}$	τ^z	τ^z	U1 π 0, U3 π 0
Z3011	$\tau^{0,y}$	0	τ^z	U10 π , U30 π , U60 π
Z3111	$\tau^{0,y}$	0	τ^z	U1 π π , U3 π π
Z5001	$\tau^{0,x,z}$	0	0	U500, U600, U800
Z5101	$\tau^{0,x,z}$	0	0	U8 π 0
Z5011	$\tau^{0,x,z}$	0	0	U50 π , U60 π , U800
Z5111	$\tau^{0,x,z}$	0	0	U8 π 0

TABLE III. Mean-field parameters on the reference bonds, u_s and u_d , for all possible symmetric \mathbb{Z}_2 *Ansätze* on the Shastry-Sutherland lattice.

We label the *Ansätze* using the scheme

$$\mathbb{Z} \text{ PSG}_{\text{row}} \left(\frac{1 - \eta_{G_{xy}}}{2} \right) \left(\frac{1 - \eta_{\sigma}}{2} \right) \left(\frac{1 - \eta_{G_x \mathcal{T}}}{2} \right), \quad (40)$$

where PSG_{row} corresponds to the row number in Table II.

Upon restricting ourselves to only J_s and J_d bonds, a total of 18 different symmetric *Ansätze* with IGG \mathbb{Z}_2 can be realized—these are listed in Table III. They are also graphically represented in Fig. 4(a), omitting the parameter $\eta_{G_x \mathcal{T}_x}$ for simplicity. However, this parameter does become important when establishing a connection of our PSGs with those on the square lattice, as discussed in the following section.

C. Mapping to square-lattice \mathbb{Z}_2 *Ansätze*

In this section, we show how the \mathbb{Z}_2 QSL *Ansätze* on the Shastry-Sutherland lattice can be continuously connected to \mathbb{Z}_2 *Ansätze* realizable on the square lattice [55].

The square lattice has a higher symmetry than the Shastry-Sutherland. The space group of the square lattice is $p4$, which is generated by two translations $T_1 = a\hat{x}$, $T_2 = a\hat{y}$, and three reflections σ_{xy} , σ_x , and σ_y about the $x = y$, $y = 0$, and $x = 0$ lines, respectively. As we show here, including σ_x transforms the space group $p4g$ of the Shastry-Sutherland lattice into $p4$. The reflection σ_x transforms the coordinate (x, y) to $(x, -y)$ and acts on (m, n, u) as

$$\sigma_x : (m, n, u) \rightarrow (m, -n - \delta_{u,3/4}, u). \quad (41)$$

One can verify that the other generators of the square

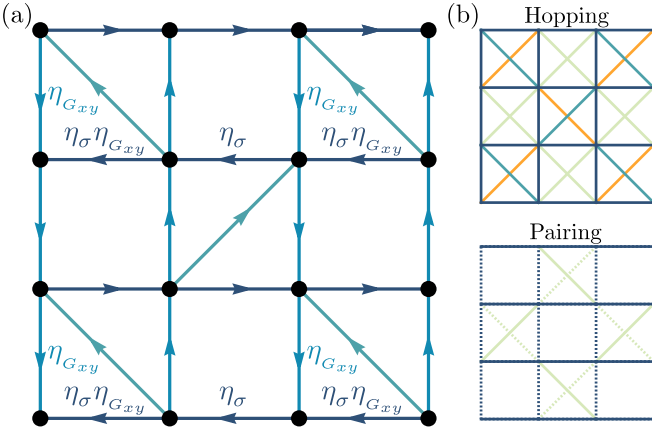


FIG. 4. (a) Graphical representation of \mathbb{Z}_2 *Ansätze*. Here, the link fields on the dark-blue (horizontal) bonds are u_s , and the link fields \tilde{u}_s on the light-blue (vertical) bonds are related to u_s as $\tilde{u}_s = (\tau^z)^p u_s (\tau^z)^p$, where $p=0(1)$ for $\mathcal{W}_{\sigma_{xy}, u} \propto \tau^{0(z)}$. The teal (diagonal) bonds carry a link field u_d . All the *Ansätze* are translationally invariant. (b) Structure of the QSL *Ansatz* Z3000. The top figure conveys the signs of the hopping fields with the hopping amplitudes on the blue, teal, orange, and green bonds given by χ_s , χ_d , $\chi_{d'}$, and χ_\square , respectively. The bottom figure shows the sign structure of the pairing field, which has d -wave symmetry, and the pairing amplitudes on the blue and green bonds are given by Δ_s and Δ_\square , respectively. Dashed bonds denote a negative sign for the pairing.

lattice can be obtained as follows:

$$\begin{aligned} T_1 &= G_x \sigma_x, \\ T_2 &= \sigma_{xy} G_x \sigma_x \sigma_{xy} = \sigma_{xy} T_1 \sigma_{xy}, \\ \sigma_y &= \sigma_{xy} \sigma_x \sigma_{xy}. \end{aligned} \quad (42)$$

Hence, the space group $p4$ is generated by $\{G_x, \sigma_{xy}, \sigma_x\}$. Using this symmetry group, we establish a mapping from the Shastry-Sutherland lattice PSGs to the square-lattice PSGs in Appendix D. We find that upon including σ_x , the *Ansätze* belonging to the $\eta_{G_{xy}} = -1$ class have to be excluded as we are incorporating a larger set of symmetries. Note that this class is also the one which yields $(0, \pi, 0, \pi)$ - and $(\pi, 0, \pi, 0)$ -flux phases in the Shastry-Sutherland lattice, while such staggered-flux phases are forbidden on the square lattice [55]. All things considered, we arrive at the 272 PSGs found in Ref. 55.

Next, we discuss how the \mathbb{Z}_2 *Ansätze* in the class $\eta_{G_{xy}} = +1$ can be mapped to those on the square lattice. To do so, we first implement the geometric mapping between the two lattices as illustrated in Fig. 1(c). Beginning with the Shastry-Sutherland lattice, we have to include two additional symmetry-inequivalent diagonal interactions, denoted by orange and light green bonds (with coupling strengths J'_d and J_\square), respectively. This introduces six new mean-field amplitudes u_{d_1}, \dots, u_{d_6} , as shown in Fig. 2(c). The full *Ansatz* can, in fact, be defined in terms of four fields: u_s , on the NN square bonds;

Label	u_s	u_d	$u_{d'}$	u_\square	Onsite
Z2000	$\tau^{z,x}$	$\tau^{z,x}$	$\tau^{z,x}$	$\tau^{z,x}$	τ^z
Z2100	$\tau^{z,x}$	$\tau^{z,x}$	$\tau^{z,x}$	0	τ^z
Z2001	$\tau^{0,y}$	$\tau^{z,x}$	$\tau^{z,x}$	$\tau^{z,x}$	τ^z
Z2101	$\tau^{0,y}$	$\tau^{z,x}$	$\tau^{z,x}$	0	τ^z
Z2011	$\tau^{0,y}$	0	0	0	τ^z
Z2111	$\tau^{0,y}$	0	0	$\tau^{z,x}$	τ^z
Z3000	$\tau^{x,z}$	τ^z	τ^z	$\tau^{z,x}$	τ^z
Z3100	$\tau^{x,z}$	τ^z	τ^z	0	τ^z
Z3010	$\tau^{x,z}$	0	0	0	τ^z
Z3110	$\tau^{x,z}$	0	0	$\tau^{z,x}$	τ^z
Z3001	$\tau^{0,y}$	τ^z	τ^z	$\tau^{z,x}$	τ^z
Z3101	$\tau^{0,y}$	τ^z	τ^z	0	τ^z
Z3011	$\tau^{0,y}$	0	0	0	τ^z
Z3111	$\tau^{0,y}$	0	0	$\tau^{z,x}$	τ^z
Z5001	$\tau^{0,x,z}$	0	0	0	0
Z5101	$\tau^{0,x,z}$	0	0	0	0
Z5011	$\tau^{0,x,z}$	0	0	0	0
Z5111	$\tau^{0,x,z}$	0	0	0	0

TABLE IV. Extension of all the symmetric \mathbb{Z}_2 *Ansätze* listed in Table III to the other diagonals—that were not originally included in the Shastry-Sutherland lattice—on which the reference bonds are denoted as $u_{d'}$ and u_\square [see Eqs. (43)-(45)]. Here, $u_{d'}$ corresponds to the diagonal bonds in the same set of plaquettes as u_d , and u_\square represents the diagonal bonds in the empty Shastry-Sutherland plaquettes.

u_d , on the diagonal bonds already present on the Shastry-Sutherland lattice; $u_{d'}$, on the other diagonal bonds in the same set of plaquettes as u_d ; and u_\square , on both the diagonal bonds in the empty Shastry-Sutherland plaquettes. The structure of the \mathbb{Z}_2 *Ansätze* with $p4g$ symmetry on these reference bonds are then given by

$$u_{d'} = u_{d_1} = u_{d_2} = i\chi_{d'}^0 \tau^0 + \Delta_{d'}^1 \tau^x + \Delta_{d'}^2 \tau^y + \chi_{d'}^3 \tau^z, \quad (43)$$

$$u_\square = u_{d_3} = (\tau^z)^p u_{d_4} (\tau^z)^p = (\tau^z)^p u_{d_5} (\tau^z)^p = u_{d_6}, \quad (44)$$

where

$$u_\square \equiv i\chi_\square^0 \tau^0 + \Delta_\square^1 \tau^x + \Delta_\square^2 \tau^y + \chi_\square^3 \tau^z. \quad (45)$$

The mean-field parameters u_s , u_d , $u_{d'}$, and u_\square are listed in Table IV. Note, that due to the inclusion of *all* diagonal bonds, the different signs of $\eta_{G_x T_x}$ are no longer related by gauge transformations.

In general, u_d , $u_{d'}$, and u_\square are not related by symmetry. However, in the square-lattice limit (after including σ_x), i.e., $J_d = J'_d = J_\square$, all diagonal bonds do become symmetry equivalent. This allows us to construct \mathbb{Z}_2 *Ansätze* on the square lattice starting from the ones on the Shastry-Sutherland lattice. For example, consider the *Ansatz* labeled Z3000 and PSG 3(c) with $\eta_{G_x T_x} = -\eta_{\sigma_x G_x} = +1$ in Table IX. After imposing the

\mathbb{Z}_2 Ansatz ($p4g$)	PSG	$(\eta_{G_x T_x}, \eta_{\sigma_x G_x})$	\mathbb{Z}_2 Ansatz ($p4$)
Z3000	3a	(+, +)	Z2A0013
Z3000	3c	(+, -)	Z2Azz13
Z3010	3a	(+, +)	Z2B0013
Z2000	2b	(+, -)	Z2Axx0z
Z5011	5d	(-, +)	Z2Ax2(12)n
Z5001	5d	(-, +)	Z2Bx2(12)n

TABLE V. Mapping between the $p4g$ -symmetric \mathbb{Z}_2 Ansatz (left column) and $p4$ -symmetric \mathbb{Z}_2 Ansätze (right column). The second and third columns tabulate the PSG parameters (see Appendix D) that make the connection between the two sets of Ansatz.

constraints associated with σ_x , we obtain the following Ansatz:

$$u_{12} = u_{21} = u_{43} = u_{34} = \chi_s \tau^z + \Delta_s \tau^x, \quad (46a)$$

$$u_{14} = u_{41} = u_{23} = u_{32} = \chi_s \tau^z - \Delta_s \tau^x, \quad (46b)$$

$$u_{13} = u_{42} = u_{d_1} = u_{d_2} = \chi_d \tau^z, \quad a_\gamma(u) = 0, \quad (46c)$$

$$u_{d_3} = u_{d_4} = u_{d_5} = u_{d_6} = -\chi_d \tau^z. \quad (46d)$$

It is straightforward to see that after a gauge transformation $W(m, n, u) = \{i\tau^y, -1, -i\tau^y, 1\}$, this can be re-expressed as:

$$u_{12} = u_{21} = u_{43} = u_{34} = \chi_s \tau^z - \Delta_s \tau^x, \quad (47a)$$

$$u_{14} = u_{41} = u_{23} = u_{32} = \chi_s \tau^z + \Delta_s \tau^x, \quad (47b)$$

$$u_{13} = u_{d_2} = u_{d_3} = u_{d_5} = \chi_d \tau^z, \quad a_\gamma(u) = 0, \quad (47c)$$

$$u_{42} = u_{d_1} = u_{d_4} = u_{d_6} = -\chi_d \tau^z. \quad (47d)$$

In the canonical square-lattice Cartesian notation, it can be written as

$$u_{\hat{x}} = \chi_s \tau^z - \Delta_s \tau^x, \quad u_{\hat{y}} = \chi_s \tau^z + \Delta_s \tau^x, \quad (48a)$$

$$u_{\hat{x}+\hat{y}} = \chi_d \tau^z, \quad u_{-\hat{x}+\hat{y}} = -\chi_d \tau^z, \quad a_\gamma(u) = 0. \quad (48b)$$

This corresponds to the Z2Azz13 Ansatz in the PSG classification by Wen [55]. Thus, the \mathbb{Z}_2 Ansatz Z3000 on the Shastry-Sutherland lattice can be continuously connected to the \mathbb{Z}_2 Ansatz Z2Azz13 on the square lattice. This connection is protected by the projective realization of G_x and σ_{xy} . When considering up to NNN amplitudes, among the \mathbb{Z}_2 Ansätze listed in this work, five more can be realized with IGG \mathbb{Z}_2 , which are labeled Z2A0013, Z2B0013, Z2Axx0z, Z2Ax2(12)n, and Z2Bx2(12)n. Their connections to the square lattice can be established following a procedure similar to that carried out above for the Z2Azz13 Ansatz, as summarized in Table V.

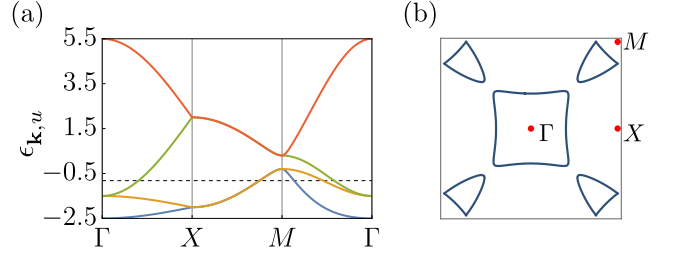


FIG. 5. (a) Dispersion of the parent U100 state and (b) illustration of its Fermi surfaces. The parameters here are chosen to be $\chi_s = 1.0$, $\chi_d = 0.5$, $\chi_{d'} = 0.4$, and $\chi_\square = 0.3$. The dashed line in the band structure marks the Fermi level.

IV. NUMERICAL RESULTS

A. \mathbb{Z}_2 Dirac state: Mean-field properties

Given that the gapless Z3000 state serves as the most promising candidate to describe the QSL in the generalized SSM (as we will show below), we now describe its corresponding variational wavefunction in terms of Abrikosov pseudo-fermions [86]. First, we define a mean-field state in the fermionic Hilbert space by taking the ground state $|\phi_{\text{MF}}\rangle$ of the following noninteracting spinon Hamiltonian, which is of the generalized Bardeen-Cooper-Schrieffer form:

$$\begin{aligned} \hat{H}_{\text{MF}}^{\text{Z3000}} = & \chi_d \sum_{\langle ij \rangle_{\text{teal}}, \alpha} s_{ij}^d \hat{f}_{i,\alpha}^\dagger \hat{f}_{j,\alpha} + \chi_{d'} \sum_{\langle ij \rangle_{\text{orange}}, \alpha} s_{ij}^{d'} \hat{f}_{i,\alpha}^\dagger \hat{f}_{j,\alpha} \\ & + \sum_{\langle ij \rangle_{\text{blue}}} \left[\chi_s \sum_{\alpha} s_{ij}^s \hat{f}_{i,\alpha}^\dagger \hat{f}_{j,\alpha} + \Delta_s \nu_{ij}^s (\hat{f}_{i,\uparrow}^\dagger \hat{f}_{j,\downarrow} + \text{h.c.}) \right] \\ & + \sum_{\langle ij \rangle_{\text{green}}} \left[\chi_\square \sum_{\alpha} s_{ij}^\square \hat{f}_{i,\alpha}^\dagger \hat{f}_{j,\alpha} + \Delta_\square \nu_{ij}^\square (\hat{f}_{i,\uparrow}^\dagger \hat{f}_{j,\downarrow} + \text{h.c.}) \right] \\ & + \mu \sum_{i,\alpha} \hat{f}_{i,\alpha}^\dagger \hat{f}_{i,\alpha}. \end{aligned} \quad (49)$$

Here, s_{ij} and ν_{ij} are sign factors for hoppings and pairings, respectively, which take values $+1(-1)$ for bonds marked as solid (dashed) in Figs. 4(b) and (c). The different colors in Fig. 4(b) label the symmetry-inequivalent bonds, as referenced in Eq. (49). We fix $\chi_s = 1$ as the overall energy scale, and the resulting wavefunction is thus parametrized by six variational parameters: χ_d , $\chi_{d'}$, χ_\square , Δ_s , Δ_\square , and the onsite chemical potential, μ .

Although the Z3000 Ansatz can be obtained by lowering the U(1) IGG—via singlet pairing terms—of three distinct U(1) states, namely, U100, U300, and U800 in Table III, it is most straightforward to view it as a descendant of the parent U100 state (see also App. G). Indeed, due to the linear (nonprojective) realization of symmetries in the U100 state, it allows for uniform real hopping amplitudes on *all* diagonal and square-lattice bonds. It can thus be retrieved from the Z3000 Ansatz (49) by setting the pairings $\Delta_s = \Delta_\square = 0$. The band structure

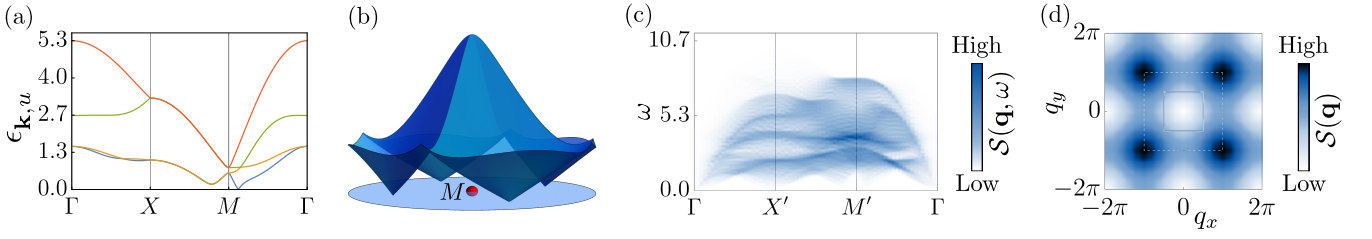


FIG. 6. (a) Spinon band structure of the Z3000 state for the variationally optimized parameters at $J_s/J_d = 0.80$, given by $\chi_s = 1.0$, $\chi_d = 0.46$, $\chi_{d'} = -0.09$, $\chi_\square = 0.14$, $\Delta_s = 0.39$, $\Delta_\square = 0.38$, and $\mu = 0.35$. (b) Spinon dispersion of the optimized Z3000 state, showing the four Dirac cones residing at $M(\pi/2, \pi/2) + (\pm\varepsilon, \pm\varepsilon)$. (c) Dynamical spin structure factor, and (d) equal-time spin structure factor of this state. The solid and dashed squares denote the first Brillouin zone (FBZ) and the extended Brillouin zone (EBZ), respectively.

of the parent U100 state is shown in Fig. 5(a) and at half filling, it features a Fermi surface [Fig. 5(b)]. On adding a nonzero Δ_s , the nearly square-shaped Fermi surface surrounding the Γ point is completely lifted, and the other Fermi surfaces in the vicinity of the M points shrink to isolated points, forming Dirac cones at $M(\pi/2, \pi/2) + (\pm\varepsilon, \pm\varepsilon)$. The magnitude of ε is found to decrease with increasing Δ_s and Δ_\square . In Fig. 6(a), we plot the dispersion of the Z3000 state for the VMC-optimized parameters at $J_s/J_d = 0.8$ while the four Dirac cones surrounding the M point are shown in Fig. 6(b). We also present the spin correlations of this mean-field state, as reflected in its dynamical and equal-time spin structure factors, in Figs. 6(c) and (d), respectively.

After performing a particle-hole transformation on the spinons with flavor \downarrow ,

$$\hat{f}_{i,\downarrow}^\dagger \rightarrow \hat{f}_{i,\downarrow}, \quad \hat{f}_{i,\uparrow}^\dagger \rightarrow \hat{f}_{i,\uparrow}^\dagger, \quad (50)$$

the mean-field Hamiltonian (49) commutes with the total number of particles. Thus, $|\phi_{\text{MF}}\rangle$ is defined by filling suitable single-particle orbitals. In this process, the choice of boundary conditions should be such that they lead to a unique state (by filling *all* orbitals in a shell with the same mean-field energy). Periodic (P) and antiperiodic (A) boundary conditions along the \mathbf{a}_1 and \mathbf{a}_2 lattice-vector directions [see Fig. 1(a)] can be considered, leading to four choices: [P,P], [P,A], [A,P], and [A,A]. Here, we impose antiperiodic and periodic boundary conditions along the \mathbf{a}_1 and \mathbf{a}_2 directions, respectively, i.e., [A,P], which leads to a closed shell (unique state) on $L \times L$ clusters with dimensions $L = 4\ell$ and $L = 4\ell + 2$, where ℓ is a positive integer.

B. Gutzwiller-projected Ansatz

A legitimate QSL wavefunction, residing in the correct sector with one fermion per site (corresponding to the physical Hilbert space of the spin-1/2 model), is then obtained by applying the Gutzwiller projector to the mean-field state $|\phi_{\text{MF}}\rangle$:

$$|\Psi_{\text{QSL}}\rangle = \mathcal{P}_{\text{G}}|\phi_{\text{MF}}\rangle, \quad (51)$$

where $\mathcal{P}_{\text{G}} = \prod_i (\hat{n}_{i,\uparrow} - \hat{n}_{i,\downarrow})^2$, $\hat{n}_{i,\alpha} = \hat{f}_{i,\alpha}^\dagger \hat{f}_{i,\alpha}$ being the fermionic density of flavor α on site i . The variational energy and correlation functions for $|\Psi_{\text{QSL}}\rangle$ can be computed in a straightforward fashion using Monte Carlo sampling, by virtue of which the constraint is imposed exactly [92]. Furthermore, a stochastic reconfiguration (SR) optimization enables us to obtain accurate estimates of the variational parameters contained in Eq. (49) with small statistical uncertainties [93, 94], even when a large number of parameters are involved [95–99].

A standard technique to systematically improve the accuracy of variational wavefunctions and approach the true ground state involves the application of a few Lanczos steps on a given variational state $|\Psi_{\text{QSL}}\rangle$ [100, 101]:

$$|\Psi_{p\text{-LS}}\rangle = \left(1 + \sum_{k=1}^p \lambda_k \hat{\mathcal{H}}^k \right) |\Psi_{\text{QSL}}\rangle, \quad (52)$$

where the λ_k s are variational parameters. For large enough p , $|\Psi_{p\text{-LS}}\rangle$ is guaranteed to converge to the exact ground state $|\Psi_{\text{ex}}\rangle$ provided the initial trial state $|\Psi_{\text{QSL}}\rangle$ is not orthogonal to $|\Psi_{\text{ex}}\rangle$, i.e., for $\langle \Psi_{\text{ex}} | \Psi_{\text{QSL}} \rangle \neq 0$. However, on large clusters, only a few Lanczos steps can be efficiently executed, and here, we consider the case with $p = 1$ and $p = 2$ ($p = 0$ corresponds to the initial trial wavefunction $|\Psi_{\text{QSL}}\rangle$). Based on this sequence, an estimate of the exact ground-state energy can be obtained by the method of zero-variance extrapolation. In fact, for sufficiently accurate states, $E - E_{\text{ex}} \approx \text{constant} \times \sigma^2$, where $E = \langle \hat{\mathcal{H}} \rangle / N$ and $\sigma^2 = (\langle \hat{\mathcal{H}}^2 \rangle - \langle \hat{\mathcal{H}} \rangle^2) / N$ are the energy and variance per site, respectively. Thus, the exact ground-state energy E_{ex} can be extracted by fitting E vs σ^2 for $p = 0, 1$, and 2. The energy, its variance, and the correlation functions after the application of a few Lanczos steps are calculated using the standard variational Monte Carlo method.

C. Variational Monte Carlo

Our variational calculations are performed on $L \times L$ tori, which respect all symmetries of the $p4g$ wallpaper

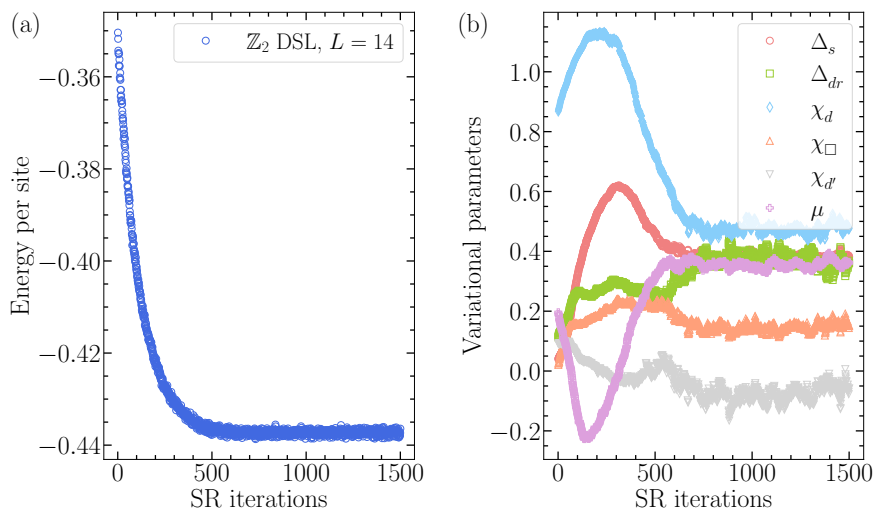


FIG. 7. A typical variational Monte Carlo optimization run for the Z_{3000} state on a 14×14 site cluster for $J_s/J_d = 0.80$. (a) Energy per site in units of J_d , and (b) variational parameters Δ_s , Δ_{\square} , χ_d , χ_{\square} , $\chi_{d'}$, and μ , as a function of the number of stochastic reconfiguration (SR) iterations. In (b), the initial parameters are taken to be $\Delta_s = 0.04$, $\Delta_{\square} = 0.11$, $\chi_d = 0.87$, $\chi_{\square} = 0.02$, $\chi_{d'} = 0.09$, $\mu = 0.2$, and we set $\chi_s = 1$ as the reference. The optimized parameter values presented in Table VI are obtained by averaging over a much larger number of converged SR iterations than shown here. In comparison, the energy per site of the optimized parent $U(1)$ state [U100], i.e., with $\Delta_s = \Delta_{\square} = 0$ is $E/J_d = -0.37500(1)$.

group, with periodic boundary conditions imposed on the spin Hamiltonian (1). We focus our analysis on the coupling ratio $J_s/J_d = 0.80$ which is located in the middle of the QSL regime seen in Refs. [32, 43, 44, 46], and for which the energy and correlation functions have been reported with different numerical approaches, thereby facilitating detailed comparisons.

1. Energetics

Among the *Ansätze* listed in Table V which can be continuously connected to the states on the square lattice, we find that the VMC optimization of the projected Z_{3000} *Ansatz* consistently yields the lowest variational energy on all clusters, with sizes ranging from $L = 6$ to 40, while the other *Ansätze* have substantially higher energies. For the optimized Z_{3000} state, crucially, we observe that the singlet pairing amplitudes Δ_s and Δ_{\square} optimize to appreciable values for all cluster sizes, and, in fact, increase in magnitude with increasing system size (see Table VI), providing evidence for a \mathbb{Z}_2 gauge structure in the thermodynamic limit. Furthermore, these pairings lead to a substantial energy gain $(E_{\mathbb{Z}_2} - E_{U(1)})/E_{U(1)} \sim 0.16$ on top of the parent $U(1)$ state, which, more importantly,

L	Δ_s	Δ_{\square}	χ_d	$\chi_{d'}$	χ_{\square}	μ
6	0.256(1)	0.085(1)	0.376(1)	0.123(1)	0.181(1)	0.931(1)
8	0.355(1)	0.261(1)	0.386(1)	-0.034(2)	0.126(1)	0.605(1)
10	0.371(1)	0.320(1)	0.423(1)	-0.062(1)	0.131(1)	0.475(1)
12	0.381(2)	0.353(2)	0.446(1)	-0.076(2)	0.136(2)	0.399(2)
14	0.387(3)	0.381(2)	0.462(2)	-0.088(2)	0.139(2)	0.345(2)

TABLE VI. The singlet pairing and hopping amplitudes of the \mathbb{Z}_2 Dirac QSL (Z_{3000} state) on different cluster sizes obtained after VMC optimization for $J_s/J_d = 0.80$. The hopping on the square bonds χ_s is set to one.

remains robust with increasing system size (as checked for up to $L=40$). In contrast, for the J_1 - J_2 square-lattice Heisenberg antiferromagnet, the energy gain of the Z_{2Azz13} state (due to d_{xy} singlet pairing terms on fifth-neighbor bonds³) is $\sim 1\%$ on top of the parent $U(1)$ state [48]. In Fig. 7, we present a typical VMC optimization run showing the evolution of the energy and the parameters of the Z_{3000} state starting from a generic unbiased starting point. We verify the convergence by initiating many optimization runs with different random initial values, and found that the energy and variational parameters converge neatly to the same value (within error bars) after averaging over a sufficient number of Monte Carlo steps. It is important to note that while the energy converges after ~ 500 iterations, the parameters converge to their final values only after a much larger number of SR iterations (see Fig. 7). This is because in optimizing the former, the steepest-descent forces are calculated using correlated sampling instead of via energy differences [93, 102].

Having established that the Z_{3000} *Ansatz* represents

L	0-LS	1-LS	2-LS	Extrapolation
6	-0.439512(1)	-0.448633(1)	-0.450432(1)	-0.451391(7)
8	-0.437955(1)	-0.446537(1)	-0.448619(1)	-0.449735(23)
10	-0.4375346(6)	-0.4454888(6)	-0.447838(3)	-0.449046(33)
12	-0.4373669(5)	-0.444746(1)	-0.447279(4)	-0.44929(21)
14	-0.4372820(6)	-0.444144(1)	-0.446776(4)	-0.44972(11)

TABLE VII. The energies of the \mathbb{Z}_2 Dirac QSL (Z_{3000} state) with $p = 0, 1$, and 2 Lanczos steps, and the zero-variance extrapolation estimate on different cluster sizes as obtained by VMC, for $J_s/J_d = 0.80$.

³ On the Shastry-Sutherland lattice, a nonzero singlet pairing amplitude on fifth-neighboring bonds—connecting $(0,0)$ to sites $(\pm 2, \pm 2)$ —does not give any detectable energy gain.

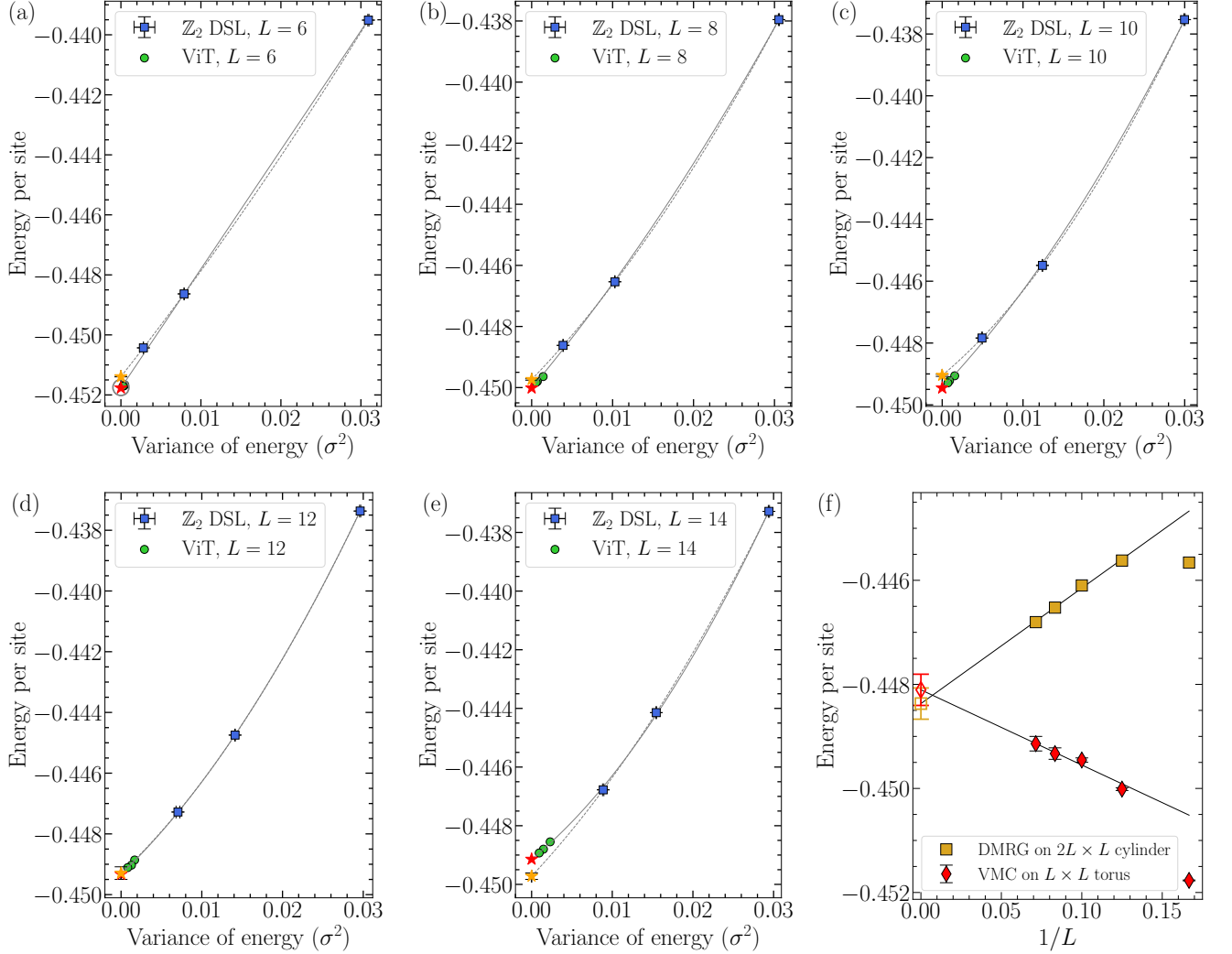


FIG. 8. Variational energies for the \mathbb{Z}_2 Dirac QSL (Z3000 state) at $J_s/J_d = 0.80$, as a function of the variance of energy, for zero, one, and two Lanczos steps. (a)–(e) An accurate estimate of the ground-state energy on the $L = 6, 8, 10, 12$, and 14 clusters is obtained by extrapolating the three variational results from VMC (blue squares) together with the ViT data (green circles) at smaller variance [46] to the zero-variance limit (red star) by a quadratic fit (solid curve). The estimate obtained by employing a quadratic fit (dashed curve) to only the three VMC points (blue squares) leads to less reliable values of the ground-state energy (yellow star), especially for larger system sizes, as seen by the nonmonotonic behavior thereof with respect to system size (see Fig. 9 and Table VII, and the main text for a description of the extrapolation method). For $L = 6$, the ED energy is marked by an empty circle. (f) The thermodynamic estimate of the ground-state energy, as obtained by a finite-size scaling of the estimated energies from VMC + ViT on the $L = 8, 10, 12$ and 14 clusters using a $1/L$ scaling form and a linear fit. The yellow squares provide a comparison with the DMRG estimates from Ref. 43.

the lowest-energy variational wavefunction (within the class of Gutzwiller-projected fermionic states) for all the system sizes investigated—and that the singlet pairing amplitudes characterizing it as well as the resulting energy gains remain size-consistent—we consider it as our starting ($p = 0$) state and improve thereupon by applying Lanczos steps. At $J_s/J_d = 0.80$, the effect of two Lanczos steps for different cluster sizes is shown in Fig. 8 (see also Table VII for the actual values of the energies of the Z3000 state). To refine the accuracy of the extrapolation, we also include the smaller-variance ViT data from Ref. 46. A zero-variance extrapolation is then per-

formed via a quadratic fit of the six points (three VMC and three ViT), $E = E_{\text{ex}} + \mathcal{A} \times \sigma^2 + \mathcal{B} \times (\sigma^2)^2$. The inclusion of the ViT data in the fit proves crucial in curing the apparent nonmonotonic behavior with system size in the zero-variance-extrapolated estimates of the ground-state energies (compare “ \mathbb{Z}_2 DSL extr.” vs. “ \mathbb{Z}_2 DSL + ViT extr.” in Fig. 9, and see Table VIII for the corresponding energies), thus enabling a reliable estimation in the thermodynamic limit. For our present purposes, the computationally demanding $p = 2$ calculations have been performed only for the $L = 6, 8, 10, 12$, and 14 clusters. It is worth emphasizing that this zero-variance extrap-

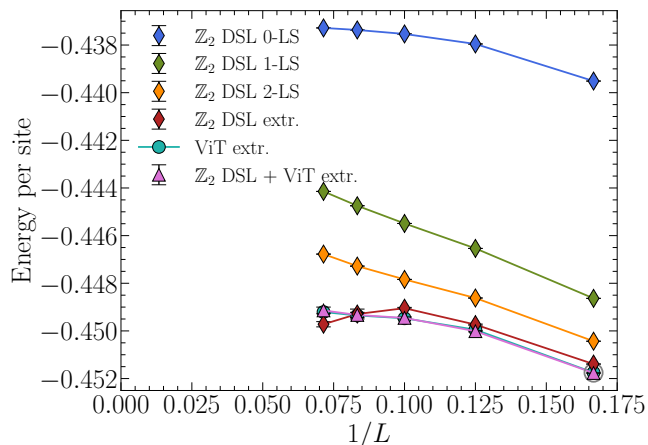


FIG. 9. The dependence on system size of the energies of the \mathbb{Z}_2 Dirac spin liquid (DSL), with $J_s/J_d = 0.8$, for $p = 0, 1, 2$ Lanczos steps and zero-variance extrapolated estimates using (i) only VMC data (\mathbb{Z}_2 DSL extr.), and (ii) combining VMC with lower-variance ViT data (\mathbb{Z}_2 DSL + ViT extr.) [46]. The latter is also consistent with ViT-only extrapolation estimates [46]. Also marked (gray circle) is the ED energy on a 36-site cluster.

olation procedure yields size-consistent estimates of the energy per site for not only the ground state [103, 104] but also excited states [105]. In fact, it is well known that the Lanczos procedure (for a fixed p) becomes progressively inefficient upon increasing the system size, yet, the extrapolation remains accurate [101]. This can be observed from the gain in the energy and the variance with respect to $p = 0$, which decreases with L (see Fig. 8 and Table VII), but the extrapolation is unaffected since the slope is essentially unchanged [48, 104]. Indeed, our estimate of the ground-state energy on the 6×6 cluster is in excellent agreement with the exact result, and equal

L	VMC	ViT	VMC + ViT	DMRG
6	-0.451391(7)	-0.451750	-0.451768(8)	-0.44565886
8	-0.449735(23)	-0.44995	-0.450013(27)	-0.44562053
10	-0.449046(33)	-0.449470	-0.449454(41)	-0.44609839
12	-0.44929(10)	-0.449352	-0.44933(11)	-0.44652433
14	-0.44972(11)	-0.449207	-0.44914(14)	-0.44680369
∞ *		-0.4486(2)	-0.4481(3)	-0.44837(30)

TABLE VIII. The ground-state energies of the spin-1/2 Heisenberg model at $J_s/J_d = 0.80$ for different cluster sizes, as obtained from zero-variance extrapolation. The extrapolation is performed using data on $L \times L$ tori from VMC, neural-network quantum states (ViT) [46], and combined extrapolation with both VMC and ViT energies (VMC + ViT); or from DMRG [43] on $2L \times L$ cylinders with periodic boundary conditions along the shorter direction. Our most accurate estimate of the ground-state energy on any given cluster is obtained from VMC + ViT extrapolation and is marked in bold. The exact-diagonalization (ED) value for $L = 6$ is -0.4517531 [46].

(within error bars) to the corresponding estimate from ViT [46] (see Fig. 8(a) and Table VIII). Similarly, on the 8×8 and larger clusters, the estimate of the ground-state energy from VMC is equal (within error bars) to the ViT estimate (see Figs. 8(b)–(e) and Table VIII). By using the ground-state energy estimates on different cluster sizes ($L = 8, 10, 12, 14$), we can also perform a finite-size extrapolation; see Fig. 8(f). At $J_s/J_d = 0.80$, our estimate for the energy per site of the infinite two-dimensional system is

$$E_\infty^{2D}/J_d = -0.4481(3). \quad (53)$$

This is equal (within error bars) to the ViT [46] and DMRG [44] estimates (see Fig. 8(f) and Table VIII), and we obtain this competitive value by optimizing *only* eight parameters [six from Eq. (49) and two from the Lanczos procedure in Eq. (52)], as opposed to the very large number of parameters that need to be optimized in the ViT [46] and DMRG [44] approaches. Note, moreover, that our energies are obtained for a state that has all the symmetries of the lattice by construction, while the DMRG states are computed on cylinders with open boundaries.

In summary, our energetic analysis lends support to the scenario of a \mathbb{Z}_2 Dirac state providing a good variational description of the gapless QSL reported in earlier studies [44, 46]. In the next section, based on an analysis of the correlation functions, we bolster the case for a \mathbb{Z}_2 QSL ground state and argue that it is the same phase as the QSL in the J_1 - J_2 square-lattice Heisenberg antiferromagnet [48].

2. Correlations

We begin by comparing the real-space, isotropic, equal-time, spin-spin correlations of the \mathbb{Z}_2 Dirac state (supplemented with 2 LS) with those obtained from the unbiased neural-network ViT wavefunction, which has recently been diagnosed to feature gapless excitations [46]. In Fig. 10(a), for the $L = 14$ cluster, we notice that the Z3000 state correctly reproduces the sign of *all* ViT correlators with their magnitudes also being in excellent agreement. A similar level of concurrence between VMC, ViT and ED correlators is also observed on the 6×6 cluster [see Fig. 10(b)]. In Fourier space, the equal-time spin structure factor of the projected \mathbb{Z}_2 Dirac state (supplemented with 2 LS) obtained from VMC displays soft maxima at (π, π) [see Fig. 10(c)] with its value on the $L = 14$ cluster being $\mathcal{S}(\pi, \pi) \approx 9.32$; this is to be compared with $\mathcal{S}(\pi, \pi) \approx 9.89$ obtained from ViT on the same cluster⁴. These results, showcasing impressive

⁴ The VMC result is for two Lanczos steps while the ViT result is extrapolated with the number of layers.

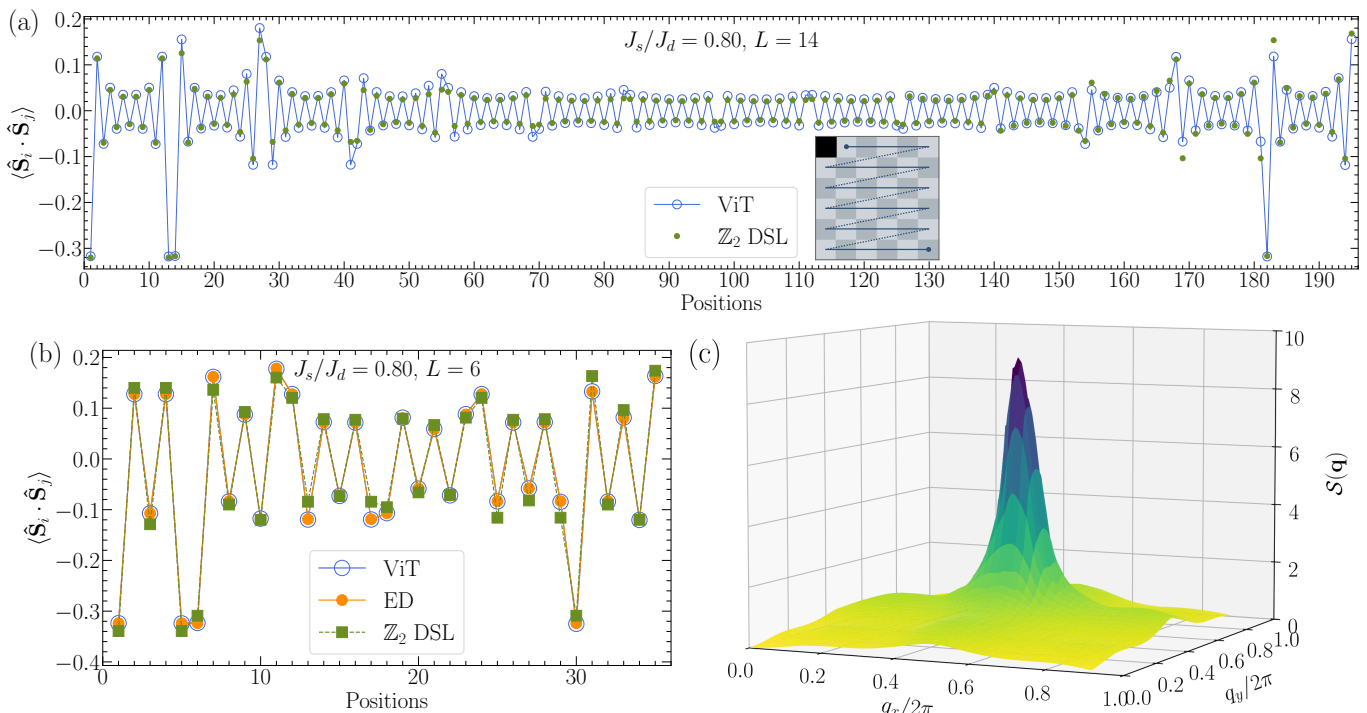


FIG. 10. (a) The equal-time isotropic spin-spin correlations ($\hat{S}_i \cdot \hat{S}_j$) in real space for the projected \mathbb{Z}_2 DSL (Z3000 state) supplemented with 2 LS, as computed using VMC (full green dots) and compared with the ViT wavefunction (empty blue circles) from Ref. 46 on a 14×14 lattice at $J_s/J_d = 0.80$. The error bars in VMC are $\sim \mathcal{O}(10^{-4})$. Inset: the blue line schematically illustrates the path on the $L = 14$ and $L = 6$ clusters along which the spin-spin correlations (with respect to the site marked in black) are ordered in the panel. Note that the ViT wavefunction explicitly breaks $SU(2)$ spin-rotation symmetry and the quantity plotted is $\langle \hat{S}^x \hat{S}^x + \hat{S}^y \hat{S}^y + \hat{S}^z \hat{S}^z \rangle$; our wavefunction is manifestly $SU(2)$ symmetric, and we thus plot $3 \times \langle \hat{S}^z \hat{S}^z \rangle$. (b) The same on an $L = 6$ cluster, now including a comparison with ED (orange circles). (c) The equal-time spin structure factor for the \mathbb{Z}_2 DSL (supplemented by 2 LS) obtained with VMC on a 14×14 lattice.

agreement, provide compelling evidence that the gapless spin liquid found in Refs. [43, 46] is a \mathbb{Z}_2 QSL described by the Z3000 state.

In Fig. 11, we show the decay of real-space spin-spin correlations $|\langle \hat{S}_i \cdot \hat{S}_j \rangle|$ for the $(1, 0)$ direction on a 14×14 cluster at $J_s/J_d = 0.80$. Given the gapless nature of the phase, one expects that $|\langle \hat{S}_i \cdot \hat{S}_j \rangle| \propto |\mathbf{r}|^{-(z+\eta)}$, manifesting the critical behavior due to gapless triplet excitations. Indeed, we find such a power-law decay indicating the critical nature of Néel antiferromagnetic correlations in the QSL phase, in accord with the findings from DMRG and ViT [43, 46]. Furthermore, we determine a critical exponent of $z + \eta = 1.5$ in consistency with that reported for the square lattice J_1 - J_2 Heisenberg antiferromagnet in Ref. 51, but differing from the DMRG and ViT estimates of ~ 1.3 [44, 46]. Hence, the QSL region in the Shastry-Sutherland and square-lattice Heisenberg antiferromagnets and the island of liquidity connecting these two models are likely the same phase, i.e., a \mathbb{Z}_2 Dirac QSL. Furthermore, this suggests a mechanism common to both lattices whereby Néel order melts due to frustration to give way to a gapless spin liquid [48].

Going beyond such equal-time correlations, next, we discuss the *dynamical* spin structure factors obtained us-

ing the Keldysh pseudo-fermion functional renormalization group (pf-FRG).

D. Keldysh pf-FRG

To compare the proposed *Ansätze* with numerical results, we employ a novel methodological approach: the pseudo-fermion functional renormalization group (pf-FRG) within the Keldysh formalism. This allows for direct computation of the dynamical spin structure factor for the Heisenberg model⁵. The pf-FRG is already a well-established method for investigating the ground-state properties of Heisenberg systems, especially for frustrated and higher-dimensional lattices, where conventional techniques such as DMRG, quantum Monte Carlo (QMC), and VMC face difficulties, e.g., the sign problem or challenges due to dimensionality [107].

⁵ Some early attempts have been made at obtaining $S(\mathbf{q}, \omega)$ within the dimer phase of the SSM based on variants of perturbative approaches [106].

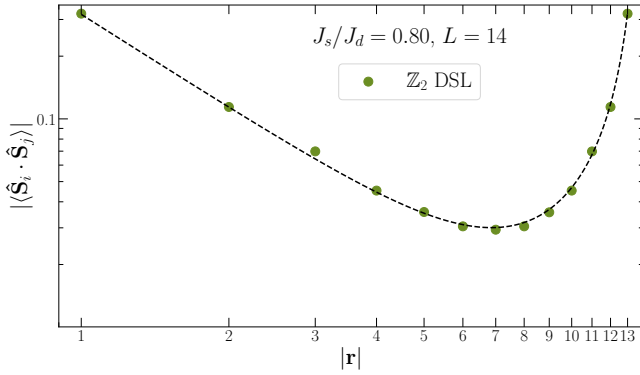


FIG. 11. The magnitude of (equal-time) isotropic real-space spin-spin correlations for the \mathbb{Z}_2 DSL (supplemented with 2 LS), plotted on a log-log scale for the $\mathbf{a}_1 = (1, 0)$ direction on a 14×14 lattice for $J_s/J_d = 0.80$. To account for the periodic boundary conditions (which leads to the eventual upturn), the fit is to a power law [50, 51] $|\langle \hat{\mathbf{S}}_i \cdot \hat{\mathbf{S}}_j \rangle| \propto |\mathbf{r}|^{-z-\eta} + \sum_{\mathbf{R} \neq (0,0)} [(|\mathbf{r} - L\mathbf{R}|^{-z-\eta}) - (|L\mathbf{R}|^{-z-\eta})]$ with $z + \eta = 1.5$, where $\mathbf{R} \equiv (R_x, R_y)$; here, $\mathbf{R} = R\mathbf{a}_1$ for $R = 1, \dots, L$. The error bars on $\langle \hat{\mathbf{S}}_i \cdot \hat{\mathbf{S}}_j \rangle$ are $\sim 10^{-4}$.

The use of the Keldysh formalism makes it possible to calculate dynamical properties directly on the real-frequency axis, avoiding the need for analytical continuation associated with Matsubara frequencies (which is known to be flawed due to numerical inaccuracies and is thus unreliable [108]). The drawback of the Keldysh pf-FRG is that we have to resort to a finite temperature for the calculations, which, in this case, is given by $T/J_d = 0.1$. This is because the FRG flow shows nonmonotonic features below this temperature scale—possibly due to the numerical integration schemes involved—which then induce artifacts in the structure factor. The Keldysh formalism also increases the computational cost, restricting our analysis to a 9×9 lattice. Furthermore, the starting point for the FRG is a quantum paramagnetic state, which, together with the finite temperature, suppresses effects around $(0, 0)$ that other techniques might predict more reliably. Thus, we cannot exclude a spectral branch emanating from the $\Gamma(0, 0)$ point at small frequencies, as obtained at the mean-field level [see Fig. 6(c)]. All details concerning the Keldysh pf-FRG will be discussed in a forthcoming publication [109].

In practice, we use the Keldysh pf-FRG to calculate the retarded dynamical spin susceptibility $\chi^{\text{ret}}(\mathbf{q}, \omega)$, which can be related to the spin structure factor by

$$\mathcal{S}^{\text{ret}}(\mathbf{q}, \omega) = \frac{1}{\pi} (1 - e^{-\beta\omega})^{-1} \text{Im}(\chi^{\text{ret}}(\mathbf{q}, \omega)). \quad (54)$$

Naturally, we exclude small frequencies for which numerical artifacts would be artificially enhanced. Our results for the dynamical spin structure factor are presented in Fig. 12(a). Due to the finite temperature, we see very broadened branches but still, two distinct lobes of maximal intensity around (π, π) [at $(\pi \pm 0.4, \pi \pm 0.4)$] are

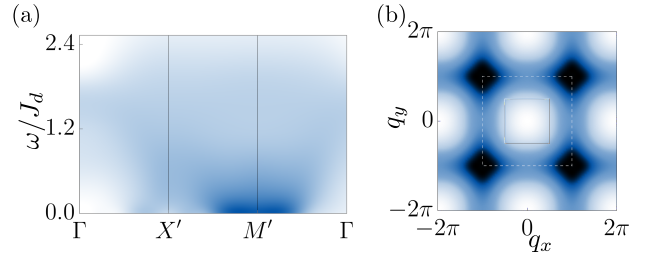


FIG. 12. (a) Dynamical and (b) equal-time spin structure factors obtained from Keldysh pf-FRG for $J_s/J_d = 0.80$ at $T/J_d = 0.1$ on a 9×9 lattice. The conventions for the color maps are adopted from those used in Figs. 6(c) and (d), respectively.

discernible, while the (π, π) point itself also features appreciable intensity. This matches the expectation for the scenario of a \mathbb{Z}_2 Dirac QSL with nodal points at $M(\pi/2, \pi/2) + (\pm\varepsilon, \pm\varepsilon)$ [see Fig. 6(b)]. Indeed, scattering from thus-situated Dirac cones would result in the principal intensity at low energy being observed at $(\pi, \pi) \pm (2\varepsilon, 2\varepsilon)$ with relatively lesser intensity at (π, π) due to the presence of a larger number of scattering channels (wavevectors connecting different Dirac cones) for the former. Furthermore, we see a gradual decrease in intensity with increasing ω and a broad continuum consistent with deconfined fractionalized excitations, as expected for a \mathbb{Z}_2 QSL.

Interestingly, the corresponding classical ($S \rightarrow \infty$) model hosts an incommensurate spiral ground state for $J_s/J_d < 1$ [1, 110, 111], so one may possibly ascribe the origin of the incommensurate location of the double maxima to the underlying spiral correlations. However, we rule out such a scenario, since if it were the case, the equal-time spin structure factor would show peaks (soft maxima in our case) at the incommensurate wave vectors (π, Θ) or (Θ, π) [25] with $\Theta = \pi \pm \arccos(J_s/J_d)$ (in the limit $S \rightarrow \infty$). In contrast, the maxima observed in $\mathcal{S}(\mathbf{q}, \omega)$ is along a different axis $(\pi \pm \varepsilon, \pi \pm \varepsilon)$, and our equal-time $\mathcal{S}(\mathbf{q})$ hosts maxima at (π, π) . Besides, such a spiral phase was also shown to have a higher energy within the coupled-cluster approach [19].

Given the fact that the Keldysh pf-FRG results have been obtained without any assumptions on the wavefunction or symmetry constraints and, in this sense, represent unbiased results from a correlator-based approach, they further corroborate the picture of a \mathbb{Z}_2 Dirac QSL ground state.

Unlike its dynamical counterpart, the equal-time spin structure factor provided by Keldysh pf-FRG instead shows broad diffuse maxima centered around (π, π) . This is due to the similar cumulative spectral weights obtained at and around (π, π) when $\mathcal{S}(\mathbf{q}, \omega)$ is integrated over ω , which washes out the underlying distribution of intensities at small ω . Moreover, this is consistent with the $\mathcal{S}(\mathbf{q})$ computed using VMC, which also shows a single broadened maxima at (π, π) [see Fig. 10(c)]. It is inter-

esting to note that the equal-time $\mathcal{S}(\mathbf{q})$ obtained from both VMC [Fig. 10(c)] and Keldysh pf-FRG [Fig. 12(b)] do not qualitatively differ from the mean-field profile [see Fig. 6(d)]. This is likely due to the fact that the \mathbb{Z}_2 gauge field is gapped, mediating only short-range interactions between spinons, and it does not significantly alter the mean-field expectation [56]. In contrast, for gapless states with a U(1) IGG, gauge fluctuations can lead to drastic differences between the mean-field and projected $\mathcal{S}(\mathbf{q})$ (cf. Ref. 112 for the kagome U(1) Dirac QSL).

V. CONCLUSIONS AND OUTLOOK

Our work presents an atlas of QSLs on the Shastry-Sutherland lattice along with their spectroscopic signatures. This is accomplished using the framework of projective symmetry groups, which, for fermionic spinons, yields 46 U(1) and 80 \mathbb{Z}_2 QSL states. Using this information, we investigate the QSL regime of the generalized spin-1/2 Shastry-Sutherland Heisenberg antiferromagnet and its interpolation to the square-lattice limit. We identify the subset of PSGs which can be continuously connected to the ones on the square lattice. In particular, we pinpoint the counterpart of the \mathbb{Z}_2 Dirac QSL on the square lattice (more precisely, the d -wave pairing Z2Azz13 state in Ref. 55), which is a prime candidate for the QSL ground state of the $S = 1/2$ J_1 - J_2 square-lattice Heisenberg antiferromagnet. Our equivalent \mathbb{Z}_2 Dirac QSL (called Z3000 state in this work) upon Gutzwiller projection and optimization over only a few parameters—using variational Monte Carlo—produces energies which are equal, within error bars, to those obtained from ViT, for all cluster sizes [46], and from DMRG [43], in the thermodynamic limit. Similarly, the equal-time correlators computed with VMC for this \mathbb{Z}_2 Dirac QSL show remarkable qualitative and *quantitative* agreement across system sizes with those found from unconstrained ViT wavefunctions. The long-distance decay of the real-space spin-spin correlators follows a power law with critical exponents $z + \eta = 1.5$, which is in agreement with that obtained for the square-lattice QSL [51], thus providing compelling evidence that the Shastry-Sutherland and square-lattice QSLs belong to the same phase. We also apply the newly developed Keldysh pseudo-fermion functional renormalization group to evaluate the dynamical spin structure factor, which shows a double-lobe maxima around (π, π) and subdominant intensity at (π, π) , as would be expected from scattering by Dirac cones at $(\pi/2, \pi/2) + (\pm\varepsilon, \pm\varepsilon)$. This observation adds to the evidence for a \mathbb{Z}_2 Dirac QSL from an independent correlator-based approach, which is blind to specific *Ansätze* and is not dictated by symmetry constraints. Further, given the rapid experimental and theoretical developments in exploring putative QSL behavior on the Shastry-Sutherland lattice, these predictions for the dynamical structure factors set the stage for identifying such exotic states in

materials and models from spectroscopic signatures.

Our classification of lattice-nematic QSLs compatible with the symmetry of the proximate plaquette VBC order, i.e., preserving C_4 but breaking glide and mirror symmetries (see Appendix F), opens the door to studying the phase transitions of fully symmetric QSLs to their nematic counterparts. Notably, a different class of gapped lattice-nematic \mathbb{Z}_2 QSLs, which instead break 90° rotational symmetry, have previously been identified within the Schwinger-boson formalism [25]. Such a nematic state has also been studied with Abrikosov fermions but for the square lattice [113]; it would be interesting to extend this classification to the Shastry-Sutherland lattice in future work to investigate the transition from the \mathbb{Z}_2 Dirac QSL to the Néel phase. A field-theoretic formulation of this transition, akin to that developed for the J_1 - J_2 model on the square lattice [114], promises to provide further important insights.

Given the rather narrow region of stability for the Shastry-Sutherland QSL along the Heisenberg axis, it would also be interesting to identify directions in Hamiltonian parameter space which possibly widen this regime. To this end, there is evidence from DMRG [7] that the introduction of an XY-type anisotropy enlarges the window of stability of the QSL, and it is worth examining whether the same \mathbb{Z}_2 Dirac QSL as the one on the Heisenberg axis remains stable upon the introduction of XXZ anisotropy or whether a new QSL phase occupies this region. Moreover, the inclusion of an explicit scalar spin-chirality term in the Hamiltonian has recently been shown to induce a chiral spin liquid (CSL) of the Kalmeyer-Laughlin type [115]. Since there exist myriad distinct Kalmeyer-Laughlin CSLs—differing in their anyon content—within parton constructions, in order to uncover the microscopic nature of the CSL, it would be necessary to obtain the chiral representation classes for the algebraic PSGs [68] of the Shastry-Sutherland lattice. Assessing the energetics and correlation functions of the corresponding Gutzwiller-projected chiral *Ansätze* would then help pin down the precise CSL that provides the best variational description of the ground state. Closely tied to this is the issue of identifying, within this classification scheme, the CSLs which serve as natural candidates for continuous transitions out of our \mathbb{Z}_2 Dirac QSL. These could include the rare class of gapless CSLs [116, 117] (such as Dirac [118] and spinon Fermi surface [65] chiral QSLs), or conventional gapped CSLs.

As regards experimental realizations of the Shastry-Sutherland lattice, the field of quantum materials is currently witnessing the arrival of several new candidates whose magnetic lattices are based on rare-earth ions of Ce^{3+} [6], Pr^{3+} [7], Yb^{3+} [9], and Er^{3+} [10]. Some of these compounds offer tantalizing evidence of nonmagnetic behaviors at low temperatures and could thus potentially host exotic QSL phases, including in the presence of magnetic fields. Recent works [119, 120] have shown that these spin-orbit coupled systems are effectively described

by generalized XYZ models. In particular, $\text{Pr}_2\text{Ga}_2\text{BeO}_7$ has been argued to be described by a XXZ model to a first approximation [7]. In light of thermodynamic measurements observing a T^2 dependence of the specific heat, a finite κ_0/T (and an associated T -linear term in the specific heat) from a residual density of states ascribed to disorder, and gapless inelastic neutron spectra, the likely scenario is that of a QSL being realized. Indeed, it has been speculated [7] that a d -wave pairing \mathbb{Z}_2 QSL would be consistent with these experimental findings. Our \mathbb{Z}_2 QSL Z3000 is, in fact, a d -wave pairing state, and we believe that it would likely be stable to the introduction of XXZ anisotropy (similar to the kagome U(1) QSL, which is stable to XXZ anisotropy in the Hamiltonian [121]). Therefore, our work potentially sheds light on the precise microscopic character of the suspected QSL phase in $\text{Pr}_2\text{Ga}_2\text{BeO}_7$ as well. From symmetry considerations alone, a Dzyaloshinskii-Moriya interaction is also allowed [122, 123] and likely plays an important role in modeling the behavior of Shastry-Sutherland materials. Hence, to expand the applicability of our approach to these spin-orbit coupled rare-earth systems, one has to extend the *Ansätze* described herein by incorporating triplet amplitudes and evaluating their energetic competitiveness for the relevant anisotropic models [124]. Finally, QSL behavior has also been observed in a magnetic field, e.g., in $\text{Yb}_2\text{Be}_2\text{GeO}_7$ [9], so it would be important to determine the stability of the proposed \mathbb{Z}_2 Dirac QSL in a magnetic field, along the lines of the analysis performed for the kagome U(1) Dirac QSL in Ref. 125.

ACKNOWLEDGMENTS

We thank Federico Becca, Bryan Clark, Chunxiao Liu, Yukitoshi Motome, Yusuke Nomura, Karlo Penc, Rico Pohle, Mingpu Qin, Subir Sachdev, Anders Sandvik, Henry Shackleton, Yanting Teng, Chandra Varma, and Luciano Viteritti for helpful discussions. Y.I. thanks Luciano Viteritti and Federico Becca for providing us with the data from Ref. 46 and discussing the detailed comparison between ViT and VMC results. R.S. is supported by the Princeton Quantum Initiative Fellowship. The work of Y.I., J.Y.L., and R.S. was performed, in part, at the Aspen Center for Physics, which is supported by National Science Foundation Grant No. PHY-2210452 and a grant from the Simons Foundation (1161654, Troyer). This research was supported in part by grant NSF PHY-2309135 to the Kavli Institute for Theoretical Physics (KITP). Y.I. acknowledges support from the ICTP through the Associates Programme, from the Simons Foundation through Grant No. 284558FY19, IIT Madras through the Institute of Eminence (IoE) program for establishing QuCenDiEM (Project No. SP22231244CPETWOQCDHOC), and the International Centre for Theoretical Sciences (ICTS), Bengaluru during a visit for participating in the pro-

gram: Kagome off-scale (ICTS/KAGOFF2024/08). Y.I. also acknowledges the use of the computing resources at HPCE, IIT Madras. The work in Würzburg is supported by the Deutsche Forschungsgemeinschaft (DFG, German Research Foundation) through Project-ID 258499086 - SFB 1170 and through the Würzburg-Dresden Cluster of Excellence on Complexity and Topology in Quantum Matter - ct.qmat Project-ID 390858490 - EXC 2147. R.T. and F.F. thank IIT Madras for a IoE Visiting Scientist position which enabled the completion of this work.

Appendix A: Gauge-enriched symmetry relations

The relations between the different symmetry elements of the Shastry-Sutherland lattice are specified by the identities listed in Eq. (18). The projective extensions of these symmetries, $W_{\mathcal{O}}$, necessarily follow the same algebraic relations, which read as:

$$W_{T_x}^{-1}(T_x(\mathbf{r}))W_{T_y}^{-1}(T_x T_y(\mathbf{r}))W_{T_x}(T_x T_y(\mathbf{r}))W_{T_y}(T_y(\mathbf{r})) = F_3(\xi_y) \quad \text{or} \quad \eta_y \tau^0, \quad (\text{A1a})$$

$$W_{G_x}^{-1}(G_x(\mathbf{r}))W_{T_x}^{-1}(G_x T_x(\mathbf{r}))W_{G_x}(G_x T_x(\mathbf{r}))W_{T_x}(T_x(\mathbf{r})) = F_3(\xi_{G_{xx}}) \quad \text{or} \quad \eta_{G_{xx}} \tau^0, \quad (\text{A1b})$$

$$W_{G_x}^{-1}(G_x(\mathbf{r}))W_{T_y}^{-1}(G_x T_y(\mathbf{r}))W_{G_x}(G_x T_y(\mathbf{r}))W_{T_y}(T_y(\mathbf{r})) = F_3(\xi_{G_{xy}}) \quad \text{or} \quad \eta_{G_{xy}} \tau^0, \quad (\text{A1c})$$

$$W_{T_x}^{-1}(T_x(\mathbf{r}))W_{G_x}(T_x(\mathbf{r}))W_{G_x}(G_x(\mathbf{r})) = F_3(\xi_{G_x T_x}) \quad \text{or} \quad \eta_{G_x T_x} \tau^0, \quad (\text{A1d})$$

$$W_{T_y}^{-1}(T_y(\mathbf{r}))W_{\sigma_{xy}}^{-1}(T_x \sigma_{xy}(\mathbf{r}))W_{T_x}(T_x \sigma_{xy}(\mathbf{r}))W_{\sigma_{xy}}(\sigma_{xy}(\mathbf{r})) = F_3(\xi_{\sigma_{xy} T_x}) \quad \text{or} \quad \eta_{\sigma_{xy} T_x} \tau^0, \quad (\text{A1e})$$

$$W_{T_x}^{-1}(T_x(\mathbf{r}))W_{\sigma_{xy}}^{-1}(T_y \sigma_{xy}(\mathbf{r}))W_{T_y}(T_y \sigma_{xy}(\mathbf{r}))W_{\sigma_{xy}}(\sigma_{xy}(\mathbf{r})) = F_3(\xi_{\sigma_{xy} T_y}) \quad \text{or} \quad \eta_{\sigma_{xy} T_y} \tau^0, \quad (\text{A1f})$$

$$\begin{aligned} W_{\sigma_{xy}}(\mathbf{r})W_{G_x}(\sigma_{xy}^{-1}(\mathbf{r}))W_{\sigma_{xy}}((\sigma_{xy} G_x)^3(\mathbf{r}))W_{G_x}(G_x(\sigma_{xy} G_x)^2(\mathbf{r}))W_{\sigma_{xy}}((\sigma_{xy} G_x)^2(\mathbf{r})) \\ \times W_{G_x}(G_x \sigma_{xy} G_x(\mathbf{r}))W_{\sigma_{xy}}(\sigma_{xy} G_x(\mathbf{r}))W_{G_x}(G_x(\mathbf{r})) = F_3(\xi_{\sigma_{xy} G_x}) \quad \text{or} \quad \eta_{\sigma_{xy} G_x} \tau^0, \end{aligned} \quad (\text{A1g})$$

$$W_{\sigma_{xy}}(\sigma_{xy}(\mathbf{r}))W_{\sigma_{xy}}(\mathbf{r}) = F_3(\xi_{\sigma_{xy}}) \quad \text{or} \quad \eta_{\sigma_{xy}} \tau^0, \quad (\text{A1h})$$

$$W_{\mathcal{T}}(\mathbf{r})W_{\mathcal{T}}(\mathbf{r}) = F_3(\xi_{\mathcal{T}}) \quad \text{or} \quad \eta_{\mathcal{T}} \tau^0, \quad (\text{A1i})$$

$$W_{\mathcal{T}}(\mathbf{r})W_{\mathcal{O}}(\mathbf{r})W_{\mathcal{T}}^{-1}(\mathcal{O}^{-1}(\mathbf{r}))W_{\mathcal{O}}^{-1}(\mathbf{r}) = F_3(\xi_{\mathcal{TO}}) \quad \text{or} \quad \eta_{\mathcal{TO}} \tau^0. \quad (\text{A1j})$$

On the right-hand side of the equations above, the first expression defines the relations for the case of a U(1) IGG, where $0 \leq \xi_{\dots} < 2\pi$ is a global U(1) phase and, as defined in the main text, $F_3(\xi) \equiv \exp(i\xi\tau^z)$. The second set of expressions, following the ‘‘or’’, corresponds to a \mathbb{Z}_2 IGG, with $\eta_{\dots} = \pm 1$ being a global \mathbb{Z}_2 sign. As they stand, the different ξ and η are free parameters for now, but in the next two sections, we will see how different symmetry-related constraints fix their values, leading to distinct PSG solutions.

Appendix B: U(1) PSG classification

The canonical form of a U(1) *Ansatz* is given by

$$u_{ij} = i\chi_{ij}^0 \tau^0 + \chi_{ij}^3 \tau^z. \quad (\text{B1})$$

The structure of the gauge transformations that keep this canonical form intact is given by

$$W_{\mathcal{O}}(\mathbf{r}, u) = F_3(\phi_{\mathcal{O}}(m, n, u))(i\tau^x)^{w_{\mathcal{O}}}, \quad (\text{B2})$$

where $\mathcal{O} \in \{T_x, T_y, G_x, G_y, \sigma_{xy}, \mathcal{T}\}$, and $w_{\mathcal{O}}$ can take values 0 or 1. Now, we will systematically work out the possibilities for $w_{\mathcal{O}}$ and $\phi_{\mathcal{O}}$ one by one for the different symmetries.

1. Space-group symmetries

First, let us analyze the solutions for the space-group symmetries of the Shastry-Sutherland lattice. Starting with translations, the relations (B2) for $\mathcal{O} \in \{T_x, T_y\}$ can be explicitly written as :

$$W_{T_x}(m, n, u) = F_3(\phi_{T_x}(m, n, u))(i\tau^x)^{w_{T_x}}, \quad (\text{B3})$$

$$W_{T_y}(m, n, u) = F_3(\phi_{T_y}(m, n, u))(i\tau^x)^{w_{T_y}}.$$

According as the values of $w_{T_x/y}$, three cases may arise :

1. $w_{T_x} = 0, w_{T_y} = 0,$

2. $w_{T_x} = 1, w_{T_y} = 0,$

3. $w_{T_x} = 1, w_{T_y} = 1.$

It is readily seen that cases 2 and 3 can be excluded as these do not satisfy the conditions (A1)(d-f). Hence, we need to only consider the first, and we call this choice the ‘‘uniform gauge’’. Now, we can always choose a gauge transformation with the form $W(m, n, u) = F_3(\theta(m, n, u))$ such that we end up with:

$$W_{T_x}(m, 0, u) = W_{T_y}(m, n, u) = \tau^0. \quad (\text{B4})$$

With these settings, inserting Eq. (B4) into the symmetry condition (A1)(a) leads to the solutions for *all* \mathbf{r} :

$$\begin{aligned} W_{T_x}(m, n, u) &= F_3(n\xi_y), \\ W_{T_y}(m, n, u) &= \tau^0. \end{aligned} \quad (\text{B5})$$

These two equations define the allowed projective actions of translational symmetries.

Next, we consider the glide symmetry. With the notation $\Delta_i\phi_{\mathcal{O}}(m, n, u) \equiv \phi_{\mathcal{O}}(m, n, u) - \phi_{\mathcal{O}}[T_i^{-1}(m, n, u)]$ for $i = x, y$, Eqs. (A1)(b, c) tell us that

$$\begin{aligned} \Delta_i\phi_{G_x}(m, n, u) &= \phi_{T_i}(m, n, u) \\ &+ (-1)^{w_{G_x}}(\xi_{G_x} - \phi_{T_i}[G_x^{-1}(m, n, u)]), \end{aligned} \quad (\text{B6})$$

which, upon substitution of ϕ_{T_i} from Eq. (B5), yields

$$\begin{aligned} \Delta_x\phi_{G_x}(m, n, u) &= (-1)^{w_{G_x}}\xi_{G_{xx}} + [n(1 + (-1)^{w_{G_x}})]\xi_y \\ &+ [(-1)^{w_{G_x}}(\delta_{u,3} + \delta_{u,4})]\xi_y, \\ \Delta_y\phi_{G_x}(m, n, u) &= (-1)^{w_{G_x}}\xi_{G_{xy}}. \end{aligned} \quad (\text{B7})$$

We also have to satisfy the additional consistency condition:

$$\begin{aligned} \Delta_x\phi_{G_x}(m, n, u) + \Delta_y\phi_{G_x}[T_x^{-1}(m, n, u)] \\ = \Delta_y\phi_{G_x}(m, n, u) + \Delta_x\phi_{G_x}[T_y^{-1}(m, n, u)], \end{aligned} \quad (\text{B8})$$

which enforces that

$$[1 + (-1)^{w_{G_x}}]\xi_y = 0. \quad (\text{B9})$$

Thus, $w_{G_x} = 0$ implies that $2\xi_y = 0$, while there is no restriction if $w_{G_x} = 1$. Consequently, we obtain the general solution

$$\begin{aligned} \phi_{G_x}(m, n, u) &= (-1)^{w_{G_x}}(m\xi_{G_{xx}} + n\xi_{G_{xy}}) \\ &+ (-1)^{w_{G_x}}m\xi_y(\delta_{u,3} + \delta_{u,4}) + \bar{\phi}_{G_x,u}, \end{aligned} \quad (\text{B10})$$

using the shorthand $\bar{\phi}_{G_x,u} \equiv \phi_{G_x}(0, 0, u)$. Once ϕ_{G_x} is determined, we can plug it back into Eq. (B2), together with the associated value of w_{G_x} , to obtain the set of PSG elements.

Having dealt with translation and glide symmetries, we now turn to the mirror symmetry σ_{xy} . The gauge transformations accompanying reflections once again have the general form

$$W_{\sigma_{xy}} = F_3(\phi_{\sigma_{xy}}(m, n, u))(i\tau^x)^{w_{\sigma_{xy}}}. \quad (\text{B11})$$

Using Eqs. (A1)(i) and (A1)(j), the relations analogous to Eq. (B7) above read as:

$$\begin{aligned} \Delta_x\phi_{\sigma_{xy}}(m, n, u) &= -(-1)^{w_{\sigma_{xy}}}\xi_{\sigma_{xy}T_x} + n\xi_y \\ \Delta_y\phi_{\sigma_{xy}}(m, n, u) &= -(-1)^{w_{\sigma_{xy}}}(\xi_{\sigma_{xy}T_y} + m\xi_y). \end{aligned} \quad (\text{B12})$$

However, unlike Eq. (B8), the corresponding consistency condition for σ_{xy} does not impose any further restrictions on ξ_y . The final solution for $W_{\phi_{\sigma_{xy}}}$ is given by

$$\begin{aligned} \phi_{\sigma_{xy}}(m, n, u) &= -(-1)^{w_{\sigma_{xy}}}(m\xi_{\sigma_{xy}T_x} + n\xi_{\sigma_{xy}T_y}) \\ &+ mn\xi_y + \bar{\phi}_{\sigma_{xy},u}, \end{aligned} \quad (\text{B13})$$

which we can put back into Eq. (B11) to determine $W_{\sigma_{xy}}$.

While Eqs. (B5), (B10), and (B13) provide the general solutions for $\phi_{\mathcal{O}}$, these may not be gauge independent. In fact, the U(1) phases derived above can be greatly simplified or fixed by the use of a local gauge transformation $W(m, n, u)$ under which

$$W_{\mathcal{O}}(m, n, u) \rightarrow W^\dagger(m, n, u)W_{\mathcal{O}}(m, n, u)W[\mathcal{O}^{-1}(m, n, u)].$$

To demonstrate this, let us choose a gauge transformation (which is independent of the sublattice index),

$$W(m, n, u) = F_3(m\theta_x + n\theta_y). \quad (\text{B14})$$

With the proper choices of θ_x and θ_y , one can then set

$$\begin{aligned} \xi_{\sigma_{xy}T_x} &= 0, \\ \text{for } w_{G_x} = 0: \xi_{G_{xy}} &= 0, \\ \text{for } w_{G_x} = 1: \xi_{G_{xx}} &= 0. \end{aligned} \quad (\text{B15})$$

Thereafter, using a sublattice-dependent gauge transformation $W(m, n, u) = F_3(\theta_u)$ with $\theta_2 = (-1)^{w_{G_x}}(\theta_1 - \bar{\phi}_{G_x,1})$, $\theta_3 = \bar{\phi}_{G_x,3} + (-1)^{w_{G_x}}\theta_4$, $\theta_4 = (-1)^{w_{\sigma_{xy}}}(\theta_2 - \bar{\phi}_{\sigma_{xy},2})$, we can fix the following:

$$\bar{\phi}_{G_x,1} = \bar{\phi}_{G_x,3} = \bar{\phi}_{\sigma_{xy},2} = 0 = \bar{\phi}_{\sigma_{xy},1}\delta_{w_{\sigma_{xy}},1}, \quad (\text{B16})$$

which drastically simplifies Eqs. (B10) and (B13).

Continuing in this spirit, we shall exploit the remaining conditions from Eq. (A1) to further fix the free parameters. For instance, using Eqs. (B15) and (B16), Eq. (A1)(d) yields

$$\begin{aligned} \text{for } w_{G_x} = 0: \xi_y &= \xi_{G_{xx}} = \xi_{G_{xy}} = 0, \\ \bar{\phi}_{G_x,2} &= \bar{\phi}_{G_x,4} = \xi_{G_xT_x}; \\ \text{for } w_{G_x} = 1: \xi_{G_{xx}} &= \xi_y + 2\xi_{G_{xy}} = 0, \\ \bar{\phi}_{G_x,2} &= n_{G_xT_x}\pi = \bar{\phi}_{G_x,4} + \xi_{G_{xy}}. \end{aligned} \quad (\text{B17})$$

Likewise, Eq. (A1)(h) asserts that

$$\xi_{\sigma_{xy}T_y} = 0, [1 + (-1)^{w_{\sigma_{xy}}}] \xi_y = 0, \quad (\text{B18})$$

$$\bar{\phi}_{\sigma_{xy},u} + (-1)^{w_{\sigma_{xy}}}\bar{\phi}_{\sigma_{xy},\sigma_{xy}(u)} = \xi_{\sigma_{xy}}. \quad (\text{B19})$$

Then, putting the content of Eq. (B16) into Eq. (B19), one arrives at the following result for $\bar{\phi}_{\sigma_{xy},u}$:

$$w_{\sigma_{xy}} = 0: \bar{\phi}_{\sigma_{xy},u} = \{\bar{\phi}_{\sigma_{xy}}, 0, \bar{\phi}_{\sigma_{xy}} + n_{\sigma_{xy}}\pi, 2\bar{\phi}_{\sigma_{xy}}\},$$

$$w_{\sigma_{xy}} = 1 : \bar{\phi}_{\sigma_{xy},u} = \{0, 0, \bar{\phi}_{\sigma_{xy}}, 0\}. \quad (\text{B20})$$

We are still left with one more lattice symmetry condition given by Eq. (A1)(g), which imposes further constraints in two cases:

$$(w_{G_x}, w_{\sigma_{xy}}) = (1, 0) : 2\xi_{G_{xy}} = 0 \implies \xi_y = 0, \quad (\text{B21})$$

$$(w_{G_x}, w_{\sigma_{xy}}) = (0, 1) : \bar{\phi}_{\sigma_{xy}} = 2\xi_{G_x T_x} + n_{\sigma_{xy}} \pi. \quad (\text{B22})$$

A simple gauge choice is possible for the case with $w_{G_x} = 0$ as follows⁶. Employing a gauge transformation of the form $W(m, n, u) = F_3(\theta_u)$ with $\theta_2 = \theta_1 + \xi_{G_x T_x}/2$ and $\theta_4 = \theta_3 + \xi_{G_x T_x}/2$, one can set

$$\bar{\phi}_{G_x, u} = \xi_{G_x T_x}/2 \implies \bar{\phi}_{G_x, u} = 0. \quad (\text{B23})$$

On the right-hand side above, we have used the gauge freedom which allows us to set a global U(1) phase to zero. Due to this gauge transformation, $\bar{\phi}_{\sigma_{xy}, u}$ will also necessarily be modified, but we can still exploit the freedom to choose θ_1 and θ_3 . For $w_{\sigma_{xy}} = 0$, choosing $\theta_3 = \theta_1 + \bar{\phi}_{\sigma_{xy}}$, we obtain

$$\begin{aligned} \bar{\phi}_{\sigma_{xy}, u} &= \{\bar{\phi}_{\sigma_{xy}}, \bar{\phi}_{\sigma_{xy}}, \bar{\phi}_{\sigma_{xy}} + n_{\sigma_{xy}} \pi, \bar{\phi}_{\sigma_{xy}}\}, \\ \implies \bar{\phi}_{\sigma_{xy}, u} &= \{0, 0, n_{\sigma_{xy}} \pi, 0\}. \end{aligned} \quad (\text{B24})$$

On the other hand, for $w_{\sigma_{xy}} = 1$, we choose $\theta_1 = 0$, $\theta_3 = -\xi_{G_x T_x}$, which leads to

$$\bar{\phi}_{\sigma_{xy}, u} = \{0, 0, \bar{\phi}_{\sigma_{xy}} + 2\xi_{G_x T_x}, 0\},$$

and, for simplicity, we will redefine $\bar{\phi}_{\sigma_{xy}} + 2\xi_{G_x T_x} \rightarrow \bar{\phi}_{\sigma_{xy}}$.

The upshot of this sequence of operations is that we have now specified all the values of $\bar{\phi}_{\mathcal{O}}$ and ξ_{\dots} that determine $\phi_{\mathcal{O}}$ for all space-group symmetries \mathcal{O} . In turn, $\phi_{\mathcal{O}}$ —together with different combinations of $w_{\mathcal{O}}$ —then feeds into Eq. (B2) and defines the PSGs.

2. Time-reversal symmetry

Per Eq. (B2), the gauge transformation associated with time reversal takes the form

$$W_{\mathcal{T}}(\mathbf{r}, u) = F_3(\phi_{\mathcal{T}}(m, n, u))(i\tau^x)^{w_{\mathcal{T}}}. \quad (\text{B25})$$

Following Eq. (A1)(j) for $\mathcal{O} \in \{T_x, T_y\}$, we find (for both $w_{\mathcal{T}} = 0$ and $w_{\mathcal{T}} = 1$) that

$$\phi_{\mathcal{T}}(m, n, u) = m \xi_{\mathcal{T}_x} + n \xi_{\mathcal{T}_y} + \bar{\phi}_{\mathcal{T}, u}. \quad (\text{B26})$$

As for Eq. (B8) earlier, the consistency condition yields

$$[1 - (-1)^{w_{\mathcal{T}}}] \xi_y = 0, \quad (\text{B27})$$

which implies that for $w_{\mathcal{T}} = 1$, $2\xi_y = 0$.

To fix the rest of the parameters, it is convenient to consider the two possible values of $w_{\mathcal{T}}$ separately.

⁶ No such uniform choice of $\bar{\phi}_{G_x, u}$ is possible for $w_{G_x} = 1$, so we will continue to use the existing gauge choice in that case.

$$a. \quad w_{\mathcal{T}} = 0$$

In this case, the symmetry relation (A1)(i) gives

$$2\xi_{\mathcal{T}_x} = 2\xi_{\mathcal{T}_y} = 0, \quad \bar{\phi}_{\mathcal{T}, u} = \bar{\phi}_{\mathcal{T}} + n_u \pi = n_u \pi, \quad (\text{B28})$$

where the gauge freedom can be utilized to set $\bar{\phi}_{\mathcal{T}} = 0$. Now, using the equation above and Eq. (A1)(j) for $\mathcal{O} = G_x, \sigma_{xy}$, one can fix:

$$\xi_{\mathcal{T}_x} = \xi_{\mathcal{T}_y} = 0. \quad (\text{B29})$$

Note that having an *Ansatz* with nonvanishing amplitudes on NN bonds requires that

$$\bar{\phi}_{\mathcal{T}, u} = u \pi. \quad (\text{B30})$$

However, since diagonal bonds connect sites with both even or odd values of the sublattice index u , this also implies that choosing such a gauge for time reversal results in vanishing *Ansätze* on the NNN bonds.

$$b. \quad w_{\mathcal{T}} = 1$$

When $w_{\mathcal{T}} = 1$, it is always possible to choose a gauge such that $\phi_{\mathcal{T}}(m, n, u) = 0$. The advantage of such a choice is that the mean-field parameters on all the bonds then comprise only real hopping terms.

Here, we demonstrate this process for the case of $w_{G_x} = w_{\sigma_{xy}} = 0$. First, we perform a gauge transformation given by,

$$W_{\mathcal{T}}(m, n, u) = F_3 \left(m \frac{\xi_{\mathcal{T}_x}}{2} + n \frac{\xi_{\mathcal{T}_y}}{2} + \frac{\bar{\phi}_{\mathcal{T}, u}}{2} \right). \quad (\text{B31})$$

This immediately sets

$$\phi_{\mathcal{T}}(m, n, u) \rightarrow \tilde{\phi}_{\mathcal{T}}(m, n, u) = 0. \quad (\text{B32})$$

The price we pay for this is that ϕ_{G_x} and ϕ_{σ} will also be modified simultaneously to

$$\begin{aligned} \tilde{\phi}_{G_x} &= -n \xi_{\mathcal{T}_y} + \frac{\bar{\phi}_{\mathcal{T}, 2} - \bar{\phi}_{\mathcal{T}, 1}}{2} (\delta_{u, 1} - \delta_{u, 2}) \\ &\quad + \frac{\bar{\phi}_{\mathcal{T}, 4} - \bar{\phi}_{\mathcal{T}, 3}}{2} (\delta_{u, 3} - \delta_{u, 4}) \\ &\quad - \frac{\xi_{\mathcal{T}_x}}{2} (\delta_{u, 1} + \delta_{u, 4}) - \frac{\xi_{\mathcal{T}_y}}{2} (\delta_{u, 3} + \delta_{u, 4}), \end{aligned} \quad (\text{B33})$$

$$\begin{aligned} \tilde{\phi}_{\sigma_{xy}} &= (n - m) \frac{\xi_{\mathcal{T}_x} - \xi_{\mathcal{T}_y}}{2} + p_{\sigma_{xy}} \pi \delta_{u, 3} \\ &\quad + \frac{\bar{\phi}_{\mathcal{T}, 4} - \bar{\phi}_{\mathcal{T}, 2}}{2} (\delta_{u, 2} - \delta_{u, 4}), \end{aligned} \quad (\text{B34})$$

with $p_{\sigma_{xy}} = 0, 1$. For notational convenience, we drop the tilde on ϕ hereafter.

Lastly, making use of Eq. (A1)(j) produces two other constraints:

$$\xi_{\mathcal{T}G_x} = -2\phi_{G_x}(m, n, u), \quad (\text{B35})$$

$$\xi_{\mathcal{T}\sigma_{xy}} = -2\phi_{\sigma_{xy}}(m, n, u), \quad (\text{B36})$$

leading to the relations:

$$2\xi_{\mathcal{T}y} = 0 \Rightarrow \xi_{\mathcal{T}y} = p_{G_{xy}}\pi, \quad (\text{B37})$$

$$\xi_{\mathcal{T}x} = \xi_{\mathcal{T}y} = p_{G_{xy}}\pi, \quad (\text{B38})$$

$$\bar{\phi}_{\mathcal{T},2} = \bar{\phi}_{\mathcal{T},4}, \quad \bar{\phi}_{\mathcal{T},1} = \bar{\phi}_{\mathcal{T},3}, \quad (\text{B39})$$

$$2(\bar{\phi}_{\mathcal{T},2} - \bar{\phi}_{\mathcal{T},1}) = p_{G_{xy}}\pi, \quad (\text{B40})$$

$$\Rightarrow \bar{\phi}_{\mathcal{T},2} = \bar{\phi}_{\mathcal{T},1} + \frac{p_{G_{xy}}\pi}{2} + p_{G_x T_x}\pi,$$

where both $p_{G_{xy}}$ and $p_{G_x T_x}$ take values 0 or 1. Combining these equations and performing an appropriate global phase shift, the end result is

$$\phi_{G_x}(m, n, u) = p_{G_{xy}}\pi(n + \delta_{u,4}) + p_{G_x T_x}\pi(\delta_{u,2} + \delta_{u,4}), \quad (\text{B41})$$

$$\phi_{\sigma_{xy}}(m, n, u) = p_{\sigma_{xy}}\pi\delta_{u,3}, \quad (\text{B42})$$

for the class $w_{G_x} = w_{\sigma_{xy}} = 0, w_{\mathcal{T}} = +1$.

The PSGs for the other classes can be straightforwardly worked out in the same manner. We summarize all the U(1) PSGs thus obtained in Eqs. (22)–(25) and Table I.

Appendix C: \mathbb{Z}_2 PSG classification

The PSGs for a \mathbb{Z}_2 IGG can be derived in similar fashion to the U(1) case. We proceed, as before, by considering the spatial and time-reversal symmetries separately.

1. Space-group symmetries

Exploiting the local gauge redundancy, we first fix:

$$W_{T_x}(m, 0, u) = W_{T_y}(m, n, u) = \tau^0. \quad (\text{C1})$$

With these settings, the symmetry condition (A1)(a) directly leads to the following solutions for the translational PSGs:

$$\begin{aligned} W_{T_x}(m, n, u) &= \eta_y^y \tau^0, \\ W_{T_y}(m, n, u) &= \tau^0, \end{aligned} \quad (\text{C2})$$

where η_y (and all other parameters η_{\dots} introduced hereafter) can be ± 1 .

Let us introduce the notation $\Omega_i[W_{\mathcal{O}}(m, n, u)] \equiv W_{\mathcal{O}}(m, n, u)W_{\mathcal{O}}[T_i^{-1}(m, n, u)]$ for $i = x, y$. In this language, after substituting Eq. (C2) into Eqs. (A1)(b, c),

we find

$$\begin{aligned} \Omega_x[W_{G_x}(m, n, u)] &= \eta_{G_{xx}}\eta_y^{-(\delta_{u,3}+\delta_{u,4})}\tau^0, \\ \Omega_y[W_{G_x}(m, n, u)] &= \eta_{G_{xy}}\tau^0. \end{aligned} \quad (\text{C3})$$

Akin to the U(1) case, we can identify a consistency equation as

$$\begin{aligned} \Omega_x[W_{G_x}(m, n, u)]\Omega_y[W_{G_x}[T_x^{-1}(m, n, u)]] &= \\ \Omega_y[W_{G_x}(m, n, u)]\Omega_x[W_{G_x}[T_y^{-1}(m, n, u)]]; \end{aligned} \quad (\text{C4})$$

however, this does not impose any new constraints. Resultantly, the solution for W_{G_x} takes the generic form:

$$W_{G_x}(m, n, u) = \eta_{G_{xx}}^m \eta_{G_{xy}}^n \eta_y^{-m(\delta_{u,3}+\delta_{u,4})} \mathcal{W}_{G_x, u}, \quad (\text{C5})$$

where $\mathcal{W}_{G_x, u}$ is a sublattice-dependent Pauli matrix in pseudospin space.

Likewise the solution for $W_{\sigma_{xy}}$ can be directly obtained from Eqs. (A1)(e, f) as

$$W_{\sigma_{xy}}(m, n, u) = \eta_{\sigma_{xy} T_x}^m \eta_{\sigma_{xy} T_y}^n \eta_y^{mn} \mathcal{W}_{\sigma_{xy}, u}. \quad (\text{C6})$$

Once again, we can try to simplify the PSG solutions by a clever choice of gauge transformations. Note that a local transformation of the form $W(m, n, u) = \eta_M^m \eta_N^n \tau^0$ does not impact the projective operation of translations. However, they do modify the spatial dependencies of $W_{\sigma_{xy}}$ and W_{G_x} . On choosing η_M and η_N appropriately, one can set

$$\eta_{\sigma_{xy} T_x} = +1. \quad (\text{C7})$$

Combining this with a sublattice-dependent gauge transformation of the form $W(m, n, u) = W_u$, we fix

$$\mathcal{W}_{G_x,1} = \mathcal{W}_{G_x,3} = \mathcal{W}_{\sigma_{xy},2} = \tau^0. \quad (\text{C8})$$

Then, using Eq. (C8) in Eq. (A1)(c), we find

$$\begin{aligned} \eta_y = \eta_{G_{xx}} &= 0, \\ \mathcal{W}_{G_x,2} = \eta_{G_{xy}} \mathcal{W}_{G_x,4} &= \eta_{G_x T_x}. \end{aligned} \quad (\text{C9})$$

At the same time, Eq. (A1)(h) gives

$$\eta_{\sigma_{xy} T_y} = +1, \quad \mathcal{W}_{\sigma_{xy}, u} \mathcal{W}_{\sigma_{xy}, \sigma_{xy}(u)} = \eta_{\sigma_{xy}} \tau^0. \quad (\text{C10})$$

In addition, we are left with one more lattice symmetry condition given by Eq. (A1). Using this together with the information from Eqs. (C8) and (C10), we obtain

$$\mathcal{W}_{\sigma_{xy}, u} = \begin{cases} \{\eta_{\sigma_{xy},1}\tau^0, \tau^0, \eta_{\sigma_{xy},3}\tau^0, \tau^0\}; & \text{for } \eta_{\sigma_{xy}} = +1 \\ \{i\tau^z, \tau^0, \eta_{\sigma_{xy},3}i\tau^z, -\tau^0\}; & \text{for } \eta_{\sigma_{xy}} = -1 \end{cases}. \quad (\text{C11})$$

At this point, yet another set of gauge transformations, defined by $W(m, n, u) = (\eta_{\sigma_{xy},1})^{(\delta_{u,1}+\delta_{u,2})}$ for $\eta_{\sigma_{xy}} = +1$ and $W(m, n, u) = (i\tau^z)^{(\delta_{u,3}+\delta_{u,4})}$ for $\eta_{\sigma_{xy}} = -1$, lead to

$$\mathcal{W}_{\sigma_{xy}, u} = \begin{cases} \{1, 1, \eta_{\sigma_{xy},3}\eta_{\sigma_{xy},1}, 1\}\eta_{\sigma_{xy},1}\tau^0; & \text{for } \eta_{\sigma_{xy}} = +1 \\ \{1, 1, \eta_{\sigma_{xy},3}, 1\}i\tau^z; & \text{for } \eta_{\sigma_{xy}} = -1 \end{cases}. \quad (\text{C12})$$

Now, by virtue of the IGG freedom, we can drop the global sign parameter $\eta_{\sigma_{xy},1}$ in the first case above. Furthermore, we define a new parameter $\eta_\sigma \equiv \eta_{\sigma_{xy},3}\eta_{\sigma_{xy},1}$ and $\eta_\sigma \equiv \eta_{\sigma_{xy},3}$ for $\eta_{\sigma_{xy}} = +1$ and $\eta_{\sigma_{xy}} = -1$, respectively. This results in the compact expression

$$\mathcal{W}_{\sigma_{xy},u} = (\eta_\sigma)^{\delta_{u,3}} \mathcal{W}_\sigma, \quad (\text{C13})$$

where $\mathcal{W}_\sigma = \tau^0 (i\tau^z)$ for positive (negative) $\eta_{\sigma_{xy}}$.

2. Time-reversal symmetry

To compute the PSG solutions for time reversal, we can again use Eq. (A1)(j) for $\mathcal{O} \in \{T_x, T_y\}$, which directly yields

$$W_{\mathcal{T}}(m, n, u) = \eta_{\mathcal{T}T_x}^m \eta_{\mathcal{T}T_y}^n \mathcal{W}_{\mathcal{T},u}. \quad (\text{C14})$$

It is easy to see that Eqs. (A1)(i,j) with $\mathcal{O} \in \{G_x, \sigma_{xy}\}$ will now introduce four extra conditions, namely,

$$\eta_{\mathcal{T}T_x} = \eta_{\mathcal{T}T_y}, \quad (\text{C15a})$$

$$\mathcal{W}_{\mathcal{T},u}^2 = \eta_{\mathcal{T}}, \quad (\text{C15b})$$

$$\mathcal{W}_{\mathcal{T},u} \mathcal{W}_{\sigma_{xy},u} = \eta_{\sigma_{xy}} \mathcal{T} \mathcal{W}_{\sigma_{xy},u} \mathcal{W}_{\mathcal{T},\sigma_{xy}^{-1}(u)}, \quad (\text{C15c})$$

$$\mathcal{W}_{\mathcal{T},u} \mathcal{W}_{G_x,u} = \eta_{G_x} \mathcal{T} \eta_{\mathcal{T}T_x}^{(u \bmod 2)} \mathcal{W}_{G_x,u} \mathcal{W}_{\mathcal{T},G_x^{-1}(u)}. \quad (\text{C15d})$$

A summary of all the \mathbb{Z}_2 PSGs constructed from these relations is provided by Eqs. (26)–(29) and Table II.

Appendix D: Mapping to square-lattice PSGs

As discussed in Sec. III C, the square-lattice space group, $p4$, can be generated from that of the Shastry-Sutherland lattice, $p4g$, by incorporating the symmetry σ_x of reflections about the x -axis. This imposes certain additional symmetry relations, which are as follows:

$$\sigma_x^{-1} T_x^{-1} \sigma_x T_x = \mathbb{1}, \quad (\text{D1a})$$

$$\sigma_x^{-1} T_y^{-1} \sigma_x T_y = \mathbb{1}, \quad (\text{D1b})$$

$$G_x^{-1} \sigma_x G_x \sigma_x = \mathbb{1}, \quad (\text{D1c})$$

$$(\sigma_x \sigma_{xy})^4 = \mathbb{1}, \quad (\text{D1d})$$

$$\sigma_x^2 = \mathbb{1}, \quad (\text{D1e})$$

$$(\sigma_{xy} \sigma_x^{-1} G_x^{-1})^2 (\sigma_{xy} G_x \sigma_x)^2 = \mathbb{1}, \quad (\text{D1f})$$

$$(\sigma_x G_x \sigma_{xy} \sigma_x \sigma_{xy})^2 = \mathbb{1}, \quad (\text{D1g})$$

$$\mathcal{T} \sigma_x \mathcal{T}^{-1} \sigma_x^{-1} = \mathbb{1}. \quad (\text{D1h})$$

Using this information, we can now deduce the PSGs for the enlarged space group which includes σ_x . For example, from Eqs. (D1a) and (D1b), we find the projective implementation

$$W_{\sigma_x}(m, n, u) = \eta_{\sigma_x T_x}^m \eta_{\sigma_x T_y}^n \mathcal{W}_{\sigma_x,u}. \quad (\text{D2})$$

Similarly, the rest of the relations in Eq. (D1) can be harnessed to impose further constraints such as $\eta_{\sigma_x T_x} = \eta_{\sigma_x T_y} = +1$ in the solution above, as well as $\eta_{G_x} = +1$ in Eq. (27). Systematically considering all the gauge-equivalent choices of $\mathcal{W}_{\sigma_x,u}$ that satisfy these symmetry constraints, we are led from the PSGs listed in Table II to the set in Table IX. Note that there are four η parameters and a total of 17 rows in the table. Thus, the total number of PSGs for the $p4$ symmetry group is $2^4 \times 17 = 272$; this is indeed the number of PSGs enumerated in the square-lattice classification by Wen [55].

To illustrate the one-to-one mapping between each row of Table IX and the PSG structure obtained in Ref. 55, we need to rewrite the PSGs in terms of the projective realization of $\{T_1, T_2, \sigma_x, \sigma_y, \sigma_{xy}\}$ ⁷ and \mathcal{T} . As T_1, T_2 , and σ_y can be generated using only G_x, σ_x , and σ_{xy} , the projective extensions $W_{T_1}(m, n, u), W_{T_2}(m, n, u)$ and $W_{\sigma_y}(m, n, u)$ can be derived using $W_{G_x}(m, n, u), W_{\sigma_x}(m, n, u)$, and $W_{\sigma_{xy}}(m, n, u)$. Recalling the relations compiled in Eq. (42), we write the corresponding projective realizations as

$$W_{T_1}(m, n, u) = \eta_{T_1} W_{G_x}(m, n, u) W_{\sigma_x} [G_x^{-1}(m, n, u)], \quad (\text{D3})$$

$$W_{T_2}(m, n, u) = \eta_{T_2} W_{\sigma_{xy}}(m, n, u) W_{T_1} [\sigma_{xy}(m, n, u)] W_{\sigma_{xy}} [T_1^{-1} \sigma_{xy}(m, n, u)], \quad (\text{D4})$$

$$W_{\sigma_y}(m, n, u) = \eta_{\sigma_y} W_{\sigma_{xy}}(m, n, u) W_{\sigma_x} [\sigma_{xy}(m, n, u)] W_{\sigma_{xy}} [\sigma_x^{-1} \sigma_{xy}(m, n, u)]. \quad (\text{D5})$$

Note that the global sign parameters η_{T_1}, η_{T_2} , and η_{σ_y} can be set to +1 using the gauge freedom. This results in the solution:

$$W_{T_1}(m, n, u) = \{\eta_{\sigma_x G_x}, \eta_{G_x T_x}, \eta_{\sigma_x G_x}, \eta_{G_x T_x}\} \mathcal{W}_{T_1}, \quad (\text{D6})$$

$$W_{T_2}(m, n, u) = \{\eta_{\sigma_x G_x}, \eta_\sigma \eta_{G_x T_x}, \eta_\sigma \eta_{\sigma_x G_x}, \eta_{G_x T_x}\} \mathcal{W}_{T_2}, \quad (\text{D7})$$

$$W_{\sigma_y}(m, n, u) = \{1, \eta_{\sigma_x G_x}, 1, \eta_{\sigma_x G_x}\} \mathcal{W}_{\sigma_y}, \quad (\text{D8})$$

$$W_{\sigma_x}(m, n, u) = \{1, \eta_{\sigma_x G_x}, 1, \eta_{\sigma_x G_x}\} \mathcal{W}_{\sigma_x}, \quad (\text{D9})$$

$$W_{\sigma_{xy}}(m, n, u) = \{1, 1, \eta_\sigma, 1\} \mathcal{W}_{\sigma_{xy}}, \quad (\text{D10})$$

$$W_{\mathcal{T}}(m, n, u) = \{1, \eta_{G_x \mathcal{T}}, 1, \eta_{G_x \mathcal{T}}\} \mathcal{W}_{\mathcal{T}}. \quad (\text{D11})$$

The associated matrices \mathcal{W} are listed in Table X.

To simplify these expressions even further, we can now implement a gauge transformation with $W(m, n, u) = (\eta_{\sigma_x G_x} \eta_{G_x T_x})^{m+n} \{\eta_{\sigma_x G_x} \eta_{G_x T_x}, \eta_{\sigma_x G_x}, \eta_\sigma, \eta_{\sigma_x G_x}\}$, which brings us to

$$W_{T_1}(m, n, u) = \{1, 1, \eta_\sigma, \eta_\sigma\} \mathcal{W}_{T_1}, \quad (\text{D12})$$

⁷ In Ref. 55, $\sigma_x, \sigma_y, \sigma_{xy}$ are denoted as P_y, P_x and P_{xy} , respectively.

PSG No.	$\mathcal{W}_{\sigma_{xy},u}$	$\mathcal{W}_{\mathcal{T},u}$	$\mathcal{W}_{\sigma_x,u}$
1(a)	$\{\tau^0, \tau^0, \eta_\sigma \tau^0, \tau^0\}$	$\{\tau^0, \eta_{G_x \mathcal{T}} \tau^0, \tau^0, \eta_{G_x \mathcal{T}} \tau^0\}$	$\{\tau^0, \eta_{\sigma_x G_x} \tau^0, \tau^0, \eta_{\sigma_x G_x} \tau^0\}$
1(b)	$\{\tau^0, \tau^0, \eta_\sigma \tau^0, \tau^0\}$	$\{\tau^0, \eta_{G_x \mathcal{T}} \tau^0, \tau^0, \eta_{G_x \mathcal{T}} \tau^0\}$	$\{i\tau^z, \eta_{\sigma_x G_x} i\tau^z, i\tau^z, \eta_{\sigma_x G_x} i\tau^z\}$
2(a)	$\{\tau^0, \tau^0, \eta_\sigma \tau^0, \tau^0\}$	$\{i\tau^y, \eta_{G_x \mathcal{T}} i\tau^y, i\tau^y, \eta_{G_x \mathcal{T}} i\tau^y\}$	$\{\tau^0, \eta_{\sigma_x G_x} \tau^0, \tau^0, \eta_{\sigma_x G_x} \tau^0\}$
2(b)	$\{\tau^0, \tau^0, \eta_\sigma \tau^0, \tau^0\}$	$\{i\tau^y, \eta_{G_x \mathcal{T}} i\tau^y, i\tau^y, \eta_{G_x \mathcal{T}} i\tau^y\}$	$\{i\tau^z, \eta_{\sigma_x G_x} i\tau^z, i\tau^z, \eta_{\sigma_x G_x} i\tau^z\}$
2(c)	$\{\tau^0, \tau^0, \eta_\sigma \tau^0, \tau^0\}$	$\{i\tau^y, \eta_{G_x \mathcal{T}} i\tau^y, i\tau^y, \eta_{G_x \mathcal{T}} i\tau^y\}$	$\{i\tau^y, \eta_{\sigma_x G_x} i\tau^y, i\tau^y, \eta_{\sigma_x G_x} i\tau^y\}$
3(a)	$\{i\tau^z, i\tau^z, \eta_\sigma i\tau^z, i\tau^z\}$	$\{i\tau^y, \eta_{G_x \mathcal{T}} i\tau^y, i\tau^y, \eta_{G_x \mathcal{T}} i\tau^y\}$	$\{\tau^0, \eta_{\sigma_x G_x} \tau^0, \tau^0, \eta_{\sigma_x G_x} \tau^0\}$
3(b)	$\{i\tau^z, i\tau^z, \eta_\sigma i\tau^z, i\tau^z\}$	$\{i\tau^y, \eta_{G_x \mathcal{T}} i\tau^y, i\tau^y, \eta_{G_x \mathcal{T}} i\tau^y\}$	$\{i\tau^z, \eta_{\sigma_x G_x} i\tau^z, i\tau^z, \eta_{\sigma_x G_x} i\tau^z\}$
3(c)	$\{i\tau^z, i\tau^z, \eta_\sigma i\tau^z, i\tau^z\}$	$\{i\tau^y, \eta_{G_x \mathcal{T}} i\tau^y, i\tau^y, \eta_{G_x \mathcal{T}} i\tau^y\}$	$\{i\tau^y, \eta_{\sigma_x G_x} i\tau^y, i\tau^y, \eta_{\sigma_x G_x} i\tau^y\}$
3(d)	$\{i\tau^z, i\tau^z, \eta_\sigma i\tau^z, i\tau^z\}$	$\{i\tau^y, \eta_{G_x \mathcal{T}} i\tau^y, i\tau^y, \eta_{G_x \mathcal{T}} i\tau^y\}$	$\{i\tau^x, \eta_{\sigma_x G_x} i\tau^x, i\tau^x, \eta_{\sigma_x G_x} i\tau^x\}$
3(e)	$\{i\tau^z, i\tau^z, \eta_\sigma i\tau^z, i\tau^z\}$	$\{i\tau^y, \eta_{G_x \mathcal{T}} i\tau^y, i\tau^y, \eta_{G_x \mathcal{T}} i\tau^y\}$	$\{i\tau^{zx}, \eta_{\sigma_x G_x} i\tau^{zx}, i\tau^{zx}, \eta_{\sigma_x G_x} i\tau^{zx}\}$
4(a)	$\{i\tau^z, i\tau^z, \eta_\sigma i\tau^z, i\tau^z\}$	$\{i\tau^z, \eta_{G_x \mathcal{T}} i\tau^z, i\tau^z, \eta_{G_x \mathcal{T}} i\tau^z\}$	$\{\tau^0, \eta_{\sigma_x G_x} \tau^0, \tau^0, \eta_{\sigma_x G_x} \tau^0\}$
4(b)	$\{i\tau^z, i\tau^z, \eta_\sigma i\tau^z, i\tau^z\}$	$\{i\tau^z, \eta_{G_x \mathcal{T}} i\tau^z, i\tau^z, \eta_{G_x \mathcal{T}} i\tau^z\}$	$\{i\tau^z, \eta_{\sigma_x G_x} i\tau^z, i\tau^z, \eta_{\sigma_x G_x} i\tau^z\}$
4(c)	$\{i\tau^z, i\tau^z, \eta_\sigma i\tau^z, i\tau^z\}$	$\{i\tau^z, \eta_{G_x \mathcal{T}} i\tau^z, i\tau^z, \eta_{G_x \mathcal{T}} i\tau^z\}$	$\{i\tau^y, \eta_{\sigma_x G_x} i\tau^y, i\tau^y, \eta_{\sigma_x G_x} i\tau^y\}$
5(a)	$\{i\tau^z, i\tau^z, \eta_\sigma i\tau^z, i\tau^z\}$	$\{\tau^0, \eta_{G_x \mathcal{T}} \tau^0, \tau^0, \eta_{G_x \mathcal{T}} \tau^0\}$	$\{\tau^0, \eta_{\sigma_x G_x} \tau^0, \tau^0, \eta_{\sigma_x G_x} \tau^0\}$
5(b)	$\{i\tau^z, i\tau^z, \eta_\sigma i\tau^z, i\tau^z\}$	$\{\tau^0, \eta_{G_x \mathcal{T}} \tau^0, \tau^0, \eta_{G_x \mathcal{T}} \tau^0\}$	$\{i\tau^z, \eta_{\sigma_x G_x} i\tau^z, i\tau^z, \eta_{\sigma_x G_x} i\tau^z\}$
5(c)	$\{i\tau^z, i\tau^z, \eta_\sigma i\tau^z, i\tau^z\}$	$\{\tau^0, \eta_{G_x \mathcal{T}} \tau^0, \tau^0, \eta_{G_x \mathcal{T}} \tau^0\}$	$\{i\tau^y, \eta_{\sigma_x G_x} i\tau^y, i\tau^y, \eta_{\sigma_x G_x} i\tau^y\}$
5(d)	$\{i\tau^z, i\tau^z, \eta_\sigma i\tau^z, i\tau^z\}$	$\{\tau^0, \eta_{G_x \mathcal{T}} \tau^0, \tau^0, \eta_{G_x \mathcal{T}} \tau^0\}$	$\{i\tau^{zx}, \eta_{\sigma_x G_x} i\tau^{zx}, i\tau^{zx}, \eta_{\sigma_x G_x} i\tau^{zx}\}$

TABLE IX. All gauge-inequivalent PSGs corresponding to the full $p4$ space-group symmetry. The choices of $\mathcal{W}_{G_x,u}$ are the same for each row and are given by $\mathcal{W}_{G_x,u} = \{\tau^0, \eta_{G_x T_x} \tau^0, \tau^0, \eta_{G_x T_x} \tau^0\}$. Here, τ^{zx} is to be read as $\tau^{zx} \equiv (\tau^z + \tau^x)/\sqrt{2}$.

PSG No.	\mathcal{W}_{T_1}	\mathcal{W}_{T_2}	\mathcal{W}_{σ_y}	\mathcal{W}_{σ_x}	$\mathcal{W}_{\sigma_{xy}}$	$\mathcal{W}_{\mathcal{T}}$
1(a)	τ^0	τ^0	τ^0	τ^0	τ^0	τ^0
1(b)	$i\tau^z$	$i\tau^z$	$i\tau^z$	$i\tau^z$	τ^0	τ^0
2(a)	τ^0	τ^0	τ^0	τ^0	τ^0	$i\tau^y$
2(b)	$i\tau^z$	$i\tau^z$	$i\tau^z$	$i\tau^z$	τ^0	$i\tau^y$
2(c)	$i\tau^y$	$i\tau^y$	$i\tau^y$	$i\tau^y$	τ^0	$i\tau^y$
3(a)	τ^0	τ^0	τ^0	τ^0	$i\tau^z$	$i\tau^y$
3(b)	$i\tau^z$	$i\tau^z$	$i\tau^z$	$i\tau^z$	$i\tau^z$	$i\tau^y$
3(c)	$i\tau^y$	$i\tau^y$	$i\tau^y$	$i\tau^y$	$i\tau^z$	$i\tau^y$
3(d)	$i\tau^x$	$i\tau^x$	$i\tau^x$	$i\tau^x$	$i\tau^z$	$i\tau^y$
3(e)	$i\tau^{zx}$	$i\tau^{z\bar{x}}$	$i\tau^{z\bar{x}}$	$i\tau^{zx}$	$i\tau^z$	$i\tau^y$
4(a)	τ^0	τ^0	τ^0	τ^0	$i\tau^z$	$i\tau^z$
4(b)	$i\tau^z$	$i\tau^z$	$i\tau^z$	$i\tau^z$	$i\tau^z$	$i\tau^z$
4(c)	$i\tau^y$	$i\tau^y$	$i\tau^y$	$i\tau^y$	$i\tau^z$	$i\tau^z$
5(a)	τ^0	τ^0	τ^0	τ^0	$i\tau^z$	τ^0
5(b)	$i\tau^z$	$i\tau^z$	$i\tau^z$	$i\tau^z$	$i\tau^z$	τ^0
5(c)	$i\tau^y$	$i\tau^y$	$i\tau^y$	$i\tau^y$	$i\tau^z$	τ^0
5(d)	$i\tau^{zx}$	$i\tau^{z\bar{x}}$	$i\tau^{z\bar{x}}$	$i\tau^{zx}$	$i\tau^z$	τ^0

PSG No.	\mathcal{W}_{σ_y}	\mathcal{W}_{σ_x}	$\mathcal{W}_{\sigma_{xy}}$	$\mathcal{W}_{\mathcal{T}}$	\mathcal{W}_{σ_y}	\mathcal{W}_{σ_x}	$\mathcal{W}_{\sigma_{xy}}$	$\mathcal{W}_{\mathcal{T}}$
1(a)	τ^0	τ^0	τ^0	τ^0	τ^0	τ^0	τ^0	τ^0
1(b)	$i\tau^z$	$i\tau^z$	τ^0	τ^0	$i\tau^z$	$i\tau^z$	τ^0	τ^0
2(a)	τ^0	τ^0	τ^0	$i\tau^y$	τ^0	τ^0	τ^0	$i\tau^z$
2(b)	$i\tau^z$	$i\tau^z$	τ^0	$i\tau^y$	$i\tau^x$	$i\tau^x$	τ^0	$i\tau^z$
2(c)	$i\tau^y$	$i\tau^y$	τ^0	$i\tau^y$	$i\tau^z$	$i\tau^z$	τ^0	$i\tau^z$
3(a)	τ^0	τ^0	$i\tau^z$	$i\tau^y$	τ^0	τ^0	$i\tau^x$	$i\tau^z$
3(b)	$i\tau^z$	$i\tau^z$	$i\tau^z$	$i\tau^y$	$i\tau^x$	$i\tau^x$	$i\tau^x$	$i\tau^z$
3(c)	$i\tau^y$	$i\tau^y$	$i\tau^z$	$i\tau^y$	$i\tau^z$	$i\tau^z$	$i\tau^x$	$i\tau^z$
3(d)	$i\tau^x$	$i\tau^x$	$i\tau^z$	$i\tau^y$	$i\tau^y$	$i\tau^y$	$i\tau^x$	$i\tau^z$
3(e)	$i\tau^{z\bar{x}}$	$i\tau^{zx}$	$i\tau^z$	$i\tau^y$	$i\tau^1$	$i\tau^y$	$i\tau^{xy}$	$i\tau^z$
4(a)	τ^0	τ^0	$i\tau^z$	$i\tau^z$	τ^0	τ^0	$i\tau^z$	$i\tau^z$
4(b)	$i\tau^z$	$i\tau^z$	$i\tau^z$	$i\tau^z$	$i\tau^z$	$i\tau^z$	$i\tau^z$	$i\tau^z$
4(c)	$i\tau^y$	$i\tau^y$	$i\tau^z$	$i\tau^z$	$i\tau^x$	$i\tau^x$	$i\tau^z$	$i\tau^z$
5(a)	τ^0	τ^0	$i\tau^z$	τ^0	τ^0	τ^0	$i\tau^z$	τ^0
5(b)	$i\tau^z$	$i\tau^z$	$i\tau^z$	τ^0	$i\tau^z$	$i\tau^z$	$i\tau^z$	τ^0
5(c)	$i\tau^y$	$i\tau^y$	$i\tau^z$	τ^0	$i\tau^x$	$i\tau^x$	$i\tau^z$	τ^0
5(d)	$i\tau^{z\bar{x}}$	$i\tau^{zx}$	$i\tau^z$	τ^0	$i\tau^1$	$i\tau^y$	$i\tau^{xy}$	τ^0

TABLE X. The same PSGs as enlisted in Table IX, but recast in terms of the symmetry group $\{T_1, T_2, \sigma_x, \sigma_y, \sigma_{xy}, \mathcal{T}\}$ [see Eqs. (D6)-(D11)]. $\tau^{z\bar{x}}$ is to be read as $\tau^{z\bar{x}} \equiv (\tau^z - \tau^x)/\sqrt{2}$.

$$\mathcal{W}_{T_2}(m, n, u) = \mathcal{W}_{T_2}, \quad (\text{D13})$$

$$\mathcal{W}_{\sigma_y}(m, n, u) = \{1, \eta_{G_x T_x}, \eta_{G_x T_x} \eta_{\sigma_x G_x}, \eta_{\sigma_x G_x}\} \mathcal{W}_{\sigma_y}, \quad (\text{D14})$$

$$\mathcal{W}_{\sigma_x}(m, n, u) = \{1, \eta_{\sigma_x G_x}, \eta_{G_x T_x} \eta_{\sigma_x G_x}, \eta_{G_x T_x}\} \mathcal{W}_{\sigma_x}, \quad (\text{D15})$$

TABLE XI. List of PSGs written in the square-lattice notation of Eq. (D24). We define $\tau^{xy} \equiv (\tau^x + \tau^y)/\sqrt{2}$ and $\tau^{x\bar{y}} \equiv (\tau^x - \tau^y)/\sqrt{2}$. On the right side, we present the solutions in a different gauge, which is the same as the one used in Ref. 55.

$$\mathcal{W}_{\sigma_{xy}}(m, n, u) = \{1, 1, \eta_\sigma, 1\} \mathcal{W}_{\sigma_{xy}}, \quad (\text{D16})$$

$$\mathcal{W}_{\mathcal{T}}(m, n, u) = \{1, \eta_{G_x \mathcal{T}}, 1, \eta_{G_x \mathcal{T}}\} \mathcal{W}_{\mathcal{T}}. \quad (\text{D17})$$

The square lattice, of course, has only one site per

unit cell, so the solutions above can be reformulated in the simple (x, y) coordinate system as

$$W_{T_1}(x, y) = \eta_\sigma^y \mathcal{W}_{T_1}, \quad (\text{D18})$$

$$W_{T_2}(x, y) = \mathcal{W}_{T_2}, \quad (\text{D19})$$

$$W_{\sigma_y}(x, y) = \eta_{G_x T_x}^x \eta_{\sigma_x G_x}^y \mathcal{W}_{\sigma_y}, \quad (\text{D20})$$

$$W_{\sigma_x}(x, y) = \eta_{\sigma_x G_x}^x \eta_{G_x T_x}^y \mathcal{W}_{\sigma_x}, \quad (\text{D21})$$

$$W_{\sigma_{xy}}(x, y) = \eta_\sigma^{xy} \mathcal{W}_{\sigma_{xy}}, \quad (\text{D22})$$

$$W_{\mathcal{T}}(x, y) = \eta_{G_x \mathcal{T}}^{x+y} \mathcal{W}_{\mathcal{T}}. \quad (\text{D23})$$

Additionally, one can conveniently set $\mathcal{W}_{T_1} = \mathcal{W}_{T_2} = \tau^0$ by applying a gauge transformation of the form $W(x, y) = \mathcal{W}_{T_2}^y \mathcal{W}_{T_1}^x$. This will not change the overall structure of the solutions in Table X up to a sign factor, which can be absorbed either using the gauge freedom (if it is global) or by redefining the parameters η . As an example, for $\mathcal{W}_{T_1} = i\tau^{zx} = i(\tau^z + \tau^1)/\sqrt{2}$, $W_{T_1}(x, y)$ and $W_{\sigma_{xy}}(x, y)$ in Eqs. (D18) and (D22), respectively, become $\mathcal{W}_{T_1} = (-\eta_\sigma)^y$ and $W_{\sigma_{xy}}(x, y) = (-\eta_\sigma)^{xy} \mathcal{W}_{\sigma_{xy}}$. The original x, y dependence can be recovered by the redefinition $\eta_\sigma \rightarrow -\eta_\sigma$.

After all these steps, we arrive at the full solution for the square-lattice PSGs, which read

$$W_{T_1}(x, y) = \eta_\sigma^y, \quad (\text{D24a})$$

$$W_{T_2}(x, y) = \tau^0, \quad (\text{D24b})$$

$$W_{\sigma_y}(x, y) = \eta_{G_x T_x}^x \eta_{\sigma_x G_x}^y \mathcal{W}_{\sigma_y}, \quad (\text{D24c})$$

$$W_{\sigma_x}(x, y) = \eta_{\sigma_x G_x}^x \eta_{G_x T_x}^y \mathcal{W}_{\sigma_x}, \quad (\text{D24d})$$

$$W_{\sigma_{xy}}(x, y) = \eta_\sigma^{xy} \mathcal{W}_{\sigma_{xy}}, \quad (\text{D24e})$$

$$W_{\mathcal{T}}(x, y) = \eta_{G_x \mathcal{T}}^{x+y} \mathcal{W}_{\mathcal{T}}, \quad (\text{D24f})$$

with the \mathcal{W} matrices noted on the left side in Table XI. On the right side of the same table, we write these matrices in a different gauge, used in Ref. 55. This completes the mapping of projective realizations of the symmetries from the Shastry-Sutherland model to those of the square lattice.

Appendix E: Properties of U(1) and \mathbb{Z}_2 *Ansätze*

The properties of an *Ansatz*—such as its spinon excitation spectrum, the dynamical structure factor, and the equal-time structure factor—depend on the choices of the mean-field parameters, which, in principle, should be evaluated self-consistently based on specific models. Here, we take a different approach and concentrate on more generic properties rather than focusing on a particular model.

In the canonical gauge, any U(1) *Ansatz* consists of solely hopping terms, so the pseudospin \uparrow and \downarrow sectors are decoupled. Working in the basis defined by $\hat{f}_{\mathbf{k},\alpha} =$

$(\hat{f}_{\mathbf{k},1,\alpha}, \hat{f}_{\mathbf{k},2,\alpha}, \hat{f}_{\mathbf{k},3,\alpha}, \hat{f}_{\mathbf{k},4,\alpha})^T$, the quadratic Hamiltonian in \mathbf{k} -space reads

$$\hat{H}(\mathbf{k}) = \sum_{\alpha=\uparrow,\downarrow} \hat{f}_{\mathbf{k},\alpha}^\dagger \hat{H}_{\mathbf{k}}^{\text{U}(1)} \hat{f}_{\mathbf{k},\alpha}. \quad (\text{E1})$$

Owing to spinon number conservation, the chemical potential does not need to be explicitly considered and can be ignored here. The one-particle-per-site constraint (on average) is enforced by setting the Fermi energy such that we are at half filling.

In the following, we summarize the generic spinon excitation characteristics of different U(1) *Ansätze*, which are illustrated in the top panel of Fig. 13. The band structures are plotted along the path $\Gamma \rightarrow X \rightarrow M \rightarrow \Gamma$, where the high-symmetry points are $\Gamma(0, 0)$, $X(\pi/2, 0)$, and $M(\pi/2, \pi/2)$ in the first Brillouin zone.

- The excitation spectrum for U100 is quadratic and gapless at the Γ point, while U1 π 0 exhibits quadratic gapless excitations at isolated \mathbf{k} -points. The spectrum of U10 π consists of Dirac cones located at $(\pm\pi/2, \pm\pi/2)$, as also seen for the SU(2) Dirac spin liquid labeled as SU2B n 0 on the square lattice [55]. U1 $\pi\pi$ features a Fermi surface with linear gapless excitations along $(k_x, -k_x)$ and $(k_x, k_x \pm \pi/2)$, forming Dirac nodal lines.
- The spectrum of U300 is gapless with a linear dispersion, and Dirac cones are observed along the \overline{XM} and \overline{YM} lines. A Fermi surface is seen for $\chi_d < 1.5\chi_s$. U3 π 0 has a gapped spinon spectrum. The link fields of U30 π and U3 $\pi\pi$ are the same as those of U10 π and U1 $\pi\pi$, respectively. However, the former states include a staggered chemical potential that opens up a gap. Notably, the staggered chemical potential also opens a gap for U300.
- The excitation spectrum of U500 is quadratic and gapless along $(k_x, \pm k_x)$, forming nodal lines. For U50 π , the spectrum is also gapless but linearly dispersing, forming a Dirac nodal loop surrounding the Γ or M point.
- The U8 ξ 0 family encompasses a series of *Ansätze* corresponding to different choices of $\xi = \mathcal{P}\pi/\mathcal{Q}$, for $\mathcal{P}, \mathcal{Q} \in \mathbb{Z}$. Here, we limit our analysis to states realizable within a single unit cell, which includes $\xi = 0$ and $\xi = \pi$. Both cases exhibit a Dirac dispersion. For $\xi = 0$, the Dirac cones are anchored at the Γ point, while for $\xi = \pi$, they reside at all high-symmetry points.

Next, we discuss the excitation spectra of the \mathbb{Z}_2 *Ansätze*. In this case, the interpretation of the quasiparticles is quite different from that for a U(1) IGG because spinon number conservation is lost due to the presence of pairing terms. We begin with the generic Bogoliubov–de Gennes (BdG) basis

$$\hat{\Psi}_{\mathbf{k}}^\dagger = (\hat{f}_{\mathbf{k},\uparrow}^\dagger, (\hat{f}_{-\mathbf{k},\downarrow})^T), \quad (\text{E2})$$

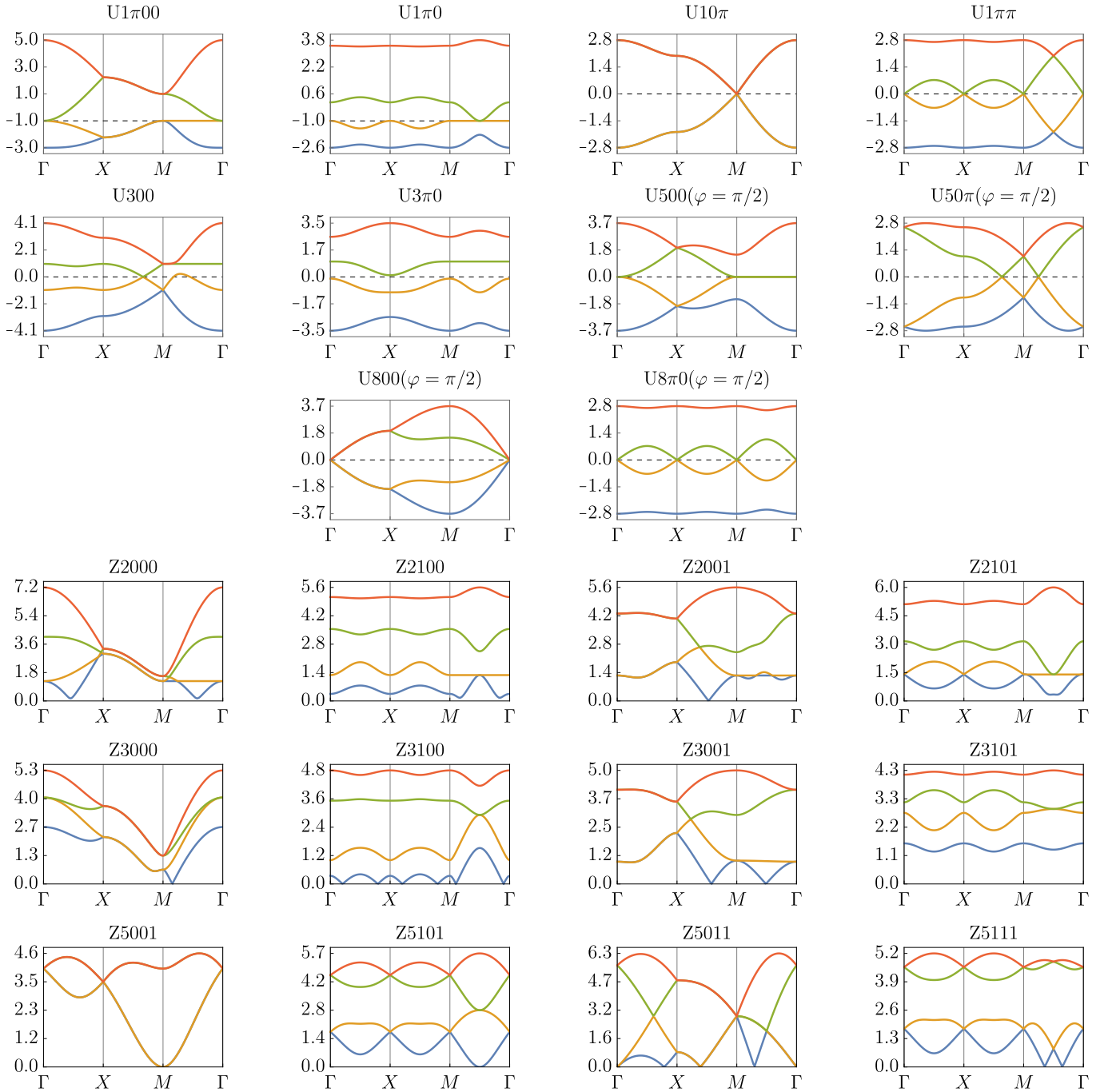


FIG. 13. Spinon band structures for all the U(1) *Ansätze* illustrated in Fig. 3 (top), and for the \mathbb{Z}_2 *Ansätze* listed in Table III (bottom). In both cases, we pick the mean-field parameters such that the magnitude of the symmetry-allowed hoppings is set to one. The dashed black line marks the Fermi level. For the U(1) *Ansätze* with both imaginary and real hoppings, we define a parameter $\varphi = \text{Arg}[u_s^4]$, which is related to the flux threading the square plaquettes (see Fig. 3).

using which, any general mean-field Hamiltonian in \mathbf{k} -space can be expressed as

$$\hat{H}(\mathbf{k}) = \hat{\Psi}_{\mathbf{k}}^\dagger \hat{H}_{\mathbf{k}}^{\text{BdG}} \hat{\Psi}_{\mathbf{k}}; \quad \hat{H}_{\mathbf{k}}^{\text{BdG}} = \begin{bmatrix} \hat{H}_{\mathbf{k}}^{\text{U}(1)} & \hat{H}_{\mathbf{k}}^{\mathbb{Z}_2} \\ (\hat{H}_{\mathbf{k}}^{\mathbb{Z}_2})^\dagger & -\hat{H}_{-\mathbf{k}}^{\text{U}(1)} \end{bmatrix}, \quad (\text{E3})$$

where $\hat{H}_{\mathbf{k}}^{\text{U}(1)}$ and $\hat{H}_{\mathbf{k}}^{\mathbb{Z}_2}$ denote the hopping and pairing terms in the *Ansatz*, respectively. The superscript \mathbb{Z}_2 indicates that these terms are the ones responsible for breaking the IGG down to \mathbb{Z}_2 .

Upon diagonalization, $\hat{H}_{\mathbf{k}}^{\text{BdG}}$ yields eigenvalues in positive and negative pairs, i.e., $\pm\epsilon_{\mathbf{k},u}$. In the diagonalized

basis, $\hat{f}_{\mathbf{k},u,\alpha} \rightarrow \hat{\zeta}_{\mathbf{k},u,\alpha}$, the Hamiltonian can be rewritten as

$$\begin{aligned} \hat{H}(\mathbf{k}) &= \sum_{u=1}^4 \epsilon_{\mathbf{k},u} (\hat{\zeta}_{\mathbf{k},u,\uparrow}^\dagger \hat{\zeta}_{\mathbf{k},u,\uparrow} - \hat{\zeta}_{\mathbf{k},u,\downarrow} \hat{\zeta}_{\mathbf{k},u,\downarrow}^\dagger) \\ &= \sum_{u=1}^4 \sum_{\alpha=\uparrow,\downarrow} \epsilon_{\mathbf{k},u} (\hat{\zeta}_{\mathbf{k},u,\alpha}^\dagger \hat{\zeta}_{\mathbf{k},u,\alpha} - 1). \end{aligned} \quad (\text{E4})$$

This formulation allows us to interpret the spinon excitations of a generic symmetric \mathbb{Z}_2 mean-field *Ansatz* as Bogoliubov quasiparticles that always have a positive energy. In other words, the Fermi level lies at zero energy, leaving the quasiparticle-free ground state as the vacuum. In this case, the explicit inclusion of Lagrange multipliers is required to enforce the one-particle-per-site constraint on average.

In the second half of Fig. 13, we showcase the spinon dispersion spectra for the \mathbb{Z}_2 *Ansätze* listed in Table III. For purposes of illustration, all mean-field parameters are set to unity. The general properties of these states are as follows:

- For Z2000, the chemical potential $\mu \neq 0$ (required to satisfy the constraint) opens up a small gap in general. Both Z2100 and Z2101 are also generically gapped. The spectrum of Z2001 always exhibits a Dirac dispersion with a Dirac cone positioned between the X and M points.
- Similarly to Z2001, Z3000 hosts a Dirac dispersion, with a Dirac cone located between Γ and M . Z3100 shows a gapless spectrum with either a Fermi surface or Dirac cones, depending on the mean-field parameters. The spectrum of Z3001 generally features a Fermi surface surrounding the M points, or a Dirac dispersion for specific parameter choices. Z3101 can exhibit gapped, Dirac, or Fermi-surface states.
- Within the Z5 class, Z5101, Z5011, and Z5111 exhibit gapless dispersions with a Fermi surface, while Z5001 has a quadratic dispersion that becomes gapless at the M point.
- For the remaining six *Ansätze* (Z2011, Z2111, Z3010, Z3110, Z3011, Z3111), the term breaking the IGG from U(1) to \mathbb{Z}_2 is the onsite piece $\mu\tau^z$. The link fields retain the original U(1) flux structures, leading these *Ansätze* to qualitatively resemble their parent U(1) states.

To distinguish between and further characterize these states, we can calculate their respective structure factors, which are also of utility for comparisons to neutron scattering experiments. The longitudinal component (which suffices due to spin-rotation symmetry) of the equal-time spin-spin correlation defines the equal-time spin structure

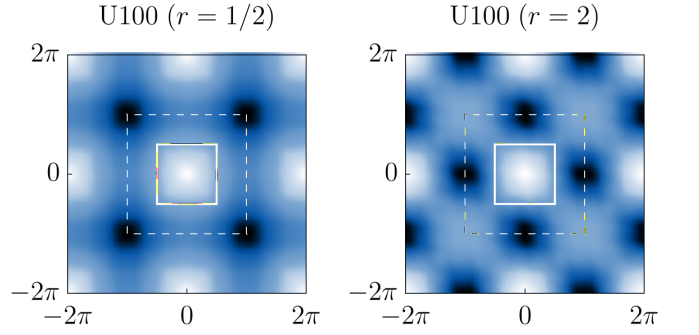


FIG. 14. Equal-time structure factor for the U100 state. r denotes the ratio of the hopping amplitude on the diagonals to that on the square bonds. Note that the structure factors for $r = 1/2$ and $r = 2$ show the same signatures as Néel and stripe magnetic ordering on the square lattice, respectively. This property holds for all the U(1) and \mathbb{Z}_2 *Ansätze* with nonvanishing parameters on both the square and diagonal bonds. The solid (dashed) white square marks the first (extended) Brillouin zone.

factor as

$$\mathcal{S}(\mathbf{q}) = \frac{1}{\mathcal{N}} \sum_{i,j} e^{i\mathbf{q}\cdot\mathbf{r}_{ij}} \langle \hat{S}_i^z \hat{S}_j^z \rangle, \quad (\text{E5})$$

where $\sqrt{\mathcal{N}}$ is the number of lattice sites. In Fig. 14, we show the equal-time structure factor of the U(1) state labeled U100 for two choices of parameters: $r = 1/2$ and $r = 2$, where r is the ratio of mean-field amplitudes on the diagonal and square bonds. With stronger square bonds, maxima appear at the $M'(\pi, \pi)$ points in the extended Brillouin zone (EBZ), while for dominant diagonal bonds, the maxima occur at $X'(\pi, 0)$. These maxima are not sharp Bragg peaks due to spin-rotational symmetry but instead form a continuum. This qualitative behavior persists across all U(1) and \mathbb{Z}_2 *Ansätze* with nonzero mean-field parameters on both square and diagonal bonds. For *Ansätze* with vanishing diagonal parameters, the maxima always appear at M' .

For representative parameter choices (consistent with the dispersion plots in Fig. 13), the equal-time structure factors of all the U(1) and \mathbb{Z}_2 *Ansätze* are shown in Fig. 15. While most states exhibit minimal qualitative differences in their equal-time structure factor, the distinctions are clearer in the dynamical structure factor (DSF), defined as

$$\mathcal{S}(\mathbf{q}, \omega) = \int_{-\infty}^{+\infty} \frac{d\tau e^{i\omega\tau}}{2\pi\mathcal{N}} \sum_{i,j} e^{i\mathbf{q}\cdot\mathbf{r}_{ij}} \langle \hat{S}_i^z(\tau) \hat{S}_j^z(0) \rangle. \quad (\text{E6})$$

The DSFs are plotted for the various *Ansätze* along the high-symmetry path $\Gamma(0,0) \rightarrow X'(\pi,0) \rightarrow M'(\pi,\pi) \rightarrow \Gamma$ in the EBZ in Fig. 16.

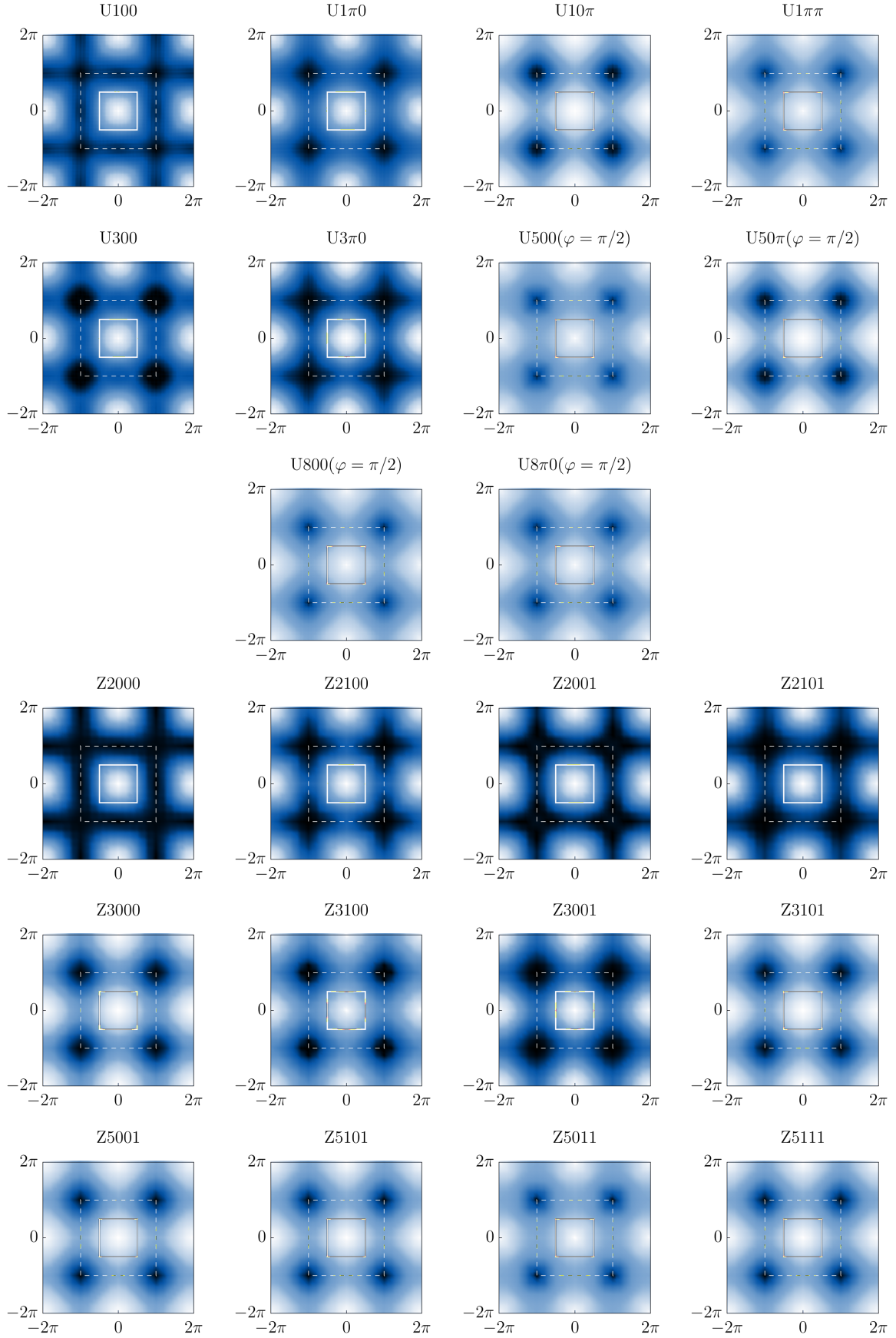


FIG. 15. Equal-time structure factors for all the $U(1)$ *Ansätze* illustrated in Fig. 3 (top), and for the Z_2 *Ansätze* listed in Table III (bottom), following the same conventions for the color map as in Fig. 14. The mean-field parameters are the same as those used for Fig. 13.

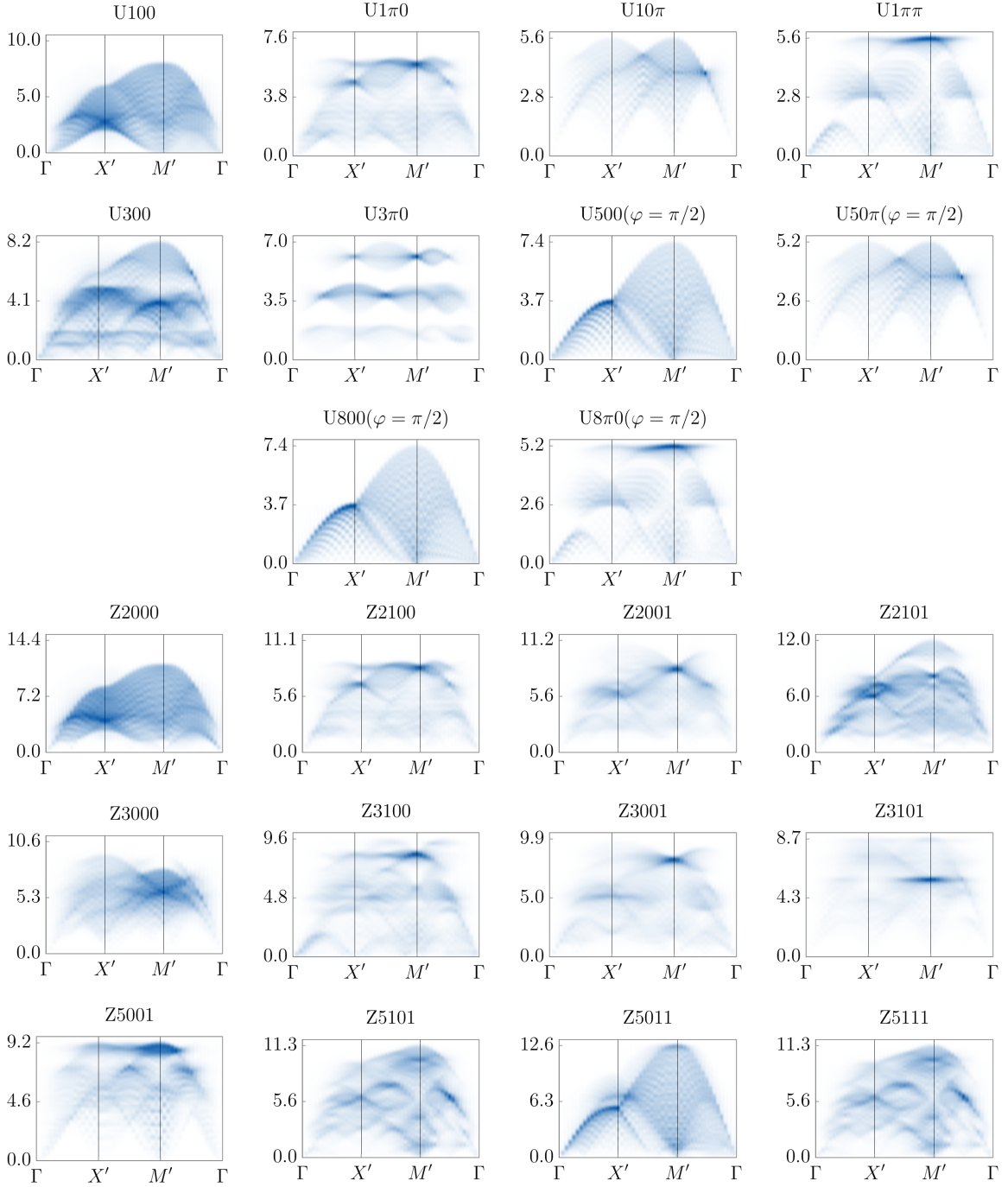


FIG. 16. Dynamical structure factors for all the U(1) *Ansätze* illustrated in Fig. 3 (top), and for the Z_2 *Ansätze* listed in Table III (bottom). The variation in intensity from low to high is conveyed by the gradient of the color, from white to blue (similar to Fig. 12). The mean-field parameters are the same as those used for Fig. 13.

Appendix F: Lattice-nematic QSLs

So far, we have focused exclusively on symmetric QSLs in our discussion. However, with the aim of describing the dimerizations of our fully symmetric QSLs into the neighboring plaquette VBC phase reported for $J_s/J_d \lesssim 0.77$ [43, 46], we now also perform a classifica-

tion of lattice-nematic QSLs which have a lower symmetry, namely, that of the plaquette VBC. This enables us to identify the possible fermionic mean-field states that lead to a plaquette VBC phase upon transitioning out of the spin liquid.

Realizing a plaquette VBC on the empty squares of the Shastry-Sutherland lattice (as observed in numerical

Label	$\{\eta_y, \eta_{C_4}, \eta_{C_4y}, \eta_{\mathcal{T}}, \eta_{\mathcal{T}C_4}\}$	u_s	u'_s	u_d	Onsite
P1A/B	$\{\eta_y, +, +, +, +\}$	$\tau^{z,x}$	$\tau^{z,x}$	$\tau^{z,x}$	τ^z
P2A/B	$\{\eta_y, +, -, +, +\}$	$\tau^{z,x}$	$\tau^{z,x}$	0	τ^z
P3A/B	$\{\eta_y, -, +, +, +\}$	$\tau^{z,x}$	$\tau^{z,x}$	0	τ^z
P4A/B	$\{\eta_y, -, -, +, +\}$	$\tau^{z,x}$	$\tau^{z,x}$	$\tau^{z,x}$	τ^z
P5A/B	$\{\eta_y, +, +, +, -\}$	$\tau^{0,y}$	$\tau^{0,y}$	$\tau^{z,x}$	τ^z
P6A/B	$\{\eta_y, +, -, +, -\}$	$\tau^{0,y}$	$\tau^{0,y}$	0	τ^z
P7A/B	$\{\eta_y, -, +, +, -\}$	$\tau^{0,y}$	$\tau^{0,y}$	0	τ^z
P8A/B	$\{\eta_y, -, -, +, -\}$	$\tau^{0,y}$	$\tau^{0,y}$	$\tau^{z,x}$	τ^3
P9A/B	$\{\eta_y, +, +, -, +\}$	$\tau^{z,x}$	$\tau^{0,y}$	τ^y	τ^z
P10A/B	$\{\eta_y, +, -, -, +\}$	$\tau^{z,x}$	$\tau^{0,y}$	τ^0	τ^z
P11A/B	$\{\eta_y, -, +, -, +\}$	$\tau^{z,x}$	$\tau^{0,y}$	τ^0	τ^z
P12A/B	$\{\eta_y, -, -, -, +\}$	$\tau^{z,x}$	$\tau^{0,y}$	τ^y	τ^z
P13A/B	$\{\eta_y, +, +, -, -\}$	$\tau^{0,y}$	$\tau^{z,x}$	τ^y	τ^z
P14A/B	$\{\eta_y, +, -, -, -\}$	$\tau^{0,y}$	$\tau^{z,x}$	τ^0	τ^z
P15A/B	$\{\eta_y, -, +, -, -\}$	$\tau^{0,y}$	$\tau^{z,x}$	τ^0	τ^z
P16A/B	$\{\eta_y, -, -, -, -\}$	$\tau^{0,y}$	$\tau^{3,1}$	τ^y	τ^z
P17A/B	$\{\eta_y, +, +, +, -\}$	$\tau^{0,z}$	$\tau^{0,x,z}$	0	0
P18A/B	$\{\eta_y, +, -, +, -\}$	$\tau^{0,z}$	$\tau^{0,x,z}$	0	0
P19A/B	$\{\eta_y, -, +, +, -\}$	$\tau^{0,z}$	$\tau^{0,x,z}$	0	0
P20A/B	$\{\eta_y, -, -, +, -\}$	$\tau^{0,z}$	$\tau^{0,x,z}$	0	0
P21A/B	$\{\eta_y, +, +, -, +\}$	0	$\tau^{0,z}$	$\tau^{x,z}$	0
P22A/B	$\{\eta_y, +, -, -, +\}$	0	$\tau^{0,z}$	τ^0	0
P23A/B	$\{\eta_y, -, +, -, +\}$	0	$\tau^{0,z}$	τ^0	0
P24A/B	$\{\eta_y, -, -, -, +\}$	0	$\tau^{0,z}$	$\tau^{x,z}$	0
P25A/B	$\{\eta_y, +, +, -, -\}$	$\tau^{0,z}$	0	$\tau^{x,z}$	0
P26A/B	$\{\eta_y, +, -, -, -\}$	$\tau^{0,z}$	0	τ^0	0
P27A/B	$\{\eta_y, -, +, -, -\}$	$\tau^{0,z}$	0	τ^0	0
P28A/B	$\{\eta_y, -, -, -, -\}$	$\tau^{0,z}$	0	$\tau^{x,z}$	0

TABLE XII. Mean-field parameters on the reference bonds, u_s , u'_s , and u_d for all possible *Ansätze* taking only translations, C_4 , and time-reversal symmetries into account. Each row stands for two *Ansätze* labeled by classes A ($\eta_y = +1$) and B ($\eta_y = -1$). All the *Ansätze* besides P22A, P22B, P23A, P23B, P26A, P26B, P27A, and P27B correspond to a \mathbb{Z}_2 IGG.

studies) imprints a different symmetry group on the system: this order requires breaking both G_x and σ_{xy} , but preserving the fourfold rotational, C_4 , symmetry. Hence, the modified symmetry group is given by $\{T_x, T_y, C_4, \mathcal{T}\}$. The symmetry relations analogous to Eqs. (18) are

$$T_x^{-1} T_y^{-1} T_x T_y = \mathbb{1}, \quad (\text{F1})$$

$$T_y C_4^{-1} T_x C_4 = \mathbb{1}, \quad (\text{F2})$$

$$T_x^{-1} C_4^{-1} T_y C_4 = \mathbb{1}, \quad (\text{F3})$$

$$C_4^4 = \mathcal{T}^2 = \mathbb{1}, \quad (\text{F4})$$

$$\mathcal{T} \mathcal{O} \mathcal{T}^{-1} \mathcal{O}^{-1} = \mathbb{1}. \quad (\text{F5})$$

For concreteness, we consider the center of an empty square (which the C_4 axis passes through) as the origin of the coordinate system, and the square itself is taken to be

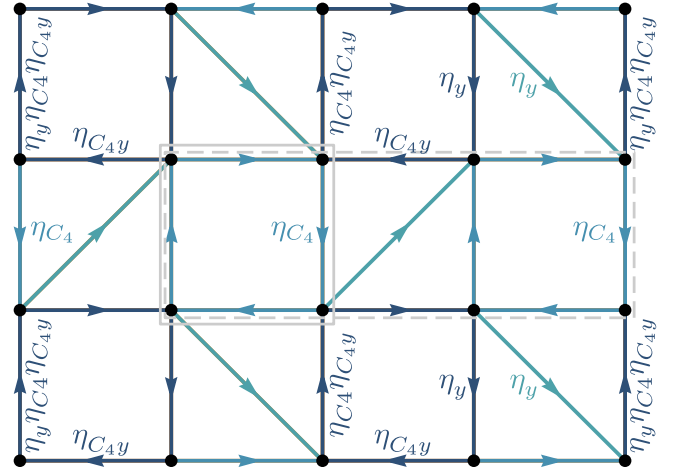


FIG. 17. Representation of \mathbb{Z}_2 *Ansätze* with the symmetry group of the plaquette VBC. The link fields on the light blue, dark blue, and teal (diagonal) bonds are given by $u_s = i\chi_s^0 \tau^0 + \Delta_s^1 \tau^x + \Delta_s^2 \tau^y + \chi_s^3 \tau^z$, $u'_s = i\chi'_s \tau^0 + \Delta'_s \tau^x + \Delta'_s \tau^y + \chi'_s \tau^z$, and $u_d = i\chi_d \tau^0 + \Delta_d \tau^x + \Delta_d \tau^y + \chi_d \tau^z$, respectively. The allowed mean fields for the 48 different \mathbb{Z}_2 *Ansätze* can be read off Table XII. The solid (dashed) gray box marks the unit cell required to realize *Ansätze* in class A, with $\eta_y = +1$ (class B, with $\eta_y = -1$).

the new reference unit cell; see Fig. 17. The coordinates of the four sites (indexed by u) within the unit cell are given by $1(-a/2, a/2)$, $2(-a/2, -a/2)$, $3(a/2, -a/2)$, and $4(a/2, a/2)$. Now, we introduce the sublattice-dependent coordinate system (X, Y, u) , akin to Eq. (15) earlier. Under the present symmetry group elements, (X, Y, u) transforms as

$$T_x : (X, Y, u) \rightarrow (X + 1, Y, u), \quad (\text{F6})$$

$$T_y : (X, Y, u) \rightarrow (X, Y + 1, u), \quad (\text{F7})$$

$$C_4 : (X, Y, u) \rightarrow (-Y, X, C_4(u)), \quad (\text{F8})$$

where $C_4(\{1, 2, 3, 4\}) = \{2, 3, 4, 1\}$.

Following the same prescription as in Appendix C, we can obtain the solutions of the algebraic PSGs:

$$W_{T_x}(X, Y, u) = \eta_y^Y \tau^0, \quad W_{T_y}(X, Y, u) = \tau^0, \quad (\text{F9})$$

$$W_{C_4}(X, Y, u) = \eta_{C_4y}^Y \eta_y^{XY} \mathcal{W}_{C_4, u}, \quad (\text{F10})$$

$$W_{\mathcal{T}}(X, Y, u) = \eta_{\mathcal{T}}^{X+Y} \eta_{\mathcal{T}C_4}^u \mathcal{W}_{\mathcal{T}}. \quad (\text{F11})$$

Here, $\mathcal{W}_{C_4, u} = \{\tau^0, \tau^0, \tau^0, \eta_{C_4} \tau^0\}$, and the matrix $\mathcal{W}_{\mathcal{T}}$ can be either τ^0 or $i\tau^y$. Each of the five parameters $\{\eta_y, \eta_{C_4}, \eta_{C_4y}, \eta_{\mathcal{T}}, \eta_{\mathcal{T}C_4}\}$ take values ± 1 , so together with the two options for $\mathcal{W}_{\mathcal{T}}$, we find a total of 64 algebraic PSGs. However, for $\mathcal{W}_{\mathcal{T}} = \tau^0$, the solution with $\eta_{\mathcal{T}} = \eta_{\mathcal{T}C_4} = +1$ has to be excluded as the mean-field parameters trivially vanish on all the bonds. Therefore, we are left with 56 PSGs. The corresponding symmetry-allowed mean-field parameters are documented in Table XII. Note that since we restrict ourselves to short-range *Ansätze* with only NN and NNN bonds, only 48 of

the 56 PSGs lead to QSL states with IGG \mathbb{Z}_2 . The remaining eight (P22A, P22B, P23A, P23B, P26A, P26B, P27A and P27B) carry a U(1) IGG since the pairing terms identically vanish up to NNNs. In Table XII, each row corresponds to two *Ansätze*, one with $\eta_y = +1$ (class A) and the other with $\eta_y = -1$ (class B). Realization of the class-B *Ansätze* requires doubling of the unit cell along the x -axis. The detailed sign structures of these *Ansätze* are illustrated in Fig. 17.

Besides this PSG classification, let us briefly comment on the energetics of these nematic QSLs. At $J_s/J_d = 0.70$, our Gutzwiller-projected VMC calculations optimizing the symmetry-inequivalent hoppings and pairings within a unit cell [126–129] find that the lowest-energy states are those for which the fluxes through one type of empty squares (formed by either dark blue or light blue bonds in Fig. 17) settle to a value of π , while the fluxes threading the other type of empty squares and the squares hosting diagonal bonds converge to zero. Those with π fluxes are also found to have substantially larger spin-spin correlations on the square-lattice bonds, thereby forming plaquette singlets, whereas the correlations on the bonds of the zero-flux squares are essentially vanishing. Multiple *Ansätze* are found to optimize to this particular flux and dimerization pattern; all of these yield extremely close energies such that we are unable to uniquely identify a single lowest-energy PSG to within our numerical accuracy.

Appendix G: Parent U(1) states for Z3000

As mentioned in Sec. IV A, the Z3000 *Ansatz* can be obtained by starting from three *distinct* U(1) states, namely, U100, U300 and U800, and breaking down the U(1) IGG to \mathbb{Z}_2 via singlet pairing terms. While we earlier focused on the viewpoint that the Z3000 state is a descendant of U100, here, for completeness, we illustrate how both U300 and U800 can equivalently be regarded as the parent state instead.

This is easier to see first for U800. Concretely, the

connection of U800 to Z3000 can be found by setting the mean-field parameters on all the diagonal bonds in Z3000 to zero, followed by an appropriate gauge transform. In the hopping-only gauge, the U800 state exhibits a Dirac cone anchored at the Γ point (see Fig. 13).

The U300 *Ansatz* has a nontrivial sign structure. Considering all the diagonals, this is given by

$$\begin{aligned} u_{12} &= u_{43} = u_{21} = u_{34} = u_{14} = u_{23} = u_{41} = u_{32} = \chi_s \tau^z, \\ u_{13} &= -u_{42} = \chi_d \tau^z, \quad u_{d_1} = -u_{d_2} = \chi_{d'} \tau^z, \\ u_{d_3} &= -u_{d_4} = u_{d_5} = -u_{d_6} = \chi_{\square} \tau^z, \\ \sum_{\gamma} a_{\gamma}(m, n, u) \tau^{\gamma} &= (-)^u \mu \tau^z. \end{aligned} \quad (\text{G1})$$

At first glance, the connection to Z3000 is therefore far from apparent. However, this can be established by setting $\chi_s = 0$ and $\Delta_{\square} = 0$ in the Z3000 *Ansatz*, followed by a gauge transformation of the form

$$W(m, n, u) = (-1)^{(\delta_{u,1} + \delta_{u,2})} (i\tau^y)^{(\delta_{u,2} + \delta_{u,4})}.$$

The dispersion of the U3000 state is sketched in Fig. 18(a), and features clear Fermi surfaces as evidenced by Fig. 18(b).

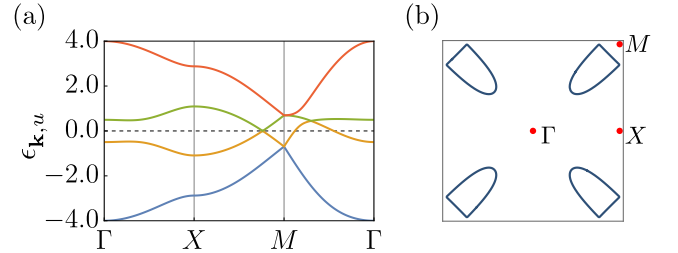


FIG. 18. (a) Dispersion of the U300 state, and (b) illustration of its Fermi surfaces. The mean-field parameters here are set to $\chi_s = 1.0$, $\chi_d = 0.5$, $\chi_{d'} = 0.4$, and $\chi_{\square} = 0.3$. The dashed line indicates the Fermi level.

- [1] B. Sriram Shastry and B. Sutherland, Exact ground state of a quantum mechanical antiferromagnet, *Physica B+C* **108**, 1069 (1981).
- [2] H. Kageyama, K. Yoshimura, R. Stern, N. V. Mushnikov, K. Onizuka, M. Kato, K. Kosuge, C. P. Slichter, T. Goto, and Y. Ueda, Exact Dimer Ground State and Quantized Magnetization Plateaus in the Two-Dimensional Spin System $\text{SrCu}_2(\text{BO}_3)_2$, *Phys. Rev. Lett.* **82**, 3168 (1999).
- [3] S. Miyahara and K. Ueda, Theory of the orthogonal dimer Heisenberg spin model for $\text{SrCu}_2(\text{BO}_3)_2$, *J. Phys.: Condens. Matter* **15**, R327 (2003).
- [4] P. C. G. Vlaar and P. Corboz, Tensor network study

- of the Shastry-Sutherland model with weak interlayer coupling, *SciPost Phys.* **15**, 126 (2023).
- [5] F. Ferrari and R. Valentí, Altermagnetism on the Shastry-Sutherland lattice, *Phys. Rev. B* **110**, 205140 (2024).
- [6] Q. Ma, B. R. Billingsley, M. Marshall, D. A. Dahlbom, Y. Hao, D. M. Pajerowski, A. I. Kolesnikov, X. Bai, C. D. Batista, T. Kong, and H. Cao, Quantum entanglement of XY-type spin dimers in Shastry-Sutherland lattice (2024), [arXiv:2412.17913](https://arxiv.org/abs/2412.17913) [cond-mat.str-el].
- [7] N. Li, A. Brassington, M. F. Shu, Y. Y. Wang, H. Liang, Q. J. Li, X. Zhao, P. J. Baker, H. Kikuchi, T. Masuda, G. Duan, C. Liu, H. Wang, W. Xie, R. Zhong, J. Ma,

- R. Yu, H. D. Zhou, and X. F. Sun, Spinons in a new Shastry-Sutherland lattice magnet $\text{Pr}_2\text{Ga}_2\text{BeO}_7$ (2024), [arXiv:2405.13628 \[cond-mat.str-el\]](#).
- [8] A. Liu, F. Song, Y. Cao, H. Ge, H. Bu, J. Zhou, Y. Qin, Q. Zeng, J. Li, L. Ling, W. Tong, J. Sheng, M. Yang, L. Wu, H. Guo, and Z. Tian, Distinct magnetic ground states in Shastry-Sutherland lattice materials: $\text{Pr}_2\text{Be}_2\text{GeO}_7$ versus $\text{Nd}_2\text{Be}_2\text{GeO}_7$, *Phys. Rev. B* **109**, 184413 (2024).
- [9] M. Pula, S. Sharma, J. Gautreau, S. K. P., A. Kanigel, M. D. Frontzek, T. N. Dolling, L. Clark, S. Dunsiger, A. Ghara, and G. M. Luke, Candidate for a quantum spin liquid ground state in the Shastry-Sutherland lattice material $\text{Yb}_2\text{Be}_2\text{GeO}_7$, *Phys. Rev. B* **110**, 014412 (2024).
- [10] A. Brassington, Q. Ma, G. Sala, A. I. Kolesnikov, K. M. Taddei, Y. Wu, E. S. Choi, H. Wang, W. Xie, J. Ma, H. D. Zhou, and A. A. Aczel, Magnetic properties of the quasi-XY Shastry-Sutherland magnet $\text{Er}_2\text{Be}_2\text{SiO}_7$ (2024), [arXiv:2405.08230 \[cond-mat.str-el\]](#).
- [11] L. Yadav, A. Rufino, R. Bag, C. dela Cruz, A. I. Kolesnikov, V. O. Garlea, D. Graf, F. Mila, and S. Haravifard, Observation of unprecedented fractional magnetization plateaus in a new Shastry-Sutherland Ising compound (2024), [arXiv:2405.12405 \[cond-mat.str-el\]](#).
- [12] M. Pula, S. Sharma, J. Gautreau, S. K. P., A. Kanigel, C. R. dela Cruz, T. N. Dolling, L. Clark, and G. M. Luke, Fractionalized Magnetization Plateaus in the Shastry-Sutherland Lattice Material $\text{Er}_2\text{Be}_2\text{GeO}_7$ (2024), [arXiv:2412.04360 \[cond-mat.str-el\]](#).
- [13] S. Miyahara and K. Ueda, Exact Dimer Ground State of the Two Dimensional Heisenberg Spin System $\text{SrCu}_2(\text{BO}_3)_2$, *Phys. Rev. Lett.* **82**, 3701 (1999).
- [14] Z. Weihong, C. J. Hamer, and J. Oitmaa, Series expansions for a Heisenberg antiferromagnetic model for $\text{SrCu}_2(\text{BO}_3)_2$, *Phys. Rev. B* **60**, 6608 (1999).
- [15] E. Müller-Hartmann, R. R. P. Singh, C. Knetter, and G. S. Uhrig, Exact Demonstration of Magnetization Plateaus and First-Order Dimer-Néel Phase Transitions in a Modified Shastry-Sutherland Model for $\text{SrCu}_2(\text{BO}_3)_2$, *Phys. Rev. Lett.* **84**, 1808 (2000).
- [16] M. Albrecht and F. Mila, First-order transition between magnetic order and valence bond order in a 2D frustrated Heisenberg model, *Europhys. Lett.* **34**, 145 (1996).
- [17] T. Munehisa and Y. Munehisa, Numerical Study of Excited States in the Shastry-Sutherland Model, *J. Phys. Soc. Jpn.* **72**, 160 (2003).
- [18] T. Munehisa and Y. Munehisa, The Stochastic State Selection Method for Energy Eigenvalues in the Shastry-Sutherland Model, *J. Phys. Soc. Jpn.* **73**, 340 (2004).
- [19] R. Darradi, J. Richter, and D. J. J. Farnell, Coupled cluster treatment of the Shastry-Sutherland antiferromagnet, *Phys. Rev. B* **72**, 104425 (2005).
- [20] C. Knetter, A. Bühler, E. Müller-Hartmann, and G. S. Uhrig, Dispersion and Symmetry of Bound States in the Shastry-Sutherland Model, *Phys. Rev. Lett.* **85**, 3958 (2000).
- [21] M. Al Hajj and J.-P. Malrieu, Phase transitions in the Shastry-Sutherland lattice, *Phys. Rev. B* **72**, 094436 (2005).
- [22] A. Koga and N. Kawakami, Quantum Phase Transitions in the Shastry-Sutherland Model for $\text{SrCu}_2(\text{BO}_3)_2$, *Phys. Rev. Lett.* **84**, 4461 (2000).
- [23] Y. Takushima, A. Koga, and N. Kawakami, Competing Spin-Gap Phases in a Frustrated Quantum Spin System in Two Dimensions, *J. Phys. Soc. Jpn.* **70**, 1369 (2001).
- [24] W. Zheng, J. Oitmaa, and C. J. Hamer, Phase diagram of the Shastry-Sutherland antiferromagnet, *Phys. Rev. B* **65**, 014408 (2001).
- [25] C. H. Chung, J. B. Marston, and S. Sachdev, Quantum phases of the Shastry-Sutherland antiferromagnet: Application to $\text{SrCu}_2(\text{BO}_3)_2$, *Phys. Rev. B* **64**, 134407 (2001).
- [26] A. Läuchli, S. Wessel, and M. Sigrist, Phase diagram of the quadrumerized Shastry-Sutherland model, *Phys. Rev. B* **66**, 014401 (2002).
- [27] R. Kumar and B. Kumar, Triplon mean-field analysis of an antiferromagnet with degenerate Shastry-Sutherland ground states, *J. Phys. Commun.* **1**, 055020 (2017).
- [28] S. Moukouri, Plaquette ground state of the Shastry-Sutherland model: Density-matrix renormalization-group calculations, *Phys. Rev. B* **78**, 132405 (2008).
- [29] A. Isacsson and O. F. Syljuåsen, Variational treatment of the Shastry-Sutherland antiferromagnet using projected entangled pair states, *Phys. Rev. E* **74**, 026701 (2006).
- [30] P. Corboz and F. Mila, Tensor network study of the Shastry-Sutherland model in zero magnetic field, *Phys. Rev. B* **87**, 115144 (2013).
- [31] J. Y. Lee, Y.-Z. You, S. Sachdev, and A. Vishwanath, Signatures of a Deconfined Phase Transition on the Shastry-Sutherland Lattice: Applications to Quantum Critical $\text{SrCu}_2(\text{BO}_3)_2$, *Phys. Rev. X* **9**, 041037 (2019).
- [32] A. Keleş and E. Zhao, Rise and fall of plaquette order in the Shastry-Sutherland magnet revealed by pseudofermion functional renormalization group, *Phys. Rev. B* **105**, L041115 (2022).
- [33] D. Carpentier and L. Balents, Field theory for generalized Shastry-Sutherland models, *Phys. Rev. B* **65**, 024427 (2001).
- [34] D. C. Ronquillo and M. R. Peterson, Identifying topological order in the Shastry-Sutherland model via entanglement entropy, *Phys. Rev. B* **90**, 201108 (2014).
- [35] T. Waki, K. Arai, M. Takigawa, Y. Saiga, Y. Uwatoko, H. Kageyama, and Y. Ueda, A Novel Ordered Phase in $\text{SrCu}_2(\text{BO}_3)_2$ under High Pressure, *J. Phys. Soc. Jpn.* **76**, 073710 (2007).
- [36] M. E. Zayed, C. Rüegg, J. Larrea J., A. M. Läuchli, C. Panagopoulos, S. S. Saxena, M. Ellerby, D. F. McMorrow, T. Strässle, S. Klotz, G. Hamel, R. A. Sadykov, V. Pomjakushin, M. Boehm, M. Jiménez-Ruiz, A. Schneidewind, E. Pomjakushina, M. Stingaciu, K. Conder, and H. M. Rønnow, 4-spin plaquette singlet state in the Shastry-Sutherland compound $\text{SrCu}_2(\text{BO}_3)_2$, *Nat. Phys.* **13**, 962 (2017).
- [37] J. Guo, G. Sun, B. Zhao, L. Wang, W. Hong, V. A. Sidorov, N. Ma, Q. Wu, S. Li, Z. Y. Meng, A. W. Sandvik, and L. Sun, Quantum Phases of $\text{SrCu}_2(\text{BO}_3)_2$ from High-Pressure Thermodynamics, *Phys. Rev. Lett.* **124**, 206602 (2020).
- [38] W.-Y. Liu, X.-T. Zhang, Z. Wang, S.-S. Gong, W.-Q. Chen, and Z.-C. Gu, Deconfined quantum critical-

- ity with emergent symmetry in the extended Shastry-Sutherland model (2023), [arXiv:2309.10955 \[cond-mat.str-el\]](#).
- [39] X. Qian, R. Lv, J. Y. Lee, and M. Qin, From the Shastry-Sutherland model to the J_1 - J_2 Heisenberg model (2024), [arXiv:2411.17452 \[cond-mat.str-el\]](#).
- [40] H. Chen, G. Duan, C. Liu, Y. Cui, W. Yu, Z. Y. Xie, and R. Yu, Spin excitations of the Shastry-Sutherland model – altermagnetism and proximate deconfined quantum criticality (2024), [arXiv:2411.00301 \[cond-mat.str-el\]](#).
- [41] Y.-T. Yang, F.-Z. Chen, and H.-G. Luo, Identifying the ground state phases by spin-patterns in the Shastry-Sutherland model (2024), [arXiv:2404.16330 \[cond-mat.str-el\]](#).
- [42] N. Xi, H. Chen, Z. Y. Xie, and R. Yu, First-order transition between the plaquette valence bond solid and antiferromagnetic phases of the Shastry-Sutherland model (2021), [arXiv:2111.07368 \[cond-mat.str-el\]](#).
- [43] J. Yang, A. W. Sandvik, and L. Wang, Quantum criticality and spin liquid phase in the Shastry-Sutherland model, *Phys. Rev. B* **105**, L060409 (2022).
- [44] L. Wang, Y. Zhang, and A. W. Sandvik, Quantum Spin Liquid Phase in the Shastry-Sutherland Model Detected by an Improved Level Spectroscopic Method, *Chin. Phys. Lett.* **39**, 077502 (2022).
- [45] H. Nakano and T. Sakai, Third Boundary of the Shastry-Sutherland Model by Numerical Diagonalization, *J. Phys. Soc. Jpn.* **87**, 123702 (2018).
- [46] L. L. Viteritti, R. Rende, A. Parola, S. Goldt, and F. Becca, Transformer Wave Function for the Shastry-Sutherland Model: emergence of a Spin-Liquid Phase (2024), [arXiv:2311.16889 \[cond-mat.str-el\]](#).
- [47] M. Mezera, J. Menšíková, P. Baláž, and M. Žonda, Neural network quantum states analysis of the Shastry-Sutherland model, *SciPost Phys. Core* **6**, 088 (2023).
- [48] W.-J. Hu, F. Becca, A. Parola, and S. Sorella, Direct evidence for a gapless \mathbb{Z}_2 spin liquid by frustrating Néel antiferromagnetism, *Phys. Rev. B* **88**, 060402 (2013).
- [49] F. Ferrari and F. Becca, Gapless spin liquid and valence-bond solid in the J_1 - J_2 Heisenberg model on the square lattice: Insights from singlet and triplet excitations, *Phys. Rev. B* **102**, 014417 (2020).
- [50] S. Morita, R. Kaneko, and M. Imada, Quantum Spin Liquid in Spin-1/2 J_1 - J_2 Heisenberg Model on Square Lattice: Many-Variable Variational Monte Carlo Study Combined with Quantum-Number Projections, *J. Phys. Soc. Jpn.* **84**, 024720 (2015).
- [51] Y. Nomura and M. Imada, Dirac-Type Nodal Spin Liquid Revealed by Refined Quantum Many-Body Solver Using Neural-Network Wave Function, Correlation Ratio, and Level Spectroscopy, *Phys. Rev. X* **11**, 031034 (2021).
- [52] L. Wang and A. W. Sandvik, Critical Level Crossings and Gapless Spin Liquid in the Square-Lattice Spin-1/2 $J_1 - J_2$ Heisenberg Antiferromagnet, *Phys. Rev. Lett.* **121**, 107202 (2018).
- [53] W.-Y. Liu, S. Dong, C. Wang, Y. Han, H. An, G.-C. Guo, and L. He, Gapless spin liquid ground state of the spin- $\frac{1}{2}$ $J_1 - J_2$ Heisenberg model on square lattices, *Phys. Rev. B* **98**, 241109 (2018).
- [54] W.-Y. Liu, S.-S. Gong, Y.-B. Li, D. Poilblanc, W.-Q. Chen, and Z.-C. Gu, Gapless quantum spin liquid and global phase diagram of the spin-1/2 J_1 - J_2 square antiferromagnetic Heisenberg model, *Sci. Bull.* **67**, 1034 (2022).
- [55] X.-G. Wen, Quantum orders and symmetric spin liquids, *Phys. Rev. B* **65**, 165113 (2002).
- [56] X.-G. Wen, *Quantum Field Theory of Many-Body Systems: From the Origin of Sound to an Origin of Light and Electrons* (Oxford University Press, 2007).
- [57] F. Wang and A. Vishwanath, Spin-liquid states on the triangular and Kagomé lattices: A projective-symmetry-group analysis of Schwinger boson states, *Phys. Rev. B* **74**, 174423 (2006).
- [58] M. J. Lawler, A. Paramekanti, Y. B. Kim, and L. Balents, Gapless Spin Liquids on the Three-Dimensional Hyperkagome Lattice of $\text{Na}_4\text{Ir}_3\text{O}_8$, *Phys. Rev. Lett.* **101**, 197202 (2008).
- [59] T.-P. Choy and Y. B. Kim, Classification of quantum phases for the star-lattice antiferromagnet via a projective symmetry group analysis, *Phys. Rev. B* **80**, 064404 (2009).
- [60] B.-J. Yang, A. Paramekanti, and Y. B. Kim, Competing quantum paramagnetic ground states of the Heisenberg antiferromagnet on the star lattice, *Phys. Rev. B* **81**, 134418 (2010).
- [61] Y.-M. Lu, Y. Ran, and P. A. Lee, \mathbb{Z}_2 spin liquids in the $S = \frac{1}{2}$ Heisenberg model on the kagome lattice: A projective symmetry-group study of Schwinger fermion mean-field states, *Phys. Rev. B* **83**, 224413 (2011).
- [62] Y.-M. Lu and Y. Ran, \mathbb{Z}_2 spin liquid and chiral antiferromagnetic phase in the Hubbard model on a honeycomb lattice, *Phys. Rev. B* **84**, 024420 (2011).
- [63] F. Yang and H. Yao, Frustrated resonating valence bond states in two dimensions: Classification and short-range correlations, *Phys. Rev. Lett.* **109**, 147209 (2012).
- [64] L. Messio, C. Lhuillier, and G. Misguich, Time reversal symmetry breaking chiral spin liquids: Projective symmetry group approach of bosonic mean-field theories, *Phys. Rev. B* **87**, 125127 (2013).
- [65] S. Bieri, L. Messio, B. Bernu, and C. Lhuillier, Gapless chiral spin liquid in a kagome Heisenberg model, *Phys. Rev. B* **92**, 060407 (2015).
- [66] X. Yang and F. Wang, Schwinger boson spin-liquid states on square lattice, *Phys. Rev. B* **94**, 035160 (2016).
- [67] Y.-M. Lu, Symmetric \mathbb{Z}_2 spin liquids and their neighboring phases on triangular lattice, *Phys. Rev. B* **93**, 165113 (2016).
- [68] S. Bieri, C. Lhuillier, and L. Messio, Projective symmetry group classification of chiral spin liquids, *Phys. Rev. B* **93**, 094437 (2016).
- [69] B. Huang, Y. B. Kim, and Y.-M. Lu, Interplay of nonsymmorphic symmetry and spin-orbit coupling in hyperkagome spin liquids: Applications to $\text{Na}_4\text{Ir}_3\text{O}_8$, *Phys. Rev. B* **95**, 054404 (2017).
- [70] B. Huang, W. Choi, Y. B. Kim, and Y.-M. Lu, Classification and properties of quantum spin liquids on the hyperhoneycomb lattice, *Phys. Rev. B* **97**, 195141 (2018).
- [71] Y.-M. Lu, Symmetry-protected gapless \mathbb{Z}_2 spin liquids, *Phys. Rev. B* **97**, 094422 (2018).
- [72] C. Liu, G. B. Halász, and L. Balents, Competing orders in pyrochlore magnets from a \mathbb{Z}_2 spin liquid perspective, *Phys. Rev. B* **100**, 075125 (2019).
- [73] H.-K. Jin and Y. Zhou, Classical and quantum order

- in hyperkagome antiferromagnets, *Phys. Rev. B* **101**, 054408 (2020).
- [74] J. Sonnenschein, A. Chauhan, Y. Iqbal, and J. Reuther, Projective symmetry group classifications of quantum spin liquids on the simple cubic, body centered cubic, and face centered cubic lattices, *Phys. Rev. B* **102**, 125140 (2020).
- [75] J. Sahoo and R. Flint, Symmetric spin liquids on the stuffed honeycomb lattice, *Phys. Rev. B* **101**, 115103 (2020).
- [76] C. Liu, G. B. Halász, and L. Balents, Symmetric $U(1)$ and \mathbb{Z}_2 spin liquids on the pyrochlore lattice, *Phys. Rev. B* **104**, 054401 (2021).
- [77] L. E. Chern and Y. B. Kim, Theoretical study of quantum spin liquids in $S = \frac{1}{2}$ hyper-hyperkagome magnets: Classification, heat capacity, and dynamical spin structure factor, *Phys. Rev. B* **104**, 094413 (2021).
- [78] L. E. Chern, Y. B. Kim, and C. Castelnovo, Competing quantum spin liquids, gauge fluctuations, and anisotropic interactions in a breathing pyrochlore lattice, *Phys. Rev. B* **106**, 134402 (2022).
- [79] B. Schneider, J. C. Halimeh, and M. Punk, Projective symmetry group classification of chiral \mathbb{Z}_2 spin liquids on the pyrochlore lattice: Application to the spin- $\frac{1}{2}$ XXZ Heisenberg model, *Phys. Rev. B* **105**, 125122 (2022).
- [80] A. Maity, F. Ferrari, R. Thomale, S. Mandal, and Y. Iqbal, Projective symmetry group classification of Abrikosov fermion mean-field ansätze on the square-octagon lattice, *Phys. Rev. B* **107**, 134438 (2023).
- [81] A. Chauhan, A. Maity, C. Liu, J. Sonnenschein, F. Ferrari, and Y. Iqbal, Quantum spin liquids on the diamond lattice, *Phys. Rev. B* **108**, 134424 (2023).
- [82] K. Liu and F. Wang, Schwinger boson symmetric spin liquids of Shastry-Sutherland model, *Phys. Rev. B* **109**, 134409 (2024).
- [83] J. Sonnenschein, A. Maity, C. Liu, R. Thomale, F. Ferrari, and Y. Iqbal, Candidate quantum spin liquids on the maple-leaf lattice, *Phys. Rev. B* **110**, 014414 (2024).
- [84] A. Maity, R. Samajdar, and Y. Iqbal, Gapped and gapless quantum spin liquids on the ruby lattice (2024), [arXiv:2409.16344 \[cond-mat.str-el\]](https://arxiv.org/abs/2409.16344).
- [85] A. Maity, Y. Iqbal, and R. Samajdar, Fermionic parton theory of Rydberg \mathbb{Z}_2 quantum spin liquids (2024), [arXiv:2409.17219 \[cond-mat.str-el\]](https://arxiv.org/abs/2409.17219).
- [86] A. A. Abrikosov, Electron scattering on magnetic impurities in metals and anomalous resistivity effects, *Physics* **2**, 5 (1965).
- [87] G. Baskaran and P. W. Anderson, Gauge theory of high-temperature superconductors and strongly correlated Fermi systems, *Phys. Rev. B* **37**, 580 (1988).
- [88] I. Affleck, Z. Zou, T. Hsu, and P. W. Anderson, $SU(2)$ gauge symmetry of the large- U limit of the Hubbard model, *Phys. Rev. B* **38**, 745 (1988).
- [89] Z.-X. Liu, Y. Zhou, and T.-K. Ng, Fermionic theory for quantum antiferromagnets with spin $S > \frac{1}{2}$, *Phys. Rev. B* **82**, 144422 (2010).
- [90] R. Shindou, S. Yunoki, and T. Momoi, Projective studies of spin nematics in a quantum frustrated ferromagnet, *Phys. Rev. B* **84**, 134414 (2011).
- [91] J. Reuther, S.-P. Lee, and J. Alicea, Classification of spin liquids on the square lattice with strong spin-orbit coupling, *Phys. Rev. B* **90**, 174417 (2014).
- [92] F. Becca and S. Sorella, *Quantum Monte Carlo Approaches for Correlated Systems* (Cambridge University Press, 2017).
- [93] S. Sorella, Wave function optimization in the variational Monte Carlo method, *Phys. Rev. B* **71**, 241103 (2005).
- [94] S. Yunoki and S. Sorella, Two spin liquid phases in the spatially anisotropic triangular Heisenberg model, *Phys. Rev. B* **74**, 014408 (2006).
- [95] Y. Iqbal, D. Poilblanc, and F. Becca, Spin- $\frac{1}{2}$ Heisenberg $J_1 - J_2$ antiferromagnet on the kagome lattice, *Phys. Rev. B* **91**, 020402 (2015).
- [96] Y. Iqbal, F. Ferrari, A. Chauhan, A. Parola, D. Poilblanc, and F. Becca, Gutzwiller projected states for the $J_1 - J_2$ Heisenberg model on the Kagome lattice: Achievements and pitfalls, *Phys. Rev. B* **104**, 144406 (2021).
- [97] M. Hering, V. Noculak, F. Ferrari, Y. Iqbal, and J. Reuther, Dimerization tendencies of the pyrochlore Heisenberg antiferromagnet: A functional renormalization group perspective, *Phys. Rev. B* **105**, 054426 (2022).
- [98] F. Ferrari, S. Niu, J. Hasik, Y. Iqbal, D. Poilblanc, and F. Becca, Static and dynamical signatures of Dzyaloshinskii-Moriya interactions in the Heisenberg model on the kagome lattice, *SciPost Phys.* **14**, 139 (2023).
- [99] T. Müller, R. Thomale, S. Sachdev, and Y. Iqbal, Polaronic correlations from optimized ancilla wave functions for the Fermi-Hubbard model (2024), [arXiv:2408.01492 \[cond-mat.str-el\]](https://arxiv.org/abs/2408.01492).
- [100] S. Sorella, Generalized Lanczos algorithm for variational quantum Monte Carlo, *Phys. Rev. B* **64**, 024512 (2001).
- [101] F. Becca, W.-J. Hu, Y. Iqbal, A. Parola, D. Poilblanc, and S. Sorella, Lanczos steps to improve variational wave functions, *J. Phys. Conf. Ser.* **640**, 012039 (2015).
- [102] Y. Iqbal, F. Becca, and D. Poilblanc, Projected wave function study of \mathbb{Z}_2 spin liquids on the kagome lattice for the spin- $\frac{1}{2}$ quantum Heisenberg antiferromagnet, *Phys. Rev. B* **84**, 020407 (2011).
- [103] Y. Iqbal, F. Becca, S. Sorella, and D. Poilblanc, Gapless spin-liquid phase in the kagome spin- $\frac{1}{2}$ Heisenberg antiferromagnet, *Phys. Rev. B* **87**, 060405 (2013).
- [104] Y. Iqbal, W.-J. Hu, R. Thomale, D. Poilblanc, and F. Becca, Spin liquid nature in the Heisenberg $J_1 - J_2$ triangular antiferromagnet, *Phys. Rev. B* **93**, 144411 (2016).
- [105] Y. Iqbal, D. Poilblanc, and F. Becca, Vanishing spin gap in a competing spin-liquid phase in the kagome Heisenberg antiferromagnet, *Phys. Rev. B* **89**, 020407 (2014).
- [106] C. Knetter and G. S. Uhrig, Dynamic Structure Factor of the Two-Dimensional Shastry-Sutherland Model, *Phys. Rev. Lett.* **92**, 027204 (2004).
- [107] T. Müller, D. Kiese, N. Niggemann, B. Sbierski, J. Reuther, S. Trebst, R. Thomale, and Y. Iqbal, Pseudo-fermion functional renormalization group for spin models, *Rep. Prog. Phys.* **87**, 036501 (2024).
- [108] J. Reuther and R. Thomale, Cluster functional renormalization group, *Phys. Rev. B* **89**, 024412 (2014).
- [109] J. Potten *et al.*, Keldysh pseudo-fermion functional renormalization group for quantum magnetism, in preparation.

- [110] U. Löw and E. Müller-Hartmann, Exact Bounds on the Critical Frustration in the Shastry–Sutherland Model, *J. Low Temp. Phys.* **126**, 1135 (2002).
- [111] A. Grechnev, Exact ground state of the Shastry-Sutherland lattice with classical Heisenberg spins, *Phys. Rev. B* **87**, 144419 (2013).
- [112] D. Kiese, F. Ferrari, N. Astrakhantsev, N. Niggemann, P. Ghosh, T. Müller, R. Thomale, T. Neupert, J. Reuther, M. J. P. Gingras, S. Trebst, and Y. Iqbal, Pinch-points to half-moons and up in the stars: The kagome skymap, *Phys. Rev. Res.* **5**, L012025 (2023).
- [113] A. Thomson and S. Sachdev, Fermionic Spinon Theory of Square Lattice Spin Liquids near the Néel State, *Phys. Rev. X* **8**, 011012 (2018).
- [114] H. Shackleton, A. Thomson, and S. Sachdev, Deconfined criticality and a gapless \mathbb{Z}_2 spin liquid in the square-lattice antiferromagnet, *Phys. Rev. B* **104**, 045110 (2021).
- [115] J.-W. Yang, W.-W. Luo, W. Zhu, L. Wang, B. Yang, and P. Sengupta, Chiral spin liquid on a Shastry-Sutherland Heisenberg antiferromagnet, *Phys. Rev. B* **109**, 205111 (2024).
- [116] F. Dusel, T. Hofmann, A. Maity, Y. Iqbal, M. Greiter, and R. Thomale, Chiral Gapless Spin Liquid in Hyperbolic Space (2024), [arXiv:2407.15705 \[cond-mat.str-el\]](https://arxiv.org/abs/2407.15705).
- [117] F. Oliviero, J. A. Sobral, E. C. Andrade, and R. G. Pereira, Noncoplanar magnetic orders and gapless chiral spin liquid on the kagome lattice with staggered scalar spin chirality, *SciPost Phys.* **13**, 050 (2022).
- [118] H. S. Kim, H.-J. Yang, K. Penc, and S. Lee, Spin Liquid Landscapes in the Kagome Lattice: A Variational Monte Carlo Study of the Chiral Heisenberg Model and Experimental Consequences (2024), [arXiv:2411.09542 \[cond-mat.str-el\]](https://arxiv.org/abs/2411.09542).
- [119] G. Duan, R. Yu, and C. Liu, Theory of magnetism for rare-earth magnets on the Shastry-Sutherland lattice with non-Kramers ions (2024), [arXiv:2409.12534 \[cond-mat.str-el\]](https://arxiv.org/abs/2409.12534).
- [120] C. Liu, G. Duan, and R. Yu, Theory of rare-earth Kramers magnets on a Shastry-Sutherland lattice: dimer phases in presence of strong spin-orbit coupling (2024), [arXiv:2412.00757 \[cond-mat.str-el\]](https://arxiv.org/abs/2412.00757).
- [121] W.-J. Hu, S.-S. Gong, F. Becca, and D. N. Sheng, Variational Monte Carlo study of a gapless spin liquid in the spin- $\frac{1}{2}$ XXZ antiferromagnetic model on the kagome lattice, *Phys. Rev. B* **92**, 201105 (2015).
- [122] J. Romhányi, K. Totsuka, and K. Penc, Effect of Dzyaloshinskii-Moriya interactions on the phase diagram and magnetic excitations of $\text{SrCu}_2(\text{BO}_3)_2$, *Phys. Rev. B* **83**, 024413 (2011).
- [123] T. Chen, C. Guo, P. Sengupta, and D. Poletti, Effects of staggered Dzyaloshinskii-Moriya interactions in a quasi-two-dimensional Shastry-Sutherland model, *Phys. Rev. B* **101**, 064417 (2020).
- [124] H.-J. Yang and S. Lee, Topological phases of nonsym-morphic crystals: Shastry-Sutherland lattice at integer filling, *Phys. Rev. B* **99**, 165140 (2019).
- [125] Y. Ran, W.-H. Ko, P. A. Lee, and X.-G. Wen, Spontaneous Spin Ordering of a Dirac Spin Liquid in a Magnetic Field, *Phys. Rev. Lett.* **102**, 047205 (2009).
- [126] Y. Iqbal, F. Becca, and D. Poilblanc, Valence-bond crystal in the extended kagome spin- $\frac{1}{2}$ quantum Heisenberg antiferromagnet: A variational Monte Carlo approach, *Phys. Rev. B* **83**, 100404 (2011).
- [127] Y. Iqbal, F. Becca, and D. Poilblanc, Valence-bond crystals in the kagomé spin-1/2 Heisenberg antiferromagnet: a symmetry classification and projected wave function study, *New J. Phys.* **14**, 115031 (2012).
- [128] Y. Iqbal, D. Poilblanc, R. Thomale, and F. Becca, Persistence of the gapless spin liquid in the breathing kagome Heisenberg antiferromagnet, *Phys. Rev. B* **97**, 115127 (2018).
- [129] N. Astrakhantsev, F. Ferrari, N. Niggemann, T. Müller, A. Chauhan, A. Kshetrimayum, P. Ghosh, N. Regnault, R. Thomale, J. Reuther, T. Neupert, and Y. Iqbal, Pinwheel valence bond crystal ground state of the spin- $\frac{1}{2}$ Heisenberg antiferromagnet on the shuriken lattice, *Phys. Rev. B* **104**, L220408 (2021).